THE UNIVERSITY OF CHICAGO

THEORETICAL STUDY OF HABITABLE TERRESTRIAL PLANETS AND STATISTICAL TESTS TO INFORM FUTURE OBSERVATIONS

A DISSERTATION SUBMITTED TO
THE FACULTY OF THE DIVISION OF THE PHYSICAL SCIENCES
IN CANDIDACY FOR THE DEGREE OF
DOCTOR OF PHILOSOPHY

DEPARTMENT OF THE GEOPHYSICAL SCIENCES

BY
JADE CHECLAIR

CHICAGO, ILLINOIS
AUGUST 2021

This dissertation is dedicated to my grandmother, Frédérique Balhan, who instilled in me a lifelong love of learning and exploring.

Cette thèse est dédiée à ma grand-mère, Frédérique Balhan, qui m'a inculqué l'amour d'apprendre et d'explorer.

“I guess I’d say if it is just us...

seems like an awful waste of space.”

– Contact (1997)

TABLE OF CONTENTS

I STATISTICAL TESTS FOR KEY THEORIES OF HABITABILITY WITH FUTURE DIRECT IMAGING MISSIONS

II THE SNOWBALL BIFURCATION ON HABITABLE TIDALLY LOCKED PLANETS

LIST OF FIGURES

LIST OF TABLES

ACKNOWLEDGMENTS

I would like to thank my advisor, Dorian Abbot, for mentoring and guiding me through graduate school, and for helping me grow as a scientist. Thank you also to my committee members, Jacob Bean, Edwin Kite, Leslie Rogers, and Malte Jansen, for providing valuable feedback and insight on my work and progress. Additional thanks to Tad Komacek, Stephanie Olson, and Geronimo Villanueva for their mentorship and collaboration on many projects.

I would also like to thank Chris McKay, who first inspired me to study planetary science through his enthusiasm and encouragement, and who gave me my first chance at doing research which set me on this path.

Thank you to my husband, Benjamin Hayworth, for supporting me in every possible way throughout this entire process, and for frequentely engaging in thoughtful discussions on this work which helped me greatly.

Thank you to my parents, Claire Mottart and Philippe Checlair, for their support and encouragement. Special thanks to my grandmother, Frédérique Balhan, for always believing in me and pushing me to do my best.

Finally, thank you to my wonderful dog, Kali, for always putting a smile on my face and never failing to take me out on a walk no matter how busy I got.

ABSTRACT

Future space telescopes will provide us with the opportunity to characterize the atmospheres of terrestrial planets orbiting within the habitable zones of their stars. In the near future, the James Webb Space Telescope (JWST) will allow us to spectrally characterize terrestrial planets orbiting M-stars. In the more distant future, telescopes such as the Large UV/Optical/IR Surveyor (LUVOIR) and the Habitable Exoplanet Observatory (HabEx) will allow us to direct image Earth-sized habitable zone terrestrial planets orbiting Sun-like stars (exoEarths). In this dissertation, I explore the habitability of both G-star and M-star habitable zone planets. In part 1 of this dissertation, I focus on habitable zone planets around Sun-like stars, and explore testing key theories of habitability statistically with direct imaging missions. These tests would exploit statistical marginalization of uncertainty inherent to both terrestrial planets and observations by using large samples of detected exoEarths. In Chapter 2, I propose a statistical test for the silicate-weathering feedback, which is a stabilizing negative feedback believed to help maintain habitable conditions on habitable zone planets. I find that if the silicate-weathering feedback is common on exoEarths, we are likely to detect it with LUVOIR-A, and may detect it with LUVOIR-B if the natural spread of planetary parameters is small. We are unlikely to detect it with HabEx due to its small expected exoEarth yield. In Chapter 3, I develop a statistical test for whether exoEarths tend to be Earth-like. Specifically, I consider whether observations with LUVOIR and HabEx could inform us on the fraction of exoEarths that are Earth-like (f_E) in that they develop Earth-like, O_2-producing life (oxygenic photosynthesis) that oxygenates their atmospheres roughly following Earth's oxygenation history. I explore this specifically in the event of a null detection of O_2 or O_3 on every exoEarth. I find that missions with larger aperture mirrors are more robust to uncertainties in the exoEarth occurrence rate ($\eta_\oplus$), but all missions are vulnerable to inconclusive null detections if $\eta_\oplus$ is very low. In Chapter 4, I quantify the detectability of O_2 and O_3 for future direct imaging missions LUVOIR and HabEx using a 3D Global Climate Model that includes photochemistry and realistic cloud coverage. I

find that realistic cloud coverage increases the detectability of both O_2 and O_3, despite the fact that clouds obstruct some of the absorbing gas column mass, due to the strong effect of clouds on planetary reflectivity for planets with a low-to-intermediate surface albedo.

In part 2 of this dissertation, I focus on habitable zone planets orbiting M-stars, which are expected to be tidally locked. Specifically, I explore the Snowball bifurcation on tidally locked planets. In Chapter 5, I show that tidally locked planets do not exhibit a Snowball bifurcation, regardless of stellar spectrum, as a direct result of the spatial pattern of insolation they receive. In Chapter 6, I explore whether realistic ocean heat transport can reintroduce the Snowball bifurcation for habitable tidally locked planets by destabilizing partially glaciated states. I show that including ocean heat transport does not reintroduce the Snowball bifurcation and that the lack of a Snowball bifurcation on tidally locked planets is robust to realistic levels of ocean heat transport. In Chapter 7, I explore whether limit cycling between Warm and Snowball states at the outer edge of the habitable zone occurs for tidally locked planets. I show that tidally locked planets with an active carbon cycle will not experience limit cycling as a result of their lack of a Snowball bifurcation, and instead will settle into “Eyeball” states with a small unglaciated substellar region if they orbit near the outer edge of the habitable zone.

CHAPTER 1

INTRODUCTION

1.1 Observing Exoplanets and their Atmospheres

The past two decades have been extremely productive for the field of exoplanet science, with more than 4000 exoplanets discovered using methods such as radial velocity (RV), transits, and microlensing (e.g., Mayor and Queloz, 1995; Charbonneau et al., 1999; Bond et al., 2004; Borucki et al., 2010; Gillon et al., 2017). Recently, a number of Earth-sized exoplanets have been found orbiting in the habitable zone of nearby M-stars (e.g., TRAPPIST-1e, Proxima Centauri b, and LHS1140b, Anglada-Escudé et al., 2016; Gillon et al., 2017; Dittmann et al., 2017). These are prime targets for future instruments to study in more detail and determine whether they are truly habitable, or even inhabited (e.g., Kreidberg and Loeb, 2016; Meadows et al., 2018a).

NASA's upcoming James Webb Space Telescope (JWST) (Gardner et al., 2006) should dramatically increase our ability to find and characterize terrestrial exoplanets orbiting M-stars (e.g., Deming et al., 2009; Cowan et al., 2015) However, most terrestrial atmospheric characterization targets will likely orbit too close to their stars for habitability. Despite this, JWST may attempt to characterize some habitable zone terrestrial planets around M-stars using transit spectroscopy (e.g., Barstow and Irwin, 2016; Lincowski et al., 2019). This method of spectral characterization relies on the planet orbiting in our observational plane, and transiting its star. When the planet transits in front of its star, we can measure molecular absorption features of the light that passes through the atmospheric envelope of the planet. Conversely, when the planet is close to passing behind its star during secondary transit, we can observe the emission features from the fully-lit dayside of the planet. JWST is optimized for infrared wavelengths (0.6μm - 28μm) (Gardner et al., 2006), and M-star planets will be the ideal candidates as they allow for multiple transits (which will occur more often for the short orbital periods around M-stars) and are favorable for a larger ratio of $\frac{R_p}{R_\star}$, where R_p is the radius of the planet transiting a star with radius $R_\star$.

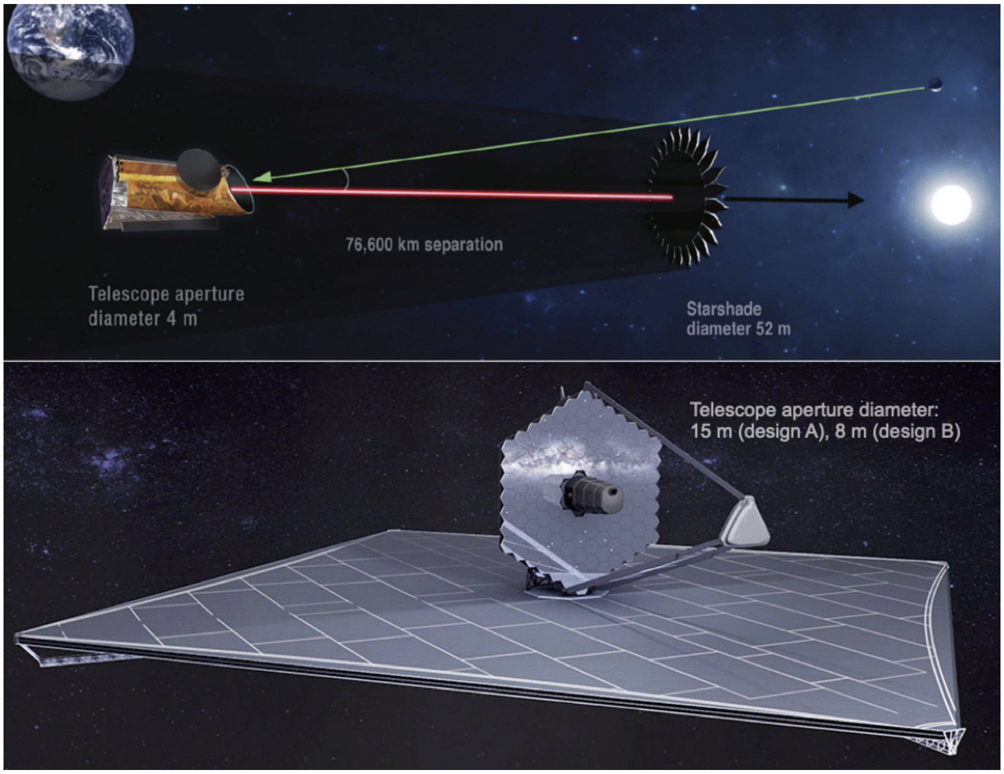

Figure 1.1: **The HabEx (top) and LUVOIR (bottom) mission concepts.** HabEx is designed with a 4 m diameter mirror and a starshade to suppress starlight. LUVOIR-A is designed with a 15 m diameter mirror, LUVOIR-B with an 8 m diameter mirror, as well as a coronagraph to suppress starlight. Image credits: NASA.

Characterizing Earth-sized planets orbiting in the habitable zone of Sun-like stars will require a new generation of telescopes. The National Academies of Sciences Engineering Medicine (NASEM) Astro 2020: Decadal Survey on Astronomy and Astrophysics is considering two future flagship concepts with a strong focus on exoplanet direct imaging: HabEx (Gaudi et al., 2020) and LUVOIR (The LUVOIR Team et al., 2019), shown in Figure 1.1. These instruments will allow us to characterize the atmospheres of habitable zone Earth-sized planets orbiting Sun-like stars (exoEarth candidates) via direct imaging. Direct imaging is a method of spectral characterization that allows us to observe starlight reflected off the target planet. This presents technical challenges, namely, suppressing the star's emitted light and achieving the minimum angular separation (inner working angle, IWA) to resolve the star and planet as separate entities. Both LUVOIR and HabEx will be optimized for observation in the UV through Near-IR (0.2μm - 2μm). This will allow them to achieve an IWA capable of resolving the star and planet at reasonable aperture sizes (4m-15m). Both missions will include a coronagraph (and/or starshade) capable of achieving a contrast ratio of $\sim 10^{-10}$ between the light emitted from the host star and the light reflected off the planet - a necessary ratio for observing exoEarth systems. This makes F, G, and K-star systems ideal targets for LUVOIR and HabEx, though they may still be able to observe some of the closest M-star planetary systems via direct imaging.

1.2 The Habitable Zone

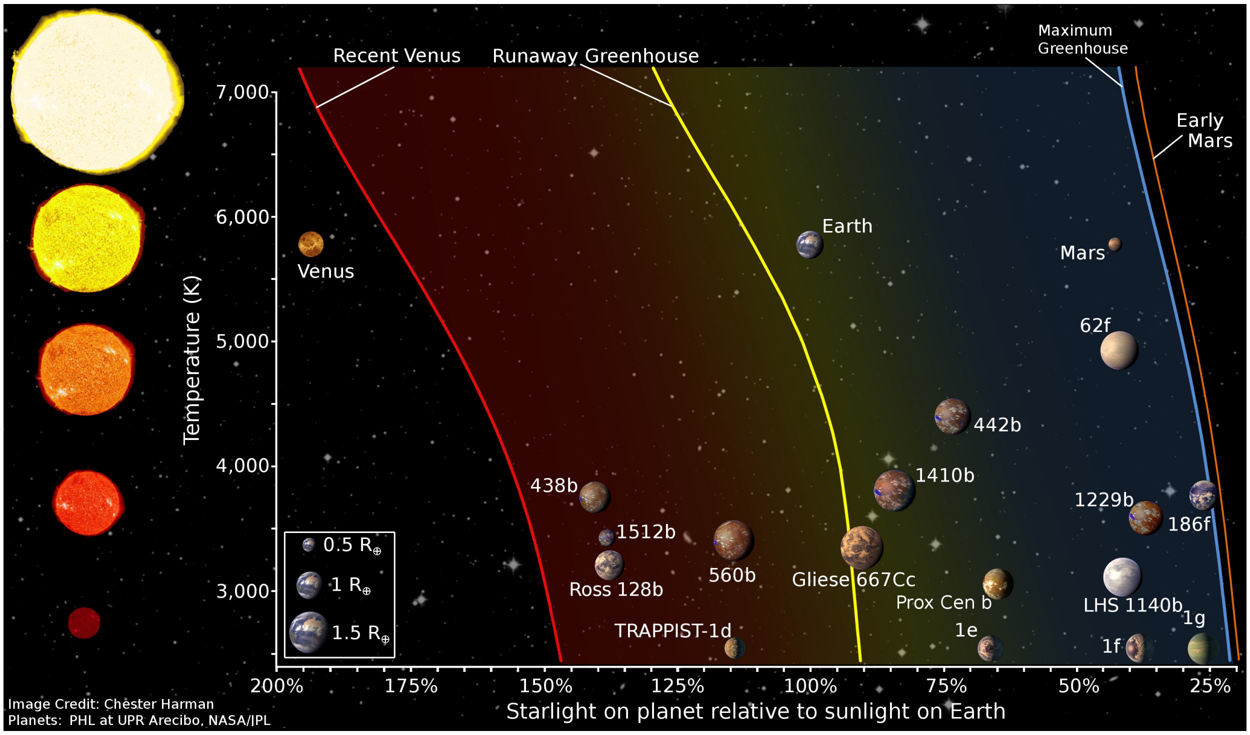

Figure 1.2: **The Habitable Zone.** This figure shows different habitable zone boundaries for different stellar types. Selected exoplanets and Solar System planets are shown. Image credit: Chester Harman.

The habitable zone is defined as the range of distances around a star within which liquid water could exist on a planet's surface given sufficient atmospheric pressure. Traditional habitable zone theory (Kasting et al., 1993a) assumes that the surface temperature of habitable planets is regulated inside the habitable zone, allowing for surface liquid water. A diagram of the habitable zone is shown in Figure 1.2. As shown in this diagram, the limits of the habitable zone depend on stellar type, with the habitable zones of Sun-like (G-type) stars being further out than the habitable zones of M-stars. This is because planets orbiting more luminous stars, such as G-stars, require a larger orbital separation to maintain habitable surface conditions than those orbiting less luminous stars such as M-stars.

Inside the “runaway greenhouse” inner edge of the habitable zone (that is, closer to the host star), planets are expected to have surface temperatures too hot for habitability, and to potentially lose their entire water inventory as a result of a runaway greenhouse process (e.g., Ingersoll, 1969; Kasting, 1988). This process occurs when the insolation is high enough to trigger a runaway, where increasing surface temperatures increases the water inventory of the atmosphere. This cycle continues, continually heating the planet and causing the ‘cold-trap’ (the altitude by which effectively all the water vapor is condensed out) to become non-existent. This allows for large quantities of water vapor to make it into the stratosphere where it is subsequently photolyzed and lost to space via hydrogen escape (Kasting and Pollack, 1983; Tian et al., 2005; Kopparapu et al., 2014). Another, more conservative, inner edge of the habitable zone is defined as the “moist greenhouse” limit, where the water-loss is exacerbated by the same mechanism as in the “runaway greenhouse”, though the surface temperature is stable. Outside the outer edge of the habitable zone, planets are expected to be frozen. The outer edge is set by the maximum greenhouse effect CO_2-H_2O atmospheres can provide. Any pCO_2 (partial pressure of CO_2) value over this threshold acts to cool the planet by raising the planetary albedo more than it warms the planet via its greenhouse effect. At low enough insolation, no value of pCO_2 is sufficient to raise the mean surface temperature above freezing, and leads to the condensation of CO_2 out of the atmosphere (Kasting, 1991; Kasting et al., 1993a).

Within the habitable zone, located between the bounds of the inner-edge (runaway green-

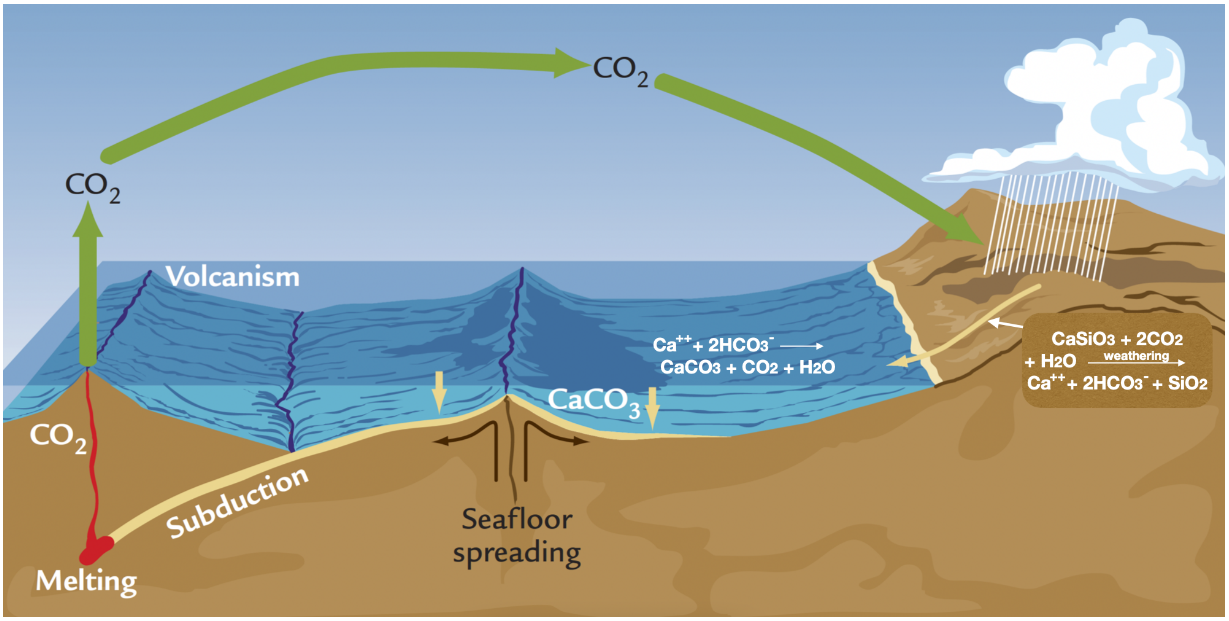

Figure 1.3: **A diagram of the carbon cycle.** CO_2 is outgassed through volcanism, and removed from the atmosphere through rock weathering and precipitation of calcium carbonate. As a planet's temperature decreases, the rate of weathering, which is dependent on temperature, slows, and CO_2 builds up in the atmosphere. This increases the greenhouse effect, which in turn increases surface temperature. This feedback mechanism is called the "silicate-weathering" feedback. Image credit: Adapted from Earth's Climate by William F. Ruddiman (2001).

house limit) and the outer-edge (maximum greenhouse limit), the silicate-weathering feedback (Walker et al., 1981a) can regulate the atmospheric CO_2 of planets through a stabilizing negative feedback. On Earth, CO_2 is outgassed through volcanism, and removed from the atmosphere through silicate weathering, which requires surface liquid water and depends strongly on surface temperature. A diagram of this carbon cycle is shown in Figure 1.3. As a planet's surface temperature decreases, the weathering rate (sequestration of CO_2 by the solid Earth) slows as precipitation rates and surface temperatures decrease (e.g., Walker et al., 1981a; Berner and Berner, 2004; Catling et al., 2019). This allows CO_2 to accumulate in the atmosphere, warming the planet back toward an equilibrium point. This feedback significantly extends the outer edge of the habitable zone, from 1.01 AU (Hart, 1979) to 1.67 AU (Kasting et al., 1993a), since it allows more distant planets to build dense CO_2 atmospheres and maintain habitable surface conditions.

1.3 Biosignatures: Remote Signs of Life on Exoplanets

Life can have a measurable impact on the composition of its host planet's atmosphere. A promising method for detecting life on an exoplanet is through the detection of "biosignatures". A biosignature, broadly, is an indicator of the presence of life on another planet. One potential biosignature is an atmospheric biosignature, where the detection of a spectral feature could only be explained by the presence of an atmospheric biogenic gas. This would indicate that life has modified its environment (e.g., Meadows, 2008; Meadows et al., 2018a; Schwieterman et al., 2018). An example of a planetary spectrum with features attributed to biosignature gases is shown in Figure 1.4. Several potential biosignatures have been proposed, such as detecting trace amounts of biologically derived molecules (e.g., Seager et al., 2005; Meadows, 2008; Seager and Deming, 2010; Seager et al., 2016; Sousa-Silva et al., 2019), the coexistence of atmospheric species that represent a thermodynamic chemical disequilibrium (Lovelock, 1965; Krissansen-Totton et al., 2018b), the detection of a vegetative "red edge" (Seager et al., 2005), bio-specific molecules (such as isoprene) (Zhan et al., 2021; Seager et al., 2016), and characteristic atmospheric seasonality (Olson et al., 2018b).

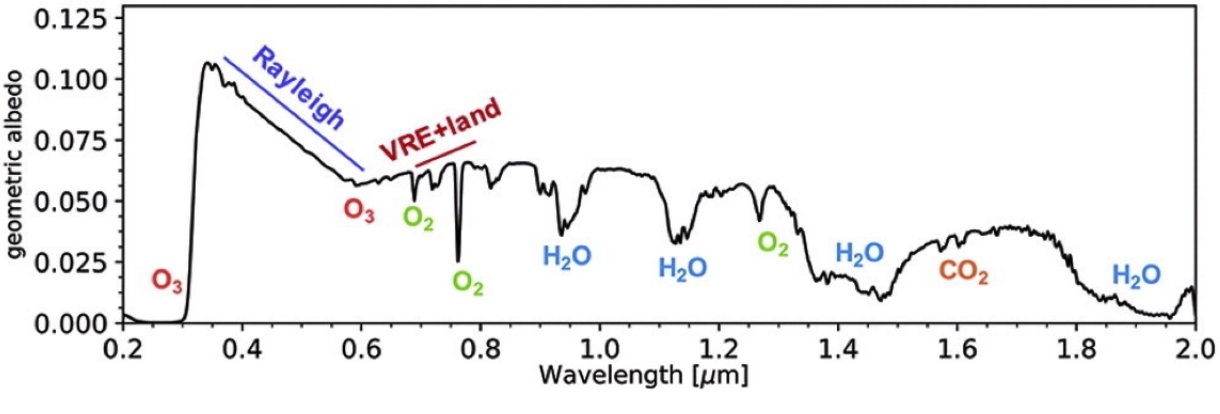

Figure 1.4: **A simulated spectrum of Earth showing various potentially detectable biosignature gases.** The wavelength range shown here includes the UV, visible, and near-IR, which could be observed by instruments such as LUVOIR and HabEx. Image credit: Schwieterman et al. (2018).

In particular, Oxygen (O_2), and its photochemical proxy Ozone (O_3), has long been considered one of the most robust biosignatures due to its reliability, survivability, and detectability in planetary atmospheres (e.g., Owen, 1980; Sagan et al., 1993; Des Marais et al., 2002; Meadows, 2008, 2017; Schwieterman et al., 2018). Its relative lack of geologic sources (compared to other major constituents such as CO_2), its long atmospheric lifetime, and its strong absorption features make O_2 an ideal candidate molecule for searching for life on exoplanets. Recent studies have identified abiotic mechanisms that may produce detectable quantities of O_2 and/or O_3 (Harman et al., 2015a; Tian et al., 2014; Meadows, 2017). These "false positive" scenarios include processes such as ocean-loss (Luger and Barnes, 2015), dissociation of CO_2 via intense FUV radiation (Harman et al., 2015b), lack of non-condensable atmospheric species (Wordsworth and Pierrehumbert, 2014), waterworlds (Krissansen-Totton et al., 2021), or planets with low initial volatile inventories (Krissansen-Totton et al., 2021). LUVOIR and HabEx's targets of interest will be habitable zone planets orbiting G-stars, which are unlikely to abiotically build up O_2/O_3 via the first two of these mechanisms (Harman et al., 2018; Meadows et al., 2018b). An important challenge in the search for biosignatures with future missions will be to rule out false positive scenarios by looking for other indicators that verify that O_2 and/or O_3 are biologic in origin. To do that, O_2 and O_3 detections will need to be interpreted within their broader chemical and planetary context.

1.4 Snowball Events and Habitability

One issue that may influence planetary habitability is the occurrence of global glaciations, which are called "Snowball" events. The Earth is believed to have plunged into these Snowballs a few times throughout its history (Kirschvink, 1992; Hoffman et al., 1998). These snowball climates in Earth's past would have left the planet almost entirely covered in ice, with the potential exception of dry continental interiors, equatorial ablation zones, or an equatorial "waterbelt" (Hoffman et al., 2017; Abbot et al., 2011a). A Snowball event begins and ends abruptly and persists for millions of years. Once the planet is fully glaciated, the weathering of CO_2 is negligible due to the lack of surface liquid water. Atmospheric CO_2 then gradually builds up through volcanism, and the resulting increased greenhouse effect is then responsible for rapidly deglaciating the planet and ending the Snowball event.

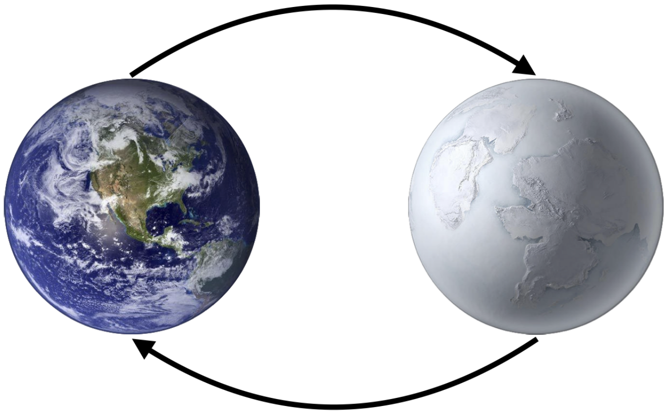

Figure 1.5: **Earth's two stable climate states: Warm state (left) and Snowball state (right).** The Earth's climate system exhibits a bistability where both a Warm and a Snowball state can exist for the same radiative forcing. Image credit: Mikkel Juul Jensen & NASA/JPL.

These Snowball events are a result of the existence of climate bifurcations, bistability, and hysteresis in rapidly rotating planets like the Earth. In the context of Snowball events, bistability means that two different climate states (a "Warm" ice-free state and a "Snowball" ice-covered state) can exist for the same external forcing (CO_2, stellar flux, etc.). This is a result of a basic nonlinearity called the ice-albedo feedback caused by the difference in top-of-atmosphere albedo of ice/snow v.s. water (Budyko, 1969; Sellers, 1969). A planet in its Warm state may "jump" into a Snowball state when the stellar flux is decreased only slightly at a particular threshold. That is because, at this threshold, the replacement of surface water with highly-reflective ice (the ice-albedo feedback) overwhelms stabilizing feedbacks in the system (Roe and Baker, 2010). At this point the modern climate state ceases to exist and the climate plunges into a Snowball state. This is an example of a saddle-node bifurcation (Strogatz, 1994), called the "Snowball bifurcation" in this context. This bifurcation (jump into a Snowball state) occurs at a critical "glaciation" stellar flux, but to deglaciate the planet the stellar flux must be increased to a much greater critical "deglaciation" value (another bifurcation). If the stellar flux is increased and decreased so that these bifurcations are crossed, its current state will be dependent on the path it has taken, which is referred to as climate hysteresis.

Snowball Earth events are an acute stressor on existing life, however, they have also been correlated with sharp increases in the complexity of life (Kirschvink, 1992; Hoffman et al., 1998) and in the atmospheric oxygen concentration (Hoffman and Schrag, 2002; Laakso and Schrag, 2014, 2017b). Given that O_2 is an important biosignature, whether a planet is able to go through such Snowball events may also have implications for the detectability of life on it.

1.5 Overview of Part 1: Statistical Tests for Key Theories of Habitability with Future Direct Imaging Missions

In the first part of this dissertation, I will focus on habitable planets orbiting Sun-like stars. Specifically, I will explore statistically testing key theories of habitability with future direct imaging missions such as LUVOIR and HabEx. These missions are expected to yield a large number of exoEarth candidates, giving us the opportunity to statistically marginalize over the large uncertainties inherent to terrestrial planets to test important theories of habitability. Using a statistical methodology with future direct imaging missions will also help us maximize their scientific return, which is especially important in the event where we do not detect convincing evidence of life.

In Chapter 2, I will discuss testing the habitable zone concept, which relies on the existence of a stabilizing climate feedback, the silicate-weathering feedback, as discussed above. This stabilizing feedback is believed to have worked throughout Earth's history (e.g., Berner and Caldeira, 1997; Stolper et al., 2016), but it remains untested in an exoplanet context. I will discuss testing the silicate-weathering feedback statistically by measuring CO_2 on a large number of exoEarths, and will explore the feasibility of such a test for future direct imaging missions.

In Chapter 3, I will discuss a test for determining whether exoEarths tend to be Earth-like, in that they originate life that progressively oxygenates their atmospheres similarly to Earth (in a step-wise fashion). I will propose testing this statistically by searching for O_2 and O_3 on exoEarths with future direct imaging missions. I will explore the ability of these missions to constrain the fraction, f_E, of exoEarths that are Earth-like in the event of a null detection of O_2 or O_3 on all observed targets.

In Chapter 4, I will explore the detectability of O_2 and O_3 with future direct imaging missions using a 3D Global Climate Model including realistic cloud coverage. I will explore various levels of atmospheric O_2 to probe the range of atmospheric O_2 levels believed to have occurred through Earth's Phanerozoic and Proterozoic eras (e.g., Reinhard et al., 2017; Olson et al., 2018a).

1.6 Overview of Part 2: The Snowball Bifurcation on Habitable Tidally Locked Planets

In the second part of this dissertation, I will focus on habitable planets orbiting M-stars. M-stars are dimmer than G-stars, so that their habitable zones are at short enough orbital radii that planets within them are likely to become tidally locked in a synchronously rotating 1:1 spin:orbit configuration (Dole, 1964; Kasting et al., 1993a). This means that one side of the planet (the "dayside") always faces toward the star, the opposite side (the "nightside") always faces away. A tidally locked configuration may affect a planet's potential for habitability in different ways, such as forcing a large temperature contrast between the substellar and antistellar regions that could lead to atmospheric collapse on the night side if the atmospheric pressure is too low. Also, as described above, Snowball events can also influence planetary habitability as, on Earth, they have been correlated with sharp increases in the complexity of life (Kirschvink, 1992; Hoffman et al., 1998) and in the atmospheric oxygen concentration (Hoffman and Schrag, 2002; Laakso and Schrag, 2014, 2017b). Exploring the possibility of Snowball events on tidally locked planets is therefore important to further our understanding of their habitability.

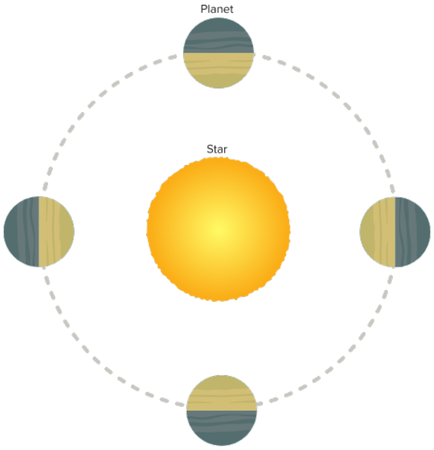

Figure 1.6: **A diagram of a tidally locked planet orbiting its star.** Tidally locked planets are synchronously rotating in a 1:1 spin:orbit configuration. One side of the planet (the "dayside") always faces toward the star, the opposite side (the "nightside") always faces away. Image credit: Smurrayinchester/Wikimedia Commons.

In Chapter 5, I will investigate the Snowball bifurcation on habitable tidally locked planets. I will show that tidally locked planets are unlikely to exhibit a Snowball bifurcation, regardless of stellar spectrum, and that they will smoothly transition from partial to complete ice coverage and back. A major implication of this finding is that habitable zone tidally locked planets with an active carbon cycle should not be found in a Snowball state for a geologically significant period of time.

In Chapter 6, I will explore whether realistic ocean heat transport can reintroduce the Snowball bifurcation for habitable tidally locked planets by destabilizing partially glaciated states. I will show that the lack of a Snowball bifurcation on tidally locked planets is robust to realistic levels of ocean heat transport.

In Chapter 7, I will consider the effect of tidal locking on limit cycling between Snowball and Warm climate states. Such limit cycling has been suggested to occur for rapidly rotating planets in the outer regions of the habitable zone with low CO_2 outgassing rates. I will show that tidally locked planets with an active carbon cycle will not experience limit cycling between Warm and Snowball states. Instead, they smoothly settle into “Eyeball” states with a small unglaciated substellar region.

Part I

Statistical Tests for Key Theories of Habitability with Future Direct Imaging Missions

CHAPTER 2

TESTING THE HABITABLE ZONE CONCEPT: DOES THE SILICATE-WEATHERING FEEDBACK WORK ON EXOEARTHS?

This chapter will be submitted for publication as: Checlair, J. H., Webber R. J., & Abbot, D. S. (2021). Testing the Habitable Zone Concept: Does the Silicate-Weathering Feedback Work on exoEarths?

2.1 Introduction

As discussed in Chapter 1, traditional habitable zone theory (Kasting et al., 1993a) assumes that the surface temperature of habitable planets is regulated inside the habitable zone, allowing for surface liquid water. Within the habitable zone, the silicate-weathering feedback (Walker et al., 1981a) regulates the atmospheric CO_2 of planets through a stabilizing negative feedback. If this feedback functions, we expect the CO_2 concentration of habitable terrestrial planets to increase as their irradiation decreases to maintain temperate surface temperatures. That said, there will be some variation in expected CO_2 concentration for a given planetary irradiation due to the various uncertainties in planetary parameters such as surface pressure, clouds, other greenhouse gases, surface albedo, gravity, and others, which may all affect surface temperature.

There is some non-definitive (e.g., Edmond and Huh, 2003) evidence that the silicate-weathering feedback has worked in Earth's history (e.g., Berner and Caldeira, 1997; Zeebe and Caldeira, 2008; Stolper et al., 2016; Caves et al., 2016; Macdonald et al., 2019; Isson et al., 2020; Penman et al., 2020). However, it remains untested in an exoplanet context. As we aim to characterize potentially habitable planets and generally deepen our understanding of habitability, it is crucial that we understand whether their climate is regulated by this negative feedback. The next generation of direct imaging instruments will allow us to test theories of habitability, such as the silicate-weathering feedback, by using large samples of Earth-sized, terrestrial planets orbiting within the habitable zones of their stars ("exoEarth candidates", EECs). In the search for life, the main advantage of exoplanets over solar system planets is their sample size (Cowan et al., 2015; Board et al., 2019). For example, while there is only one Jupiter, hundreds of hot Jupiters have already been detected. To exploit this opportunity, Bean et al. (2017) proposed a statistical approach to questions of planetary habitability, where we would exploit the number of exoplanets to statistically marginalize over both observational uncertainties and uncertainties intrinsic to terrestrial planets.

In this work, we investigate a statistical test for the operation of the silicate-weathering feedback using future instruments such as HabEx and LUVOIR. We explore the feasibility of such a test by determining the number of EECs for which CO_2 would have to be determined in order to indicate the existence of a CO_2-regulating feedback such as the silicate-weathering feedback on EECs. Such a test would exploit quick and cheap CO_2 measurements on a large sample of EECs in order to detect (or not) a negative trend between the insolation a planet receives and its atmospheric CO_2 concentration. As the total lifetime of future missions will be limited, it is important that we optimize the integration time spent on each planet. Performing quick measurements of CO_2 on a large number of EECs will allow us to test an important theory of habitability while minimizing the required observing time. A large number of those quick measurements will also allow us to statistically marginalize over uncertainties in planetary parameters and observational uncertainty.

Checlair et al. (2019a) performed a preliminary calculation of the number of EEC observations needed to test the silicate-weathering feedback. They found that 11 planets would need to be observed in their most optimistic case, and 51 in their most pessimistic case. However, they did not consider the instrumental uncertainty associated with LUVOIR and HabEx, which is expected to be an important component of the variation in the detected CO_2 for a given value of irradiation. Turbet (2020) used a toy model to show the expected trend between CO_2 and irradiation if the silicate-weathering feedback exists. They did this for planets inside the habitable zone as well as inside the inner edge and outside the outer edge. Lehmer et al. (2020) explored the number of detections necessary to distinguish a functioning silicate-weathering feedback from a log-uniform CO_2 distribution on habitable planets, and found that 83 habitable planets within the habitable zone would need to be observed. Their work differs from this work in a number of important aspects (see Section 2.4). Most importantly, they used a different statistical test than we did, as they only considered habitable planets within the habitable zone, and with $248 \text{ K} < T_s < 355 \text{ K}$. For these habitable planets, they explored how many observations would be needed to confirm that any negative trend between CO_2 and irradiation is due specifically to the silicate-weathering feedback. We discuss this further in Section 2.4.

This chapter is organized as follows. In Section 2.2 we outline step-by-step how we determine the number of EEC observations required to test the existence of the silicate-weathering feedback. First we discuss the generation of our preliminary atmospheric dataset (Section 2.2.1). Next, we show the scaling relationship for irradiation as a function of other planetary parameters derived from this dataset (Section 2.2.2). Then, we discuss how we calculate and incorporate observational noise into our model (Section 2.2.3). Finally, we outline how these pieces fit together to calculate the number of EEC detections required to test for a CO_2 regulating feedback (Section 2.2.4). In Section 2.3 we show how many EECs are required to test the CO_2-regulating feedback with HabEx and LUVOIR. In Section 2.4 we discuss implications and caveats of our work, and we summarize results in Section 2.5.

2.2 Methods

2.2.1 Data generation

To estimate the number of observations needed to detect the silicate-weathering feedback, we simulate an ensemble of repeated random observations of EECs using LUVOIR and HabEx.

First, we generate a large number of "data planets", where each data planet is associated with a different set of planetary parameters. We draw planetary parameters for each data planet from the distributions shown in Figure 2.1 and summarized in Table 2.1, for both an optimistic and a pessimistic case. The parameters we vary are: surface temperature ("$\mathrm{T_s}$", [K]), surface pressure ("$\mathrm{P_s}$", [bar]), carbon dioxide mixing ratio ("$\mathrm{CO_2}$", [mol/mol]), methane mixing ratio ("$\mathrm{CH_4}$", [mol/mol]), surface albedo ("α_s"), gravity ("g", [m/s^2]), relative humidity ("RH"), stratus cloud opacity ("τ_s"), cirrus cloud opacity ("τ_c").

Table 2.1: **Means and standard deviations of the planetary parameters for our optimistic and pessimistic cases.** The distributions in Figure 2.1 are based on these values.

Parameter	Mean	Optimistic standard deviation	Pessimistic standard deviation
Surface Temperature (T_s) [K]	288 (optimistic)	7.5	Uniform [273-373]
log Surface Pressure (P_s) [bar]	$\log_{10}(1)$	$0.5 \times \log_{10}(2)$	$2 \times \log_{10}(2)$
log CO_2 [mol/mol]	n/a	Uniform $[\log_{10}(10^{-6})$-$\log_{10}(10^{0})]$	Uniform $[\log_{10}(10^{-6})$-$\log_{10}(10^{0})]$
log CH_4 [mol/mol]	$\log_{10}(10^{-5})$	$1 \times \log_{10}(10)$	$1.5 \times \log_{10}(10)$
log Surface Albedo (α_s)	$\log_{10}(0.13)$	$0.5 \times \log_{10}(2)$	$2 \times \log_{10}(2)$
log Gravity (g) [m/s^2]	$\log_{10}(9.8)$	$0.5 \times \log_{10}(2)$	$0.5 \times \log_{10}(2)$
Relative Humidity (RH)	0.8	0.1	0.3
log Stratus Cloud Opacity (τ_s)	$\log_{10}(1.4)$	$0.5 \times \log_{10}(2)$	$2 \times \log_{10}(2)$
log Cirrus Cloud Opacity (τ_c)	$\log_{10}(0.3)$	$0.5 \times \log_{10}(2)$	$2 \times \log_{10}(2)$

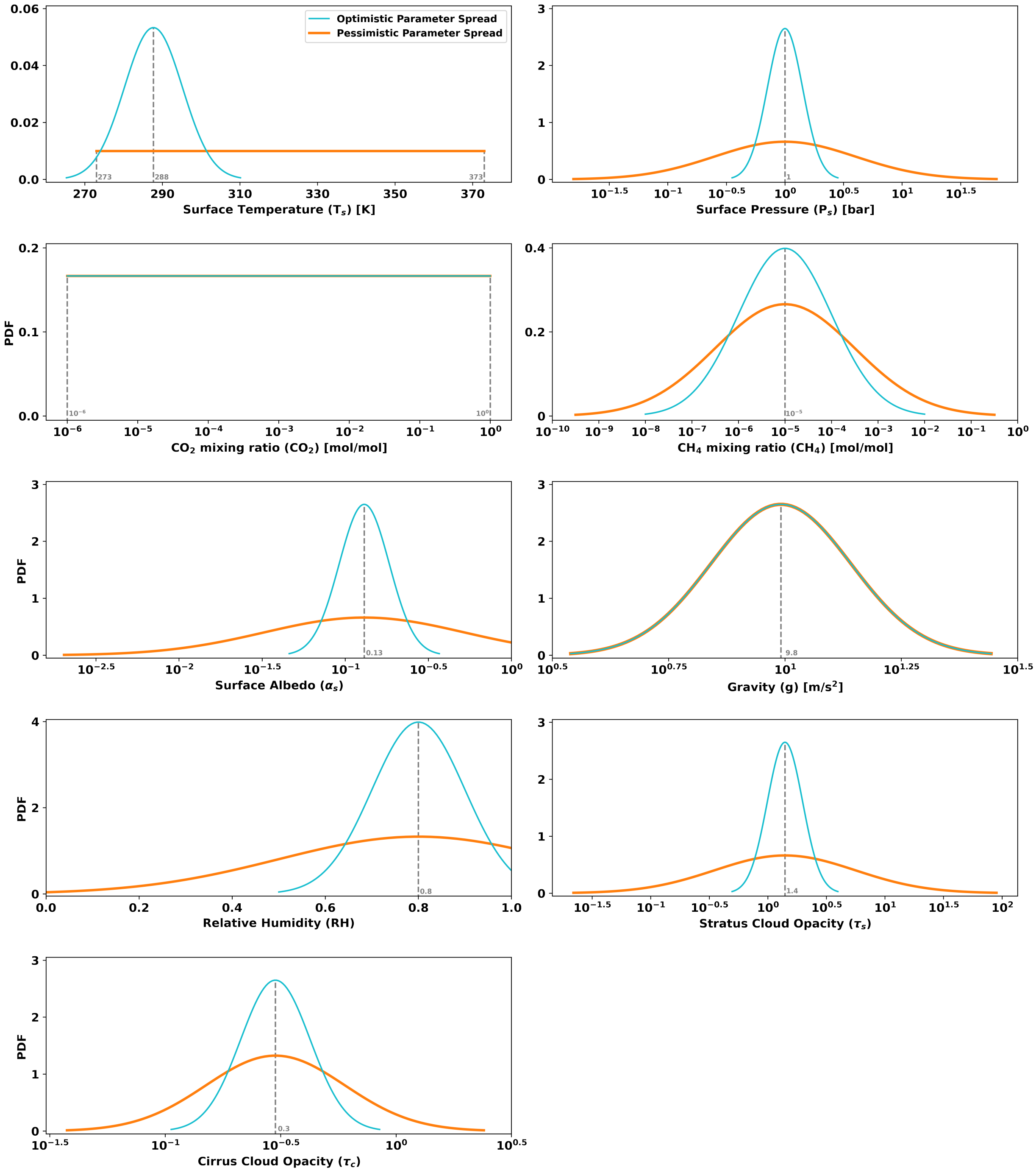

Figure 2.1: **Distributions of planetary parameters for an optimistic and a pessimistic case.** We draw from these distributions to build a preliminary dataset of "data planets" that are used to derive a relationship between S_{eff} and other planetary parameters.

We show the mean and standard deviations assumed for those distributions in Table 2.1.

For our parameters, we take Earth's current value as the mean of the distributions, except for the uniform distributions of CO_2 and of pessimistic T_s. For CH_4, we take the mean as 10× that of Modern Earth, which was the equilibrium concentration for most of Earth's history (Olson et al., 2018a). For our optimistic parameters, we choose standard deviations such that values are sampled close to that of the Earth's habitable history. For our pessimistic assumptions, we increase our standard deviations such that the values sampled represent habitable terrestrial planets with a wider variety of planetary conditions.

We draw the optimistic surface temperatures from the output of the geological carbon cycle model of Krissansen-Totton et al. (2018a), which is a reconstruction of Earth history that is consistent with a variety of geochemical data, and that considers uncertainties in silicate-weathering feedback parameterization. The pessimistic surface temperature range samples uniformly between 273 and 373 K. The 2-σ optimistic range for surface pressure is restricted to planets with surface pressures close to that of Earth, while the 2-σ pessimistic range of surface pressure includes planets with a surface pressure as low as $\sim 10 \times P_{\mathrm{Mars}}$ and as high as $\sim 0.2 \times P_{\mathrm{Venus}}$. We assume that planets with much smaller or larger surface pressures could be identified and removed from the EEC sample for this test, for example by measuring the strength of CO_2 pressure broadening or the slope of Rayleigh scattering (Feng et al., 2018). For CO_2 mixing ratio, we logarithmically sample a uniform range between 10^{-6} and 1 for both optimistic and pessimistic cases. Within 2-σ, this encompasses planets with a very low CO_2 concentration corresponding to a negligible radiative forcing, to planets with atmospheres dominated by CO_2. Both the optimistic and pessimistic 2-σ ranges of CH_4 mixing ratio sample values typical of Earth history (Olson et al., 2018a), with the pessimistic case being somewhat broader. The optimistic 2-σ range of surface albedo encompasses albedos of water and of most land surfaces, while the pessimistic 2-σ range encompasses all possible surface albedos including that of a snowball. We assume that surface gravity scales with planetary radius and sample planets half the radius of Earth (Mars) to twice the radius of Earth (Super-Earths) within the 2-σ ranges of both pessimistic and optimistic cases. For surface relative humidity, the 2-σ optimistic case samples humidities typical of habitable planets with some surface liquid water, while the 2-σ pessimistic case samples planets that would be either saturated or desiccated (Abe et al., 2011). The mean cloud opacities are those that obtain modern Earth's top-of-atmosphere OLR and albedo for a thin layer of cirrus or stratus clouds in the Spectral Mapping Atmospheric Radiative Transfer (SMART) model (Meadows and Crisp, 1996).

We sample these distributions using a Sobol sequence, which allows us to fill the parameter space more evenly than independent sampling (e.g., Kocis and Whiten, 1997; Kollig and Keller, 2002). For each data planet, we then use CLIMA (Kopparapu et al., 2013) to generate temperature-pressure profiles, and mixing ratio profiles of CO_2, CH_4, H_2O, and N_2, assuming an orbital distance of 1 AU. CLIMA is a 1D radiative-convective model that uses a two-stream approximation for radiative transfer. CLIMA solves for convective lapse rates with the formulation from Ingersoll (1969), assuming a moist adiabat with two condensable species (H_2O and CO_2). CH_4 is assumed to be well mixed. For the stratosphere, CLIMA balances total emitted infrared flux with total absorbed solar flux for each atmospheric layer, assuming radiative equilibrium.

Next, we use SMART to calculate the effective irradiation a planet would need to receive to maintain the given conditions. SMART is a line-by-line radiative transfer model that allows us to accurately calculate radiative fluxes, including the effects of clouds. To do this, we use the CLIMA mixing ratio and temperature-pressure profiles as input and run SMART for each set of parameters drawn for each data planet for both our optimistic and pessimistic cases. We include the stratus and cirrus cloud optical depths drawn from our sets of parameters in Figure 2.1. We then run SMART for each data planet at 1 AU to calculate the outgoing longwave radiation (OLR), as well as the outgoing ($S^{\uparrow}$) and incoming ($S^{\downarrow}$) top-of-atmosphere (TOA) solar radiation. From these variables, we calculate (Kasting et al., 1993a) the effective irradiation each data planet would receive as

$$
\mathrm{S_{eff}} = \frac{\mathrm{OLR}}{\left(1 - \mathrm{S}^{\uparrow}/\mathrm{S}^{\downarrow}\right)} \tag{2.1}
$$

At this stage, we therefore have a set of data planets, each with a set of parameters (T_s, P_s, CO_2, CH_4, α_s, g, RH, τ_s, and τ_c) and a corresponding effective irradiation. We generate 100 data planets for our optimistic case, and 200 for our pessimistic case.

We illustrate these data planets in Figure 2.2, where we show the relationship between CO_2 mixing ratio and S_{eff} for our optimistic and pessimistic datasets, as well as the corresponding surface temperature of each data planet. In our optimistic case, the expected downward trend between CO_2 mixing ratio and S_{eff} is visible by eye, as the variance in parameters is relatively small. In our pessimistic case, the downward trend is more difficult to detect by eye, but can be uncovered through statistical analysis (2.2.2).

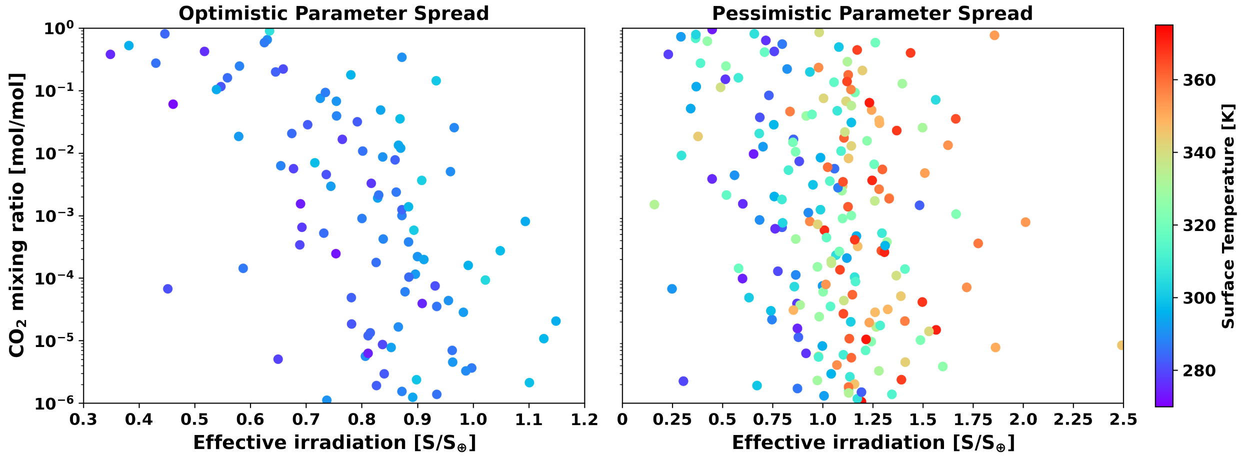

Figure 2.2: **CO_2 mixing ratio and effective irradiation for data planets, with associated surface temperature values.** Left: Optimistic parameter spread (Figure 2.1's blue curves), Right: Pessimistic parameter spread (Figure 2.1's orange curves).

2.2.2 CO_2 vs. S_{eff} scaling relationship

In this section, we derive optimistic and pessimistic scaling relationships for the effective irradiation as a function of the planetary parameters. We note here that we choose to build a model that predicts S_{eff} from other variables, rather than predicting CO_2, as we assume that S_{eff} is a deterministic function of the other parameters. This follows from the way we built our data set by computing S_{eff} from various sets of parameters. This linear model will later allow us to build a large interpolation grid from which we interpolate for CO_2 based on a set of drawn parameters (see Section 2.2.4).

We apply two separate linear regression techniques with the goal of obtaining robust models for S_{eff} using a sparsified set of predictor variables. As our first linear regression technique, we use the sparsity-promoting elastic net (Zou and Hastie, 2005; Pedregosa et al., 2011) to model S_{eff} as a function of T_s, $\log P_s$, $\log CO_2$, $\log^2 CO_2$, $\log CH_4$, $\log \alpha_s$, $\log g$, RH, τ_s, and τ_c. We set the elastic net penalization to be $\alpha = 0.075$, which reduces the set of 10 predictor variables to just $4 - 8$ predictors with nonzero fitted coefficients.

We remove from consideration any variables with fitted coefficients of zero. By reducing the number of variables in this way, we reduce the risk of overfitting and produce a more robust inference (Bishop, 2006). In both optimistic and pessimistic cases, we find that the elastic net keeps all the variables that are most strongly correlated with S_{eff} (see Figure 2.3 for barplots of correlations).

After promoting sparsity using the elastic net, we next apply a second linear regression technique — ordinary least squares (OLS) — to model S_{eff} as a function of the reduced set of predictor variables. In the optimistic case, the elastic net + OLS approach yields a fitted model

$$\begin{aligned} S_{\mathrm{eff}} = &-2.20 + 0.00953 \times T_s - 0.477 \times \log P_s \\ &- 0.147 \times \log CO_2 - 0.0154 \times \log^2 CO_2. \end{aligned} \tag{2.2}$$

We find that this scaling relationship is able to explain 76.2% of the variance in S_{eff}, and we model the remaining variance by adding Gaussian noise to this equation with a scaling

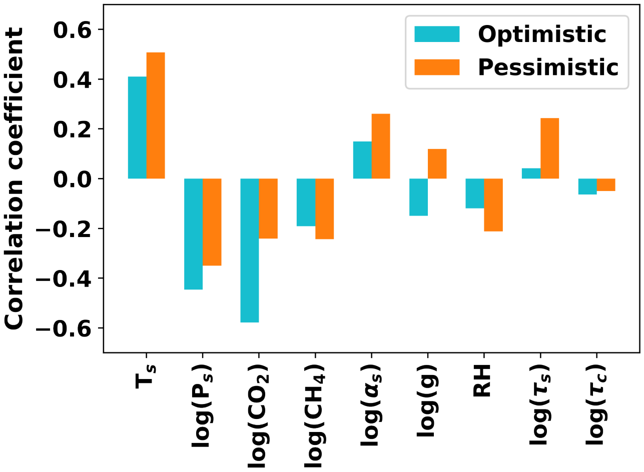

Figure 2.3: **Correlations between S_{eff} and other planetary parameters for 100 optimistic and 200 pessimistic data planets.** In the optimistic case of parameter spread, T_s, $\log P_s$, $\log CO_2$ are predictor variables for S_{eff}. In the pessimistic case of parameter spread, T_s, $\log P_s$, $\log CO_2$, $\log CH_4$, $\log \alpha_s$, RH, and τ_s are predictor variables for S_{eff}.

factor of 0.0813.

In the pessimistic case, we obtain a different fitted model

$$\begin{aligned} S_{\text{eff}} = &- 0.933 + 0.00639 \times T_s - 0.166 \times \log P_s \\ &- 0.0864 \times \log CO_2 - 0.00801 \times \log^2 CO_2 \\ &- 0.0289 \times \log CH_4 + 0.181 \times \log \alpha_s \\ &- 0.347 \times RH + 0.143 \times \log \tau_s. \end{aligned} \tag{2.3}$$

Compared to the optimistic model, there are many more predictor variables in the pessimistic model, which reflects the increased significance of CH_4, α_s, RH, and τ_s when predicting S_{eff}. Yet despite the larger number of predictor variables, the pessimistic model explains comparatively less of the variance in S_{eff} (58%) and we model the remaining variance by adding Gaussian noise with a scale factor of 0.249.

We emphasize that S_{eff} has a negative dependence on $\log CO_2$ in both optimistic and pessimistic models, but this dependence is weaker in the pessimistic model. The S_{eff}-CO_2 relationship is the single most important feature in our models, as it heavily influences the detectability of the silicate-weathering feedback.

2.2.3 Observational noise

To accurately model the instrumental noise that can be expected from LUVOIR and HabEx, we derive a scaling relationship for CO_2 noise as a function of other planetary parameters. To do this, we use the Planetary Spectrum Generator (PSG) (Villanueva et al., 2018) to simulate reflectance spectra for LUVOIR and HabEx.

First, we draw parameters for new data planets from the distributions shown in Figure 2.1. We draw 33 data planets for LUVOIR-A, 33 data planets for LUVOIR-B, and 41 data planets for HabEx. Then, we also draw a distance (D) in parsecs from a uniform distribution between 1.3 and 20 pc for each of our data planets, as well as an orbital distance between 0.6 and 1.7 AU.

Given that the stratus and cirrus optical depths were originally obtained by tuning them to SMART for a modern Earth albedo, we similarly tune a cloud profile to PSG to match a modern Earth top-of-atmosphere albedo of 0.3. We take this cloud profile as our "mean" cloud profile, and vary it by a factor equivalent to the variation in τ_S in order to assign a 2D stratus cloud profile to each of our data planets.

Next, we use PSG to generate reflectance spectra for each data planet for LUVOIR-A, LUVOIR-B, and HabEx. To accurately model observations made with each of these instruments, we set up PSG following Checlair et al. (2021) (Table 1). We assume that CO_2 and CH_4 are well-mixed in the atmosphere, and also assume hydrostatic equilibrium so that using P_S and T_S as input is sufficient to build an atmospheric profile in PSG. We assume an exposure time of 1000 hours per target, which is a realistic upper limit for observatories such as LUVOIR and HabEx. Longer exposure times would in principle be possible, but they would likely hamper other mission science objectives. Future work will consider different assumptions for the exposure time per target based on the observatories' total lifetimes and estimated EEC yields. For each data planet's reflectance spectra, we output the total signal and the noise as a function of wavelength. Then, we increase $\log \mathrm{CO}_2$ for each of those data planets until the SNR between the two spectra is equal to 1. To calculate the SNR between two spectra, we first calculate the signal by taking the difference between the two spectra: the signal is higher when the spectra are more different. We then divide the signal by the noise that PSG simulates based on the chosen instrument to obtain the SNR as a function of wavelength. The total SNR is then the square root of the sum of the square of the SNRs (Lustig-Yaeger et al., 2019; Checlair et al., 2021):

$$\mathrm{SNR}_{\mathrm{total}} = \sqrt{\sum_{\lambda_i} (\mathrm{S}_{\lambda_i}/\mathrm{N}_{\lambda_i})^2}, \tag{2.4}$$

where S_{λ_i} and N_{λ_i} are the signal and the noise for each wavelength. We do this for LUVOIR-A, LUVOIR-B, and HabEx. This provides us with an upper noise estimate on $\log \mathrm{CO}_2$ for each of our data planets. We repeat this to calculate the lower noise estimate on $\log \mathrm{CO}_2$ by progressively lowering $\log \mathrm{CO}_2$ for each of the data planets until either the SNR between the two spectra is equal to 1, or $\log \mathrm{CO}_2$ reaches the minimal detectability threshold of 10^{-6} mol/ mol.

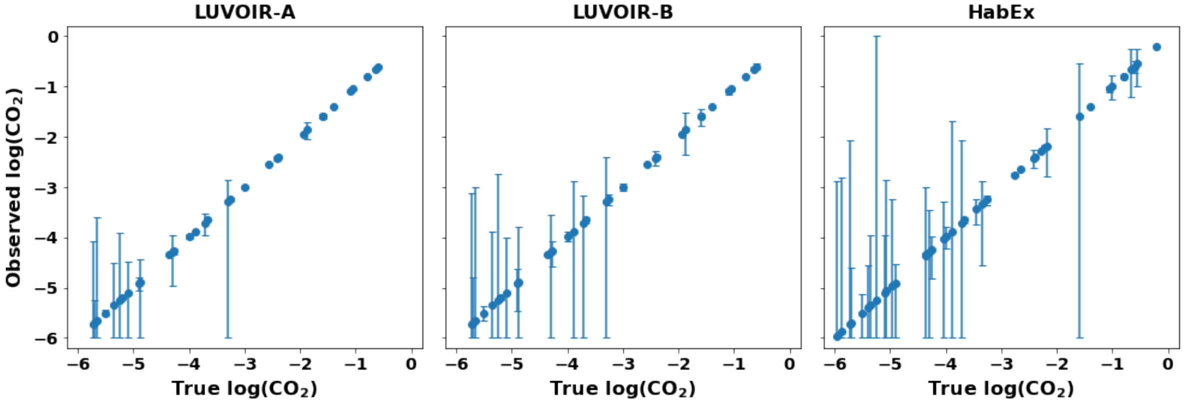

Figure 2.4: **Noise estimates for $\log \mathrm{CO}_2$ for LUVOIR-A, LUVOIR-B, and HabEx.** The positive and negative noise estimates are nearly symmetric about the true $\log \mathrm{CO}_2$ value for most points. The noise is generally largest for HabEx and smallest for LUVOIR-A.

As shown in Figure 2.4, the positive and negative noise estimates are nearly symmetric about the true $\log \mathrm{CO}_2$ value, and the noise is generally largest for HabEx and smallest for

LUVOIR-A. We model the observed $\log \mathrm{CO_2}$ using a linear Gaussian model

$$\text{Observed } \log \mathrm{CO_2} = \log \mathrm{CO_2} + \sigma\left(\log \mathrm{CO_2}, \mathrm{D}\right) \tag{2.5}$$

where the noise scale parameter $\log \sigma$ is taken to be a linear function of $\log \mathrm{CO_2}$ and distance D. We chose to use a simple linear model to prevent overfitting from a small data set.

To obtain specific models for $\log \sigma$ in the case of LUVOIR-A, LUVOIR-B, and HabEx, we apply ordinary least squares regression to predict the logarithm of the upper noise estimate as a function of $\log \mathrm{CO_2}$ and D. For LUVOIR-A, we find:

$$\log \sigma = -3.89 - 0.426 \times \log \mathrm{CO_2} + 0.155 \times \mathrm{D} \tag{2.6}$$

For LUVOIR-B, we find:

$$\log \sigma = -3.40 - 0.372 \times \log \mathrm{CO_2} + 0.180 \times \mathrm{D} \tag{2.7}$$

Lastly, for HabEx, we find:

$$\log(\sigma) = -2.92 - 0.349 \times \log \mathrm{CO_2} + 0.170 \times \mathrm{D} \tag{2.8}$$

These models confirm that the noise is slightly higher for LUVOIR-B than LUVOIR-A and slightly higher for Habex than for LUVOIR-B. In all models, the noise increases substantially with distance D and is largest when $\log \mathrm{CO_2}$ values are low. This effect is significantly stronger than the differences in noise estimates between the three instruments.

2.2.4 Simulations of observations

We begin by drawing N=10^6 values of $\mathrm{CO_2}$, $\mathrm{T_s}$, $\mathrm{P_s}$ for the optimistic case, and $\mathrm{CO_2}$, $\mathrm{T_s}$, $\mathrm{P_s}$, α_s, $\mathrm{CH_4}$, τ_s for the pessimistic case, all from the distributions shown in Figure 2.1. We then use the interpolation functions shown in equations 2.2 and 2.3 to calculate corresponding values of S_{eff} for each grid point. Then, we draw N (10^6) distances (in parsecs) for the simulated planetary systems. We draw these distances from a list of targets for each mission provided by Chris Stark (Stark et al., 2019), starting with the system closest to Earth and subsequently moving further away with each draw. Each draw is also weighted by the target's habitable zone yield estimate. We then add observational noise to each of the N drawn $\log CO_2$ values following equations 2.5−2.8. We do this for LUVOIR-A, LUVOIR-B, and HabEx. At this stage, we have grids of values for S_{eff} v.s. noisy $\log CO_2$ for all three missions for both our optimistic and pessimistic cases.

We then choose a number, N_p, of simulated observed EECs. For each of those EECs, we draw a random value for S_{eff} from a uniform distribution between 0.356 and 1.107. We chose these values to follow the boundaries of the habitable zone for an Earth-sized planet from Kopparapu et al. (2013). We assign a noisy $\log(CO_2)$ value to each S_{eff} value, based on our grids of S_{eff} v.s. noisy $\log CO_2$ values. We repeat this for each of the N_p simulated EECs. Using ordinary least squares, we then calculate the p-value for the $\log CO_2$ v.s. S_{eff} coefficient for the sample of N_p EECs. If the p-value is ≤ 0.05, we consider this iteration to be a positive detection of the silicate-weathering feedback. If the p-value is >0.05, we consider that the feedback cannot be detected. Note that we do this only if the slope of S_{eff} v.s. noisy $\log CO_2$ is negative, if it is positive we assume the feedback cannot be detected no matter the p-value. We repeat this process for 10^4 iterations. We take the fraction of the number of silicate-weathering feedback detections out of the 10^4 iterations. That is the statistical power attributed to the assumed number of simulated observed EECs.

2.3 Results

We show the probability of detecting the silicate-weathering feedback, if it exists, as a function of the number of observed EECs in Figure 2.5 for both our optimistic and pessimistic cases for LUVOIR-A, LUVOIR-B, and HabEx. For each of those cases, we calculate the minimum number of observed EECs necessary to have a 95% chance of detecting the feedback if it exists. We compare those minimum numbers to the expected number of observed EECs for LUVOIR-A, LUVOIR-B, and HabEx shown at the bottom of Figure 2.5. These distributions are based on data from Stark et al. (2019). They assume a nominal value of 4.5 for exozodi levels and of 24% for the EEC occurrence rate, and their means are reported in the HabEx and LUVOIR final reports (The LUVOIR Team et al., 2019; Gaudi et al., 2020).

First, we note that there is no significant difference in the probability of detecting the feedback for a given number of observed EECs with LUVOIR-A, LUVOIR-B, or HabEx. That is because the factors that primarily determine the magnitude of observational noise for CO_2 detections are the distance to the system (in pc) and the atmospheric CO_2 concentration. The noise increases significantly for greater distances and lower $\log CO_2$ values (see 2.2.3). In comparison, the differences in noise estimates between the three instruments are a weaker effect.

We find that to detect the silicate-weathering feedback with 95% confidence, we would need to observe 17 EECs in the optimistic case, and 34 EECs in the pessimistic case. Therefore, in the optimistic case, LUVOIR-A and LUVOIR-B respectively have a >99.9% and 96.6% chance of detecting the feedback. HabEx on the other hand is unlikely to detect the feedback (<0.01%) due to its smaller expected number of detected EECs. In the pessimistic case, LUVOIR-A has a 99.0% chance of detecting the feedback, LUVOIR-B a 12.3% chance, and HabEx a null chance.

2.4 Discussion

The silicate-weathering feedback is an important mechanism that is believed to regulate the surface temperature of Earth-sized terrestrial planets orbiting within the habitable zone (exoEarth candidates, or EECs). There is some evidence that it has functioned on Earth throughout its history, but it remains untested in an exoplanet context. Despite this, most habitability and exoplanet studies assume that it operates on EECs, and the boundaries of

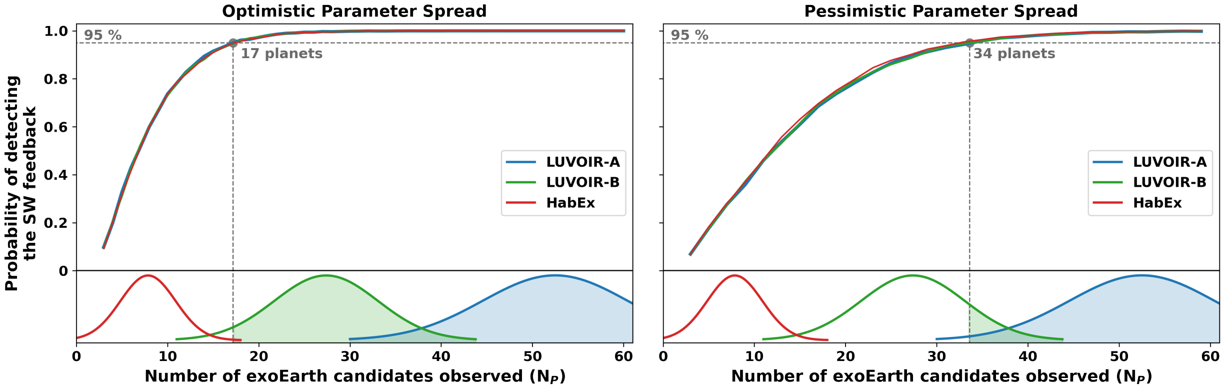

Figure 2.5: **Probability of detecting the silicate-weathering feedback if it exists on EECs, as a function of the number of observed EECs.** For the optimistic parameter spread, a minimum of 17 EECs must be observed to have a 95% chance of detecting the feedback, while 34 EECs must be observed for the pessimistic parameter spread. Both minimum numbers are applicable to LUVOIR-A (blue line), LUVOIR-B (green line), and HabEx with a starshade (red line), as there is no significant difference in their probability of detecting the feedback for a given number of observed EECs. The distributions at the bottom are the expected number of EEC detections for LUVOIR-A (blue distribution), LUVOIR-B (green distribution), and HabEx (red distribution) based on data from Stark et al. (2019) assuming nominal values for exozodi levels and for EEC occurrence rates.

the traditional habitable zone are based on its functioning. Future direct imaging instruments offer us the opportunity to test theories of habitability, such as the silicate-weathering feedback, by observing a large number of EECs. In this work, we explored the number of EECs that we would need to observe to test this feedback. To do this, we would make quick CO_2 measurements on a large sample of EECs, which would allow us to marginalize over uncertainties in planetary parameters and instrumental noise.

If the silicate-weathering feedback is common on exoEarths, we found that we would expect to detect it within 95% confidence if we observe at least 17 EECs in an optimistic case of planetary parameter spread, and 34 EECs in a pessimistic case, with either LUVOIR-A, LUVOIR-B, or HabEx. This minimum threshold limits which missions will realistically be able to test the silicate-weathering feedback, by virtue of their expected EEC yields. LUVOIR-A has the largest expected EEC yield of all three missions with a mean of 54 EECs, and has therefore a >99.9% and 99.9% chance of detecting the feedback for the optimistic and pessimistic cases respectively. LUVOIR-B has a lower expected EEC yield with a mean of 28 EECs, and has a 96.6% and 12.3% chance of detecting the feedback for the optimistic and pessimistic cases, respectively. HabEx, with the smallest EEC yield with a mean of 8 EECs, is unlikely to detect the feedback in either the optimistic or the pessimistic case. These results are not surprising, as a large sample of EECs will be required to conduct statistical studies such as this one. This is in line with Checlair et al. (2021), who showed that a mission with a higher expected yield of EECs will be more robust to the uncertainty in the value of the occurrence rate of EECs around Sun-like stars, $\eta_\oplus$, in statistically testing whether EECs are Earth-like.

The expected EEC yields of all three missions used in this work assume an occurrence rate of EECs around Sun-like stars of $\eta_\oplus = 24\%$. However, $\eta_\oplus$ is difficult to constrain as there have not yet been any Earth-sized exoplanets detected in the habitable zone of G-stars. Estimating it requires an extrapolation from Kepler data based on the population of small short-period planets. Based on this sample, estimates have been published in the literature that vary significantly (e.g., Catanzarite and Shao, 2011; Petigura et al., 2013; Burke et al., 2015; Mulders et al., 2018). Stark et al. (2019) adopted an occurrence rate of $\eta_\oplus = 24\%$ based on a community consensus study by the NASA funded Exoplanet Exploration Program Analysis Group (ExoPAG)'s Study Analysis Group 13 (SAG13). However, recent work from Pascucci et al. (2019) and Neil and Rogers (2020) argued that it may not be valid to extrapolate from the Kepler sample to estimate $\eta_\oplus$ as the dataset of short-period terrestrial planets is contaminated by stripped sub-Neptune cores. Including these potentially stripped sub-Neptune cores in the dataset causes overly optimistic estimates of $\eta_\oplus$. The estimate used by Stark et al. (2019) may therefore be overly optimistic. To re-evaluate $\eta_\oplus$, Pascucci et al. (2019) used exoplanets at larger separations and excluded short-period planets, which may be contaminated by stripped cores. They estimated $\eta_\oplus$ to be $\sim 5-10\%$. More recently, Neil and Rogers (2020) used Bayesian models fit to the Kepler data to calculate occurrence rates of planets in different regimes and found that using models with envelope mass loss predicts an order of magnitude drop in $\eta_{\oplus}$, down to $\sim 0.5\%$. The uncertainty in $\eta_{\oplus}$ may affect the expected EEC yield of future missions. If $\eta_{\oplus}$ is lower, the missions expected EEC yields will be lower. In this scenario, we may not be able to detect enough EECs to statistically test theories of habitability such as the silicate-weathering feedback. Further constraining $\eta_{\oplus}$ should be a priority to allow us to make predictions of the outcome of future observations.

In this work, we considered two cases of planetary parameter spread for EECs. In the optimistic case, we chose the means and standard deviations of the parameter distributions such that values are sampled close to that of the Earth's habitable history. In the pessimistic case, we increased the standard deviations such that the values sampled represent habitable terrestrial planets with a wider variety of planetary conditions (Krissansen-Totton et al., 2018a; Olson et al., 2018a; Abe et al., 2011; Rogers, 2015). For both of these cases, we use normal distributions to represent the parameter spread on EECs. However, in reality we have no prior as to whether a normal distribution is the correct way to characterize the real parameter spread of the EECs in our galaxy. Similarly, we used Earth's current values as the means of those distributions, as previous work by Krissansen-Totton et al. (2018a) points to habitable zone temperatures being constrained to a narrow temperate range. However, it is also possible that the real means lie at a different value. This may affect our results as a wider parameter spread could require a larger number of EECs to test the silicate-weathering feedback. However, our pessimistic case samples values that could represent any habitable zone terrestrial planet, regardless of whether they have a functioning feedback, and the 2-σ limits of those distributions ensure we are sampling rocky planets that may not resemble the Earth and may not have any sort of functioning feedback. Because of this, we expect that our pessimistic case can serve as a realistic upper limit to the number of EECs required to test the feedback.

Recent work by Lehmer et al. (2020) similarly explored the number of detections necessary to distinguish a functioning silicate-weathering feedback from a log-linear trend between CO_2 and S_{eff} on habitable planets. They found that 83 habitable planets within the habitable zone would need to be observed to reject a log-uniform distribution of CO_2 with 95% confidence. Here we discuss the ways in which their work differs from this work. Most importantly, their statistical test is different from ours, with different null and alternative hypotheses. Their null hypothesis was that if we observe habitable planets within the habitable zone and with a surface temperature constrained between 248 and 355 K, the observed CO_2 vs. S_{eff} trend will have a negative slope not necessarily associated with the silicate-weathering feedback. Their alternative hypothesis was that the negative trend between CO_2 and S_{eff} needs to have a specific slope in order to be characteristic of the silicate-weathering feedback. To explore this, they drew N planets with a random CO_2 level and an S_{eff} within the habitable zone, and calculated the corresponding surface temperature for these N planets based on a fit from a climate model. They then rejected planets with $T_s < 248$K or $T_s > 355$K, and showed that there will be a negative trend between CO_2 and S_{eff} for the remaining habitable planets. To distinguish the silicate-weathering feedback from this log-uniform distribution on CO_2, they found that 83 habitable planets within the habitable zone and with 248 K $<$ $T_s < 355$ K would need to be observed. On the other hand, our null hypothesis is that there is no relationship between CO_2 and S_{eff} in the habitable zone. Our alternative hypothesis is that if we detect a negative trend between the two, it will be due to a regulatory mechanism between CO_2 and S_{eff}, although it will not prove that this regulation is due specifically to the silicate-weathering feedback as it is on Earth. In practice, carrying out Lehmer et al. (2020)'s test would require that we first observationally measure the surface temperature of planets to determine whether they fall within this habitable range. This may be difficult and would extend the exposure time necessary for each observation. In contrast, we explore a statistical test that would rely on quick and cheap CO_2 measurements on a large sample of EECs to allow for statistical marginalization over uncertainties. Other differences are that they thoroughly considered geochemistry in their modelling of the feedback, while we do not, and they vary geochemical parameters contained in their numerical carbonate-silicate model to model uncertainty. However, they do not vary other planetary parameters such as surface pressure, gravity, surface albedo, etc., which may impact the feasibility of detecting the silicate-weathering feedback. They also do not consider the effects of clouds, which may further impede CO_2 detections. Finally, they do not include a treatment of observational uncertainty, which we explore to provide estimates of CO_2 noise for observations with LUVOIR and HabEx.

A caveat of this work is that we are testing for whether EECs commonly have a functioning silicate-weathering feedback. However, it is possible that only a fraction of them do, while most do not. If that were the case, we may not be able to confirm the existence of the feedback on EECs by observing the minimum number of EECs proposed in this work. If that were the case, our definition of the habitable zone may not be as useful, as we would no longer be able to assume that EECs within the habitable zone limits are temperate. Without the negative feedback of the silicate-weathering cycle, an EEC would be temperate depending on its insolation and steady-state CO_2 concentration. This would severely reduce the number of potential targets in our search for habitable terrestrial planets.

2.5 Conclusions

In this work, we explored the feasibility of testing the silicate-weathering feedback on exoEarth candidates (EECs) using future direct imaging instruments such as LUVOIR and HabEx. Specifically, we calculated the number of EEC observations that would be necessary to effectively marginalize over uncertainties in planetary parameters and instrumental noise by measuring CO_2 as a function of irradiation on a large sample of EECs. We considered both an optimistic and a pessimistic case of planetary parameter spread. We also considered three different telescope designs: 15 m on-axis segmented-mirror LUVOIR-A, 8 m off-axis segmented-mirror LUVOIR-B, and 4 m off-axis monolithic-mirror HabEx with a starshade. The main conclusions of this chapter are:

1. If the silicate-weathering feedback is common on EECs, we expect to detect it within

95% confidence if we observe at least 17 EECs in an optimistic case of planetary parameter spread, and 34 EECs in a pessimistic case of planetary parameter spread, with either LUVOIR-A, LUVOIR-B, or HabEx. The optimistic parameter spread samples values close to that of the Earth's habitable history, while the pessimistic spread samples values that could represent habitable terrestrial planets with a wider variety of planetary conditions.

2. This minimum threshold limits which missions will realistically be able to test the silicate-weathering feedback based solely on their expected EEC yields.
    - LUVOIR-A has a >99.9% chance of detecting the feedback for the optimistic case, and a 99.9% chance of detecting it for the pessimistic case. This is due to its large expected EEC yield with a mean of 54 EECs.
    - LUVOIR-B, with an expected mean yield of 28 EECs, has a 96.6% chance of detecting the feedback for the optimistic case, and a 12.3% chance of detecting it for the pessimistic case.
    - HabEx, with an expected mean yield of 8 EECs, is unlikely (<0.01% chance) to detect the feedback in either the optimistic or the pessimistic case.

CHAPTER 3

PROBING THE CAPABILITY OF FUTURE DIRECT IMAGING MISSIONS TO SPECTRALLY CONSTRAIN THE FREQUENCY OF EARTH-LIKE PLANETS

This chapter was originally published as: Checlair, J. H., Villanueva, G. L., Hayworth, B. P. C., Olson, S. L., Komacek, T. D., Robinson, T. D., Popović, P., Yang, H., & Abbot, D. S. (2021). Probing the Capability of Future Direct-imaging Missions to Spectrally Constrain the Frequency of Earth-like Planets. *The Astronomical Journal, 161*(3), 150.

3.1 Introduction

A long-standing goal in astrobiology is to spectrally determine the presence of life via biosignatures in the atmosphere (Schwieterman et al., 2018). Here, we focus on perhaps the most robust biosignatures for G-star planets, O_2 and O_3 (e.g., Owen, 1980; Sagan et al., 1993; Des Marais et al., 2002; Meadows, 2008, 2017; Schwieterman et al., 2018). We find that O_3 is always easier to detect than O_2 at UV-VIS wavelengths, so we expect that O_3 is the main signal for an oxygenated atmosphere that will be used in future space telescope missions. Additionally, false positives are not considered in this work as our primary concern is to determine what conclusions could be drawn from a potential null detection of O_2 and/or O_3 on all of the detected planets.

As future instruments are being launched and developed, the consensus is that planets that are Earth-sized, terrestrial, and orbiting in the habitable zone of their stars are great targets for the search for life. We will refer to Earth-sized habitable zone planets as "exoEarth candidates" (EECs), although this name does not indicate that they are "Earth-like." We will call an "Earth-like planet" an EEC that develops Earth-like O_2-producing life that oxygenates its atmosphere roughly following Earth's oxygenation history. Following this statistical definition, Earth-like EECs would start at negligible levels of atmospheric O_2 such as Earth did during its Hadean and Archean eras, and progressively develop an oxygenated atmosphere. A number of Earth-like EECs would be expected to be found in a Hadean or Archean-like era and so to lack remotely detectable levels of O_2 and O_3 as Earth did during its Hadean and Archean eras. This definition of Earth-like EECs is therefore not meant to be used for individual planets, but instead is purely statistical. If we do not detect O_2 or O_3 on an individual planet, we cannot know whether it resembles Hadean or Archean Earth and will eventually develop an oxygenated atmosphere, or if it is sterile and never will. Instead we'll simply know that at this stage in its history it does not currently have remotely detectable levels of oxygen in its atmosphere.

We will refer to the fraction of EECs that are Earth-like as f_E. If EECs are generally unlikely to be Earth-like (low f_E), it could either mean that they usually do not originate Earth-like life in the first place, or that although they do originate life, O_2 levels tend to never increase past Archean-like levels (either because oxygenic photosynthesis is rare or because oxygenic photosynthesis does not always manifest as planetary oxygenation). In both scenarios, EECs would not statistically be considered Earth-like, and we will not detect O_2 or O_3. The question we are trying to answer is: *Could future direct imaging instruments, such as HabEx and LUVOIR, constrain the frequency of Earth-like EECs, even if they do not detect any?*

A critical consideration in this work is the possibility of mission-level false negatives: cases where it is common for EECs to be Earth-like but we do not detect O_2 or O_3 on any of them. We will be adopting a statistical approach to address this problem (Bean et al., 2017; Checlair et al., 2019a; Bixel and Apai, 2020). This means that we will not investigate false negatives on particular planets. Instead, we will try to determine whether there might be mission-level false negatives for a particular mission based on all of the information that we can gain from all of the EECs that this mission can be expected to observe. Even with a large sample of EECs, we may not detect O_2 or O_3 with either LUVOIR or HabEx if the origination of life is uncommon or if EECs do not generally develop oxygenic photosynthesis.

The frequency of life origination on habitable planets is highly uncertain (e.g., Sandberg et al., 2018), so this is a scenario that should be seriously considered. Because it is possible that Earth-like EECs are very rare, we should design an instrument that would discern this, rather than possibly being a mission-level false negative scenario.

Using a statistical methodology with future direct imaging instruments will maximize the scientific return of these missions by allowing us to test theories of planetary habitability. This article focuses on statistically testing whether EECs are generally Earth-like, which necessitates a large enough sample of EECs so that mission-level false negative scenarios are unlikely and that we may constrain f_E. In previous work, Bixel and Apai (2020) proposed statistically testing the "age-oxygen" correlation with future observatories to determine whether we could place constraints on the amount of O_2 on EECs given the system age. This would then allow us to prioritize systems of a certain age for characterization when a large sample of EECs is available. Bixel and Apai (2020) found that testing this hypothesis would require a large number of EECs (∼200 EECs if 10% of detectable EECs have detectable O_2 or O_3, ∼20-40 EECs if 50% of detectable EECs have detectable O_2 or O_3) and may be therefore only be possible with a LUVOIR-A-like instrument, which is expected to detect more EECs, assuming most EECs have detectable O_2 or O_3.

The occurrence rate of EECs ($\eta_\oplus$) is difficult to constrain as there have not yet been any Earth-sized exoplanets detected in the habitable zone of G-stars. Estimating it therefore requires an extrapolation from Kepler data based on the population of small short-period planets. Based on this sample, many different estimates have been published in the literature that vary significantly (e.g., Catanzarite and Shao, 2011; Petigura et al., 2013; Burke et al., 2015; Mulders et al., 2018). To come to a community consensus, the NASA funded Exoplanet Exploration Program Analysis Group (ExoPAG) led Study Analysis Group 13 (SAG13) to compile published occurrence rates from the literature and proposed average value of $\eta_\oplus$ with uncertainties (Belikov et al., 2017; Kopparapu et al., 2018). Based on the SAG13 study, Stark et al. (2019) adopted boundaries for planet radii of $8((a/1AU))^{-0.5}$ $R_\oplus \leq R \leq$

1.4 $R_\oplus$, and for semi-major axes of 0.95-1.67 AU, and integrated the SAG13 occurence rates over these boundaries to estimate $\eta_\oplus \sim 24\pm^{46}_{16}\%$. However, recent studies from Pascucci et al. (2019) and Neil and Rogers (2020) showed that extrapolating from that Kepler sample is problematic as it is contaminated by stripped sub-Neptune cores and this sample can therefore not be reliably used to estimate $\eta_\oplus$. This suggests that the estimate used by Stark et al. (2019) may be overly optimistic. Pascucci et al. (2019) re-evaluated $\eta_\oplus$ using exoplanets at larger separations and excluding short-period planets, which may be contaminated by stripped cores, and estimated $\eta_\oplus$ to be $\sim 5-10\%$. More recently, Neil and Rogers (2020) used Bayesian models fit to the Kepler data to calculate occurrence rates of planets in different regimes and found that using models with envelope mass loss predicts an order of magnitude drop in $\eta_\oplus$, down to $\sim$ 0.5%. In this work, we consider three estimates of $\eta_\oplus$: 24% (Stark et al., 2019), 5% (Pascucci et al., 2019), and 0.5% (Neil and Rogers, 2020); and we explore how these estimates affect the ability of future direct imaging missions to constrain the fraction of Earth-like EECs in the case of a null detection of O_2 and O_3 on all of the observed EECs.

This paper is organized as follows. In Section 3.2 we outline how we determine the number of EECs on which LUVOIR and HabEx could detect O_2 and/or O_3 and the constraints that could be placed on f_E in the case of a null detection. In Section 3.3 we first theoretically solve for the probability of a mission-level false negative scenario for any mean EEC yield. We then present the integration times necessary for LUVOIR and HabEx to detect O_2 and O_3 at 5-σ. Next, we present the number of EECs on which LUVOIR and HabEx could detect O_2 and/or O_3 for different values of $\eta_\oplus$. We end that section by discussing how we could use these observations to constrain the fraction, f_E, of EECs that are Earth-like and how this may be affected by the adopted estimate of $\eta_\oplus$. In Section 3.4 we discuss some implications and caveats of our work, and we summarize results in Section 3.5.

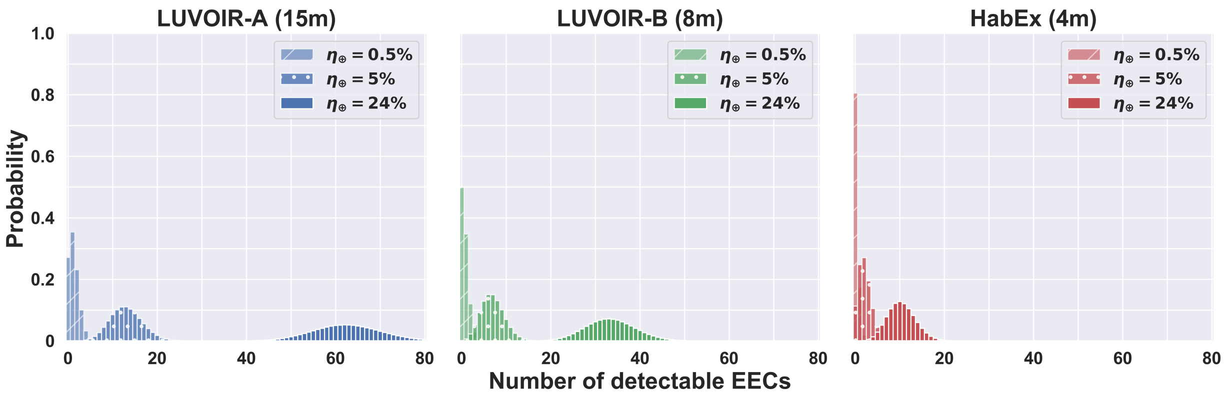

Figure 3.1: **Probability distributions of the number of EECs that would be detected by 15 m on-axis segmented-mirror LUVOIR-A (left), 8 m off-axis segmented-mirror LUVOIR-B (center), and 4 m off-axis monolithic-mirror HabEx (right). For $\eta_\oplus = 5\%$, there is an 11% chance of not detecting a single EEC with HabEx. For $\eta_\oplus = 0.5\%$, there is a 27%, 50%, and 81% chance of not detecting any EECs with LUVOIR-A, LUVOIR-B, and HabEx, respectively.** All distributions assume a high instrumental throughput. Histograms are based on data from Stark et al. (2019). Solid histograms assume $\eta_\oplus = 24\%$, following Stark et al. (2019), dotted histograms assume $\eta_\oplus = 5\%$, following Pascucci et al. (2019), and barred histograms assume $\eta_\oplus = 0.5\%$, following Neil and Rogers (2020).

3.2 Methods

3.2.1 *Overview*

To estimate the distribution of the number of detected Earth-like EECs, we perform Monte Carlo simulations where we consider an ensemble of many repeated HabEx and LUVOIR experiments. For each Monte Carlo realization, we draw the number of planets, $\mathrm{N_p}$, detected by each instrument and we assign to each detected planet a distance from Earth and an age that are used to determine whether O_2 and O_3 are detectable on the planet. Below, we first explain how we draw $\mathrm{N_p}$ and then we explain how we draw age and distance.

We consider four different mission designs: 15 m on-axis segmented-mirror LUVOIR-A, 8 m off-axis segmented-mirror LUVOIR-B, 4 m off-axis monolithic-mirror HabEx with a starshade (“HabEx/SS”, where “SS” refers to HabEx’s starshade, the complete proposed HabEx mission) and 4 m off-axis monolithic-mirror HabEx without a starshade (“HabEx/no-

SS", a proposed descoped version of HabEx). We choose these designs because they bracket the range of reasonably likely space-based direct imaging missions over the next few decades. We use the results of Stark et al. (2019) for the expected number of detectable EECs, $\mathrm{N_p}$, for each mission design. These expected yields assume $\eta_\oplus = 24\%$. To consider lower estimates of $\eta_\oplus$, we perform Monte Carlo simulations by resampling the yield estimate data from Stark et al. (2019) and weighing each EEC draw by a factor of (5/24) for $\eta_\oplus = 5\%$ (Pascucci et al., 2019), and by a factor of (0.5/24) for $\eta_\oplus = 0.5\%$ (Neil and Rogers, 2020). The resulting distributions of N_p for LUVOIR-A, LUVOIR-B, and HabEx, for different values of $\eta_\oplus$, are shown in Figure 3.1. We note here that we draw values for the number of detectable EECs, $\mathrm{N_p}$, for both HabEx/SS and HabEx/no-SS from the same HabEx distribution in Figure 3.1's right panel. We set the exposure time to 1000 hours per planet, which is a realistic upper limit for observatories such as LUVOIR and HabEx. Observations may require a shorter integration time, while a longer one, although possible in principle, would likely hamper other mission science objectives.

For each Monte Carlo realization, we first draw a value for N_p from Figure 3.1 for each instrument. This is the number of planets that will be detected using either instrument for each Monte Carlo realization. We then draw an age for each planet from a uniform distribution between 4.54 Gyr old and 0 Gyr old, to cover Earth's history. The age we draw belongs to one of Earth's eras: Hadean (4.54-4 Gya, 11.9% probability of being drawn), Archean (4-2.5 Gya, 33.0% probability of being drawn), pre-GOE Proterozoic (2.5-2.3 Gya, 4.4% probability of being drawn), post-GOE Proterozoic (2.3-0.5 Gya, 39.7% probability of being drawn), Phanerozoic (0.5-0 Gya, 11.0% probability of being drawn). We then draw a distance in parsecs for each of these N_p planets. We draw these distances from a list of targets for each mission provided by Chris Stark (Stark et al., 2019), weighted by the habitable zone yield estimates, $\eta_\oplus$, for each target. Considering the planet's era and distance, we calculate the Signal-to-Noise Ratio (SNR) for O_2 and O_3 detections with each telescope design given an exposure time of 1000 hours. We define a detectability SNR threshold of 5.0 for O_2

and/or O_3 to be considered detectable, and we count the number of EECs on which this condition is met. We find that the SNR is always higher for O_3 for all the mission designs considered. We repeat this for 10^7 Monte Carlo realizations.

An important assumption we make is that EECs that are Earth-like develop life and atmospheric O_2 following the same trajectory as Earth did: Hadean, Archean, Proterozoic, Phanerozoic. This means that we assume $f_E = 1$ to determine whether there are any mission-level false negative scenarios under this assumption. We view this as a starting assumption that is necessary to make progress, rather than the most likely scenario. We also consider a wide range of Proterozoic O_2 levels, which allows us to investigate a large range of O_2 history scenarios. We assume that O_2 and O_3 are undetectable at Hadean, Archean, and pre-GOE Proterozoic levels. We also assume EECs remain inhabited for the current inhabited history of the Earth of ~3.8 Gyr (Schidlowski, 1988; Dodd et al., 2017). This of course would depend on the planet's position in its star's habitable zone, as this will determine the length of time the planet remains habitable (Kopparapu et al., 2013). Earth will only remain in its own habitable zone for ~1.75 Gyrs before entering a runaway greenhouse climate (Rushby et al., 2013). During this time, Earth's atmospheric CO_2 should decrease to very low values as a result of the silicate-weathering feedback so that oxygenic photosynthesis by land plants will eventually fail (Caldeira and Kasting, 1992). This would likely result in a major decrease in Earth's atmospheric O_2. Since the trajectory of Earth's future atmospheric O_2 levels is highly uncertain, here we simply draw O_2 levels from Earth's history but recognize this may be an optimistic assumption if atmospheric O_2 decreases in the future. Contrarily, our assumptions would be pessimistic if O_2 remains the same or increases as the Earth ages - as the fraction of time O_2 is detectable would likewise increase.

3.2.2 Planetary Atmosphere simulations

We start by generating atmospheric profiles appropriate for Earth throughout its history. We assume a cloud-free atmosphere for all the profiles. We do not generate profiles for the

Hadean and Archean, as O_2 and O_3 concentrations remain below $\sim 10^{-5}$ Present Atmospheric Level (PAL) for the Archean (Kasting et al., 1979; Pavlov and Kasting, 2002). For the Phanerozoic, we use empirical atmospheric profiles for the Modern Earth provided by NASA's MERRA-2 dataset (Gelaro et al., 2017; Villanueva et al., 2018). For the Proterozoic, we calculate the mixing ratio profiles using a one-dimensional, horizontally averaged photochemical model (Segura et al., 2007). The model has 35 long-lived chemical species, 16 short-lived chemical species, and 220 reactions. A two-stream approximation is used for radiative transfer, using a fixed zenith angle of 50 degrees. The model solves for the steady-state solution at each altitude layer, accounting for chemical reactions, photolytic reactions, and vertical transport parameterized using Earth-like eddy diffusion profiles (Segura et al., 2007; Harman et al., 2015a).

Proterozoic O_2 levels are poorly constrained. We repeat our calculations for several Proterozoic O_2 scenarios ranging from 10^{-5} to 10^{-1} PAL to survey the full range of estimates existing in the literature (Pavlov and Kasting, 2002; Planavsky et al., 2014; Lyons et al., 2014; Reinhard et al., 2017; Olson et al., 2018a). Here we note that the lower end of that range (10^{-5} PAL) is difficult to explain in biogeochemical and photochemical models if oxygenic photosynthesis was occurring at or near modern rates (Ozaki et al., 2019). The most likely range of Proterozoic O_2 may therefore be $10^{-4} - 10^{-1}$ PAL. We discuss the constraints on Proterozoic O_2 further in Section 3.4. Reinhard et al. (2017) and Olson et al. (2018a) also surveyed the existing literature for CO_2 and CH_4 estimates throughout Earth's history, and placed upper and lower bounds on their abundances during each era. They argued for stricter constraints on each of these species' mixing ratios, providing "preferred ranges" for the Proterozoic. We use the mid-point values of those "preferred ranges" for Proterozoic CO_2 ($\sim$2000 μbar) and CH_4 ($\sim$5 μbar). For our Proterozoic water vapor profile, we assume a moist adiabat with a fixed relative humidity of 0.8. We then calculate the O_3 profile based on our background atmosphere (assumed to be 1 bar with N_2 as the major constituent). We then calculate the temperature profile using CLIMA, a one-dimensional

Table 3.1: **Instrument parameters we used in PSG to simulate observations with LUVOIR-A, LUVOIR-B, HabEx/SS, and HabEx/no-SS. The throughput values for $T_{coronagraph}$ (coronagraph throughput) and T_{opt} (optical throughput) are representative average values over the wavelength ranges. We include details about all assumed throughputs in the Appendix.**

Parameter		LUVOIR-A	LUVOIR-B	HabEx/SS	HabEx/no-SS
Diameter		15 m	8 m	4 m	4 m
Wavelength	UV	0.2-0.515μm	0.2-0.515μm	0.2-0.45μm	0.35-0.45μm
Range	VIS	0.515-1.0μm	0.515-1.0μm	0.45-0.975μm	0.45-0.975μm
	NIR	1.0-2.0μm	1.0-2.0μm	0.975-1.8μm	0.975-1.8μm
Resolution	UV	7	7	7	7
	VIS	140	140	140	140
	NIR	70	70	40	40
Exozodi Level (rel. to Solar Sys.)		4.5	4.5	4.5	4.5
Contrast		1×10^{-10}	1×10^{-10}	1×10^{-10}	2.5×10^{-10}
IWA [λ/D]	UV	4	3.5	39 mas	2.5
	VIS	4	3.5	58 mas	2.5
	NIR	4	3.5	104 mas	2.5
Read noise [e-]	UV	0	0	0.008	0.008
	VIS	0	0	0.008	0.008
	NIR	2.5	2.5	0.32	0.32
Dark noise [e-/s]	UV	3e-5	3e-5	3e-5	3e-5
	VIS	3e-5	3e-5	3e-5	3e-5
	NIR	0.002	0.002	0.005	0.005
$T_{coronagraph}$		0.27	0.46	0.7	0.55
T_{opt}	UV	0.13	0.13	0.38	0.09
	VIS	0.21	0.21	0.27	0.15
	NIR	0.3	0.3	0.36	0.15

radiative convective climate model (Kopparapu et al., 2013). As the Proterozoic has less O_3 than Phanerozoic Earth, there is a smaller temperature inversion in the stratosphere. We set the surface albedo to 0.3 for all of our atmospheric profiles.

3.2.3 Simulated Observations

We use the Planetary Spectrum Generator (PSG)[1] (Villanueva et al., 2018) to simulate observations with 15 m on-axis segmented-mirror LUVOIR-A, 8 m off-axis segmented-mirror LUVOIR-B, 4 m off-axis monolithic-mirror HabEx with a starshade ("HabEx/SS") and 4 m off-axis monolithic-mirror HabEx without a starshade ("HabEx/no-SS"). For all instruments we set the exposure time to 1000 hours. We choose the instrument parameters based on their reported values in their respective Final Reports (The LUVOIR Team et al., 2019; Gaudi et al., 2020). We summarize these parameters in Table 3.1.

3.2.4 Signal-to-Noise Ratio (SNR) Calculations

To calculate the SNRs, we simulate two spectra: one absorbing spectrum with all atmospheric species, and one continuum spectrum with all atmospheric species except the chosen absorber (either O_2 or O_3). We calculate the signal by taking the difference between the two spectra: the signal is higher where the absorber has a stronger absorption feature compared to the continuum. We then divide the signal by the noise that PSG simulates based on the chosen instrument to obtain the SNR as a function of wavelength, which is positive only at wavelengths where the absorbing gas absorbs. The total SNR for O_2 or O_3 is then the square root of the sum of the square of the SNRs (Lustig-Yaeger et al., 2019):

$$\mathrm{SNR}_{total} = \sqrt{\sum_{\lambda_i} (\mathrm{S}_{\lambda_i}/\mathrm{N}_{\lambda_i})^2} \tag{3.1}$$

---

[1] https://psg.gsfc.nasa.gov

where S_{λ_i} and N_{λ_i} are the signal and the noise for each wavelength. We calculate the SNRs at 5, 10, 15, and 20 pc, and interpolate between those values for other distances between 5 and 20 pc. For distances below 5 pc or above 20 pc, we scale the SNRs as being inversely proportional to distance (Stark et al., 2014). To get a better idea of whether O_2 and O_3 would be detectable in real observations for our different assumptions, we first calculate the integration time necessary for the total SNR to be equal to 5.0 for an Earth-like planet at 5, 10, 15, and 20 pc (see Section 3.3.2). In our Monte Carlo realizations, we consider the observation of an EEC of a given age and at a given distance as a positive life detection if the SNR of either O_2 or O_3 is above the threshold of 5.0 (see Section 3.3.3), following Lustig-Yaeger et al. (2019).

3.3 Results

3.3.1 EEC yield required to avoid mission-level false negative scenarios

We calculate the probability of a mission-level false negative scenario for an imaginary mission with any yield of EECs. Let's consider two cases: 1) O_3 is detectable on every EEC at every distance, but only at modern levels; and 2) O_3 is detectable on every EEC at every distance, at both modern and Proterozoic levels. In case 1), O_3 is then detectable on 11% of detectable EECs, as Earth has spent 11% of its history in the modern era. In case 2), O_3 is detectable on 50.7% of detectable EECs, as Earth has spent 50.7% of its history in the Proterozoic and modern eras.

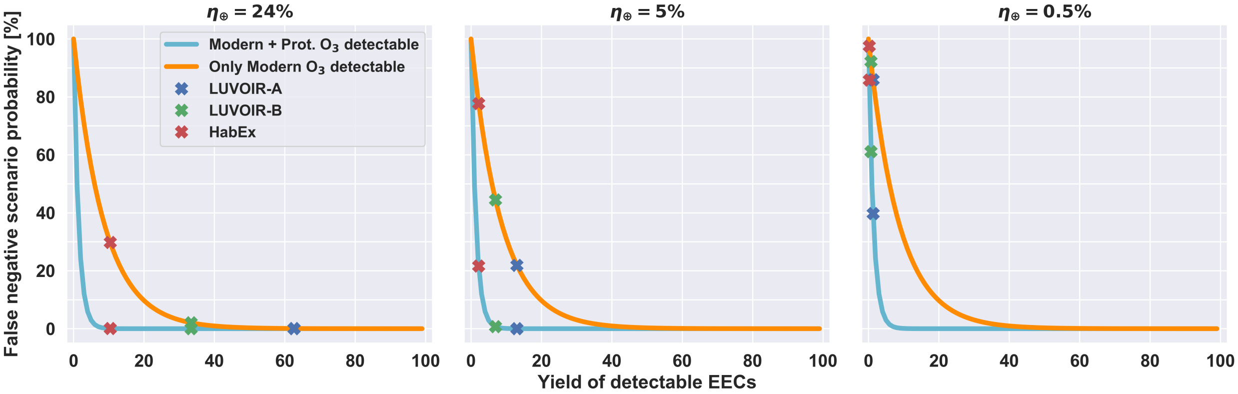

Figure 3.2: **Probability of a mission-level false negative scenario as a function of yield of detectable EECs for three different values of $\eta_\oplus$. For $\eta_\oplus = 24\%$, LUVOIR-A and LUVOIR-B have a <1% and <5% chance of a mission-level false negative scenario, respectively, even if they could only detect modern levels of O_3. On the other hand, HabEx needs to be able to detect Proterozoic levels of O_3 on every EEC to have <1% chance of a mission-level false negative scenario. For $\eta_\oplus = 5\%$, LUVOIR-A and LUVOIR-B must be able to detect Proterozoic levels of O_3 to have $< 1\%$ chance of a false negative scenario, while HabEx has >20% chance of one regardless of its ability to detect O_3. For $\eta_\oplus = 0.5\%$, all missions have probable mission-level false negative scenarios: ≥40%, ≥60%, and ≥85%, for LUVOIR-A, LUVOIR-B, and HabEx, respectively.** Orange line: Only modern levels of O_3 are detectable on every EEC; Cyan line: Phanerozoic and Proterozoic levels of O_3 are detectable on every EEC. Blue cross: LUVOIR-A's mean yield, Green cross: LUVOIR-B's mean yield, Red: HabEx's mean yield.

We can then find the probability of a mission-level false negative scenario using the percentage of detectable EECs with detectable O_3 for that imaginary mission and its mean EEC yield:

$$P = (1 - p)^N \tag{3.2}$$

where P is the probability of a mission-level false negative scenario, p is the percentage of EECs with detectable O_3, and N is the mean yield of EECs. We show the two theoretical curves for cases 1) and 2) in Figure 3.2. We have also superimposed the mean yields of LUVOIR-A, LUVOIR-B, and HabEx on top of the theoretical curves. Using these curves, we can determine the minimum number of EECs that would need to be detectable to have no chance of a mission-level false negative scenario. To have less than a 1% chance of a mission-level false negative scenario, in case 1), 39.5 EECs would need to be detectable. In case 2), 6.5 EECs would suffice as O_3 would be detectable on a greater percentage of them. Similarly, to have less than a 5% chance of a mission-level false negative scenario, in case 1), 25.7 EECs would need to be detectable, while in case 2), we would need to detect 4.2 EECs.

For $\eta_\oplus = 24\%$, LUVOIR-A's large EEC yield allows it to have less than a 1% chance of a mission-level false negative scenario even if it could only detect modern levels of O_3. Similarly, LUVOIR-B has less than a 5% chance of a mission-level false negative scenario even if it could only detect modern levels of O_3. On the other hand, HabEx needs to be able to reliably detect O_3 at Proterozoic levels to avoid a mission-level false negative scenario. That is due to its smaller EEC yield, which requires it to be able to detect lower levels of O_3.

For $\eta_\oplus = 5\%$, LUVOIR-A and LUVOIR-B need to be able to detect Proterozoic levels of O_3 to have less than a 1% chance of a mission-level false negative scenario. HabEx on the other hand will have a $> 20\%$ chance of a mission-level false negative scenario even if it could detect O_3 at modern and Proterozoic levels on every EEC.

For $\eta_\oplus = 0.5\%$, LUVOIR-A, LUVOIR-B, and HabEx would have a $\sim$40%, $\sim$ 60%, and $\sim$ 85% chance of a mission-level false negative scenario, respectively, even if they could detect O_3 at modern and Proterozoic levels on every EEC. Therefore, mission-level false negative scenarios are unavoidable for such a low estimate of $\eta_\oplus$.

3.3.2 Integration Times to detect O_2 and O_3 with LUVOIR and HabEx

We present the integration times required for a 5-σ detection of O_2 and O_3 at 5 pc for cloud-free atmospheres calculated using PSG (Villanueva et al., 2018) in Table 3.2 for LUVOIR-A, LUVOIR-B, HabEx/SS and HabEx/no-SS. The integration times calculated at 10, 15, and 20 pc can also be found in the Appendix. To calculate these integration times, we first calculate the SNRs for O_2 and O_3 detections using the method outlined in Section 3.2.4 with an exposure time of 1000 hours. We then calculate what the integration time would

Table 3.2: **Integration times [hrs] with LUVOIR-A (15 m), LUVOIR-B (8 m), HabEx/SS (4 m), and HabEx/no-SS (4m) to yield a 5-σ detection of O_2 and O_3 for an Earth-like planet without clouds at 5 pc for six different O_2 levels. Integration times calculated at 10, 15, and 20 pc can be found in the Appendix.**

O_2 Level	15 m LUVOIR-A	8 m LUVOIR-B	4 m HabEx/SS	4 m HabEx/no-SS
1 PAL	O_2: 0.75 hrs	O_2: 3.31 hrs	O_2: 12.8 hrs	O_2: 44.2 hrs
	O_3: 0.19 hr	O_3: 0.56 hr	O_3: 0.45 hr	O_3: 17.1 hrs
10^{-1} PAL	O_2: 4.24 hrs	O_2: 17.43 hrs	O_2: 65.9 hrs	O_2: 211.7 hrs
	O_3: 0.33 hr	O_3: 0.89 hrs	O_3: 0.41 hr	O_3: 62.8 hrs
10^{-2} PAL	O_2: 41.2 hrs	O_2: 167.9 hrs	O_2: 564.1 hrs	O_2: 2002.1 hrs
	O_3: 0.57 hrs	O_3: 1.48 hrs	O_3: 0.46 hr	O_3: 546.9 hrs
10^{-3} PAL	O_2: 658.0 hrs	O_2: 2679.8 hrs	O_2: 6772.4 hrs	O_2: 3.2×10^4 hrs
	O_3: 0.99 hrs	O_3: 2.59 hrs	O_3: 0.70 hr	O_3: 1463.9 hrs
10^{-4} PAL	O_2: 3.1×10^4 hrs	O_2: 1.2×10^5 hrs	O_2: 1.6×10^5 hrs	O_2: 1.5×10^6 hrs
	O_3: 4.15 hrs	O_3: 11.1 hrs	O_3: 2.22 hrs	O_3: 9.5×10^4 hrs
10^{-5} PAL	O_2: 2.7×10^6 hrs	O_2: 1.1×10^7 hrs	O_2: 1.0×10^7 hrs	O_2: 1.3×10^8 hrs
	O_3: 125.7 hrs	O_3: 338.2 hrs	O_3: 58.94 hrs	O_3: 2.0×10^7 hrs

have to be for these SNRs to be equal to 5.0:

$$\Delta t = 1000\ [\text{hrs}] \times \left(\frac{5}{\text{SNR}}\right)^2 \tag{3.3}$$

We consider six different O_2 levels: Phanerozoic (1 PAL), and five Proterozoic estimates (10^{-1} to 10^{-5} PAL).

In all cases for LUVOIR and HabEx, O_3 is easier to detect than O_2 due to its deep and broad feature between 0.2-0.3 μm (Hartley bands) and between 0.5-0.7 μm (Chappuis bands). Most importantly, O_3 is detectable at 5-σ with LUVOIR-A, LUVOIR-B, and HabEx/SS in under 500 hours even at very low estimates for Proterozoic O_2 levels (down to 10^{-5} PAL). For HabEx/no-SS, detecting O_3 without a starshade at 5 pc is difficult (>1000 hours) for Proterozoic O_2 levels below 10^{-2} PAL. We note here that the HabEx/SS integration times we calculated for O_2 are ~1-4 orders of magnitude larger than reported in the HabEx report (Figure 3.3-7 of Gaudi et al. (2020)) depending on the O_2 level due to the fact that our background atmosphere includes other absorbers such as O_3 and H_2O while that of the HabEx report only includes N_2. However, our calculations agree closely with simulations made using the Robinson et al. (2016) model when including additional background gases in their model (see Appendix for further details).

3.3.3 *Likelihood of detecting O_2 and/or O_3 with LUVOIR and HabEx*

$\eta_\oplus = 24\%$

We present the probability distributions of total O_2 and/or O_3 detections for LUVOIR-A (left-most), LUVOIR-B (center-left), HabEx/SS (center right), and HabEx/no-SS (right-most) in Figure 3.3, assuming $\eta_\oplus = 24\%$. As described in Section 3.2, we calculate the SNR of O_2 and O_3 for a given EEC at a certain distance and with a certain level of O_2 based on its age drawn from a uniform distribution. If either of these SNRs is above the threshold of 5.0 (for an exposure time of 1000 hours), we consider that EEC a positive O_2/O_3 detection. We note here that since O_3 is easier to detect than O_2 in all cases we considered (see Table 3.2), O_3 detectability is the limiting factor in determining whether O_2 and/or O_3 is detectable on a given EEC. We assume that $f_E = 1$ (all EECs are Earth-like), and determine whether there are any mission-level false negative scenario even under this optimistic assumption. We vary the Proterozoic O_2 from 10^{-5} to 0.1 PAL.

For LUVOIR-A, with Proterozoic levels of O_2 equal to or larger than 10^{-4} PAL, O_3 is detectable for EECs at all target distances for both modern and Proterozoic levels. Because of this, the first four rows of Figure 3.3 show the same distribution. The reason the distribution is offset from 62 (peak of Figure 3.1's left panel) is that O_2 and O_3 are undetectable for EECs in a Hadean or Archean era and so all EECs drawn to be of Hadean or Archean age will correspond to a null detection of O_2 and O_3. For these four levels of Proterozoic O_2, we find that LUVOIR-A has a 95% chance of detecting 21-43 Earth-like EECs (for $f_E = 1$). At Proterozoic O_2 levels of 10^{-5} PAL, O_3 is only detectable on EECs at close distances (<11.5

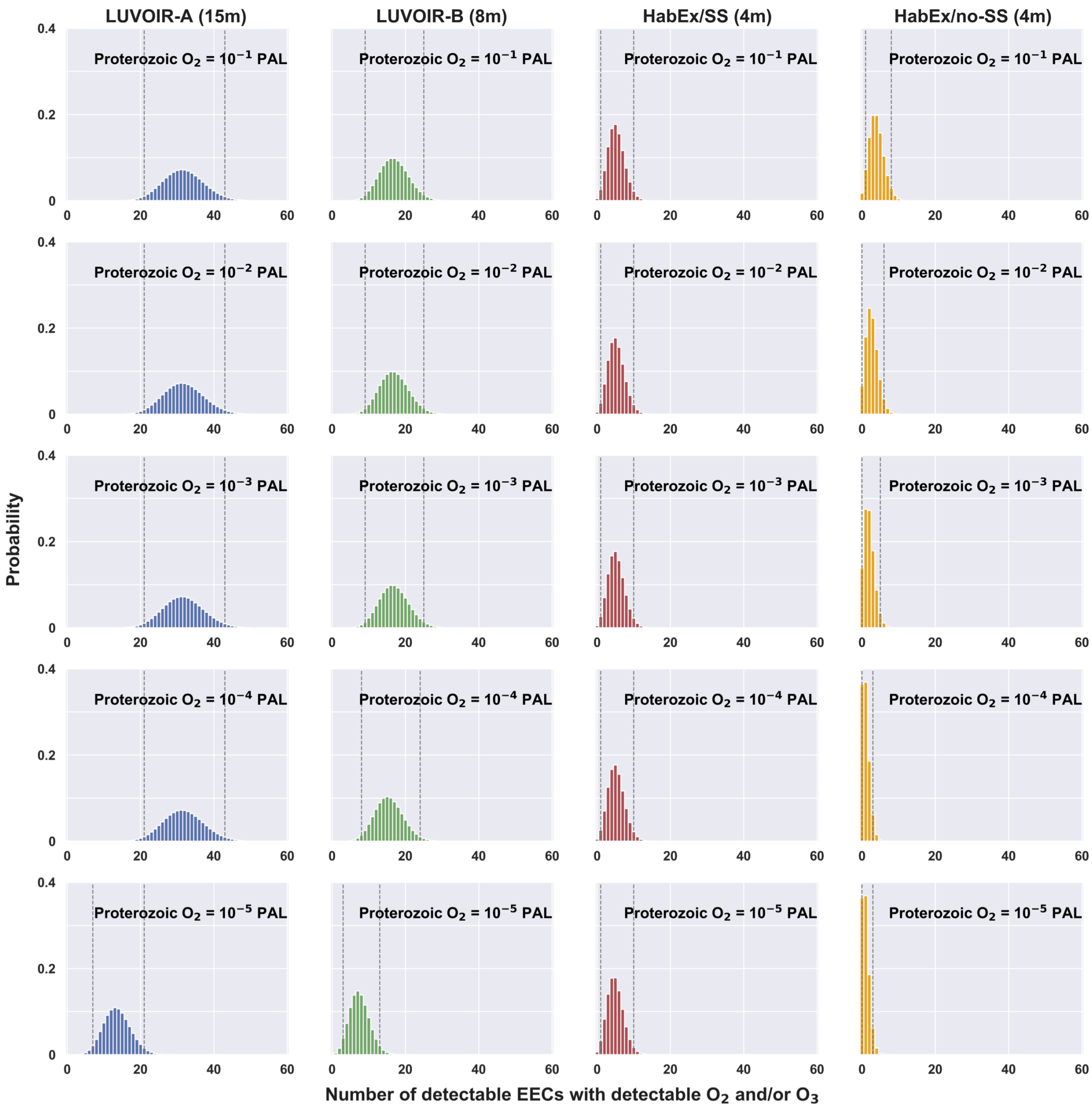

Figure 3.3: **Probability distributions of the number of EECs on which an O_2 and/or O_3 signature could be detected, for $\eta_\oplus = 24\%$, assuming $f_E = 1$ (all EECs are Earth-like). For LUVOIR-A and LUVOIR-B, there are no mission-level false negative scenarios, so O_2 and/or O_3 will be detected on a number of EECs if they are all Earth-like. For HabEx/SS, there is a small mission-level false negative scenario probability (0.5-0.6%). For HabEx/no-SS, there is a mission-level false negative scenario probability of 1.8% for 10^{-1} PAL, 6.6% for 10^{-2} PAL, 13.8% for 10^{-3} PAL, and 36.4% for $\leq 10^{-4}$ PAL of Proterozoic O_2.** Panels: LUVOIR-A (left-most), LUVOIR-B (center left), HabEx/SS (center right), and HabEx/no-SS (right-most). If the distribution reaches zero, there is a non-zero mission-level false negative probability: O_2 and/or O_3 are not detected on any EECs despite $f_E = 1$. We draw an age for EECs from Earth's history, and assume Hadean, Archean, and pre-GOE Proterozoic O_2 and O_3 levels are undetectable. Post-GOE Proterozoic O_2 concentrations range between 10^{-5} and 0.1 PAL. The vertical grey dotted lines represent the 95% confidence interval.

Table 3.3: **Probability of a mission-level false negative scenario for different assumptions of Proterozoic O_2 concentrations, assuming $\mathbf{f_E = 1}$, for $\eta_\oplus = $ 24%.** We draw a distance from the mission target list and an age for each EEC observed. A mission-level false negative scenario is defined as not detecting O_2/O_3 on any of the observed EECs even though we assume they are all Earth-like. The lowest possible mission-level false negative probability we can estimate is $< 10^{-5}$% given that we perform 10^7 Monte Carlo simulations.

Proterozoic O_2 Level	15 m LUVOIR-A	8 m LUVOIR-B	4 m HabEx/SS	4 m HabEx/no-SS
10^{-1} PAL	$<10^{-5}$%	$<10^{-5}$%	0.48%	1.8%
10^{-2} PAL	$<10^{-5}$%	$<10^{-5}$%	0.48%	6.6%
10^{-3} PAL	$<10^{-5}$%	$<10^{-5}$%	0.48%	13.8%
10^{-4} PAL	$<10^{-5}$%	$<10^{-5}$%	0.48%	36.4%
10^{-5} PAL	6.0×10^{-5}%	0.054%	0.63%	36.4%

pc), and therefore the distribution shifts toward zero due to the EECs that are further away and drawn to be of Proterozoic age. We find that LUVOIR-A has a 95% chance of detecting 7-21 Earth-like EECs for Proterozoic levels of 10^{-5} PAL (for $f_E = 1$). In the first four cases (Proterozoic O_2 between 0.1-10^{-4} PAL), the distribution of the number of EECs that have detectable O_3 is well above zero. For the case with Proterozoic levels of 10^{-5} PAL, the curve's end member is above zero with 5 as the smallest number of detected Earth-like EECs. There is therefore no mission-level false negative scenario for LUVOIR as a mission if $f_E = 1$: O_2 and/or O_3 will be detected on a number of EECs if they are all Earth-like.

For LUVOIR-B, with Proterozoic levels of O_2 equal to or larger than 10^{-3} PAL, O_3 is detectable for EECs at all target distances for both modern and Proterozoic levels. At lower Proterozoic O_2 levels, O_3 is only detectable at <19.1 pc for 10^{-4} PAL and at <8.1 pc for 10^{-5} PAL. We find that LUVOIR-B has a 95% chance (for $f_E = 1$) of detecting 9-25 Earth-like EECs for Proterozoic O_2 levels of 0.1-10^{-3} PAL, 8-24 for 10^{-4} PAL, and 3-13 for 10^{-5} PAL. Similarly to LUVOIR-A, for Proterozoic O_2 between 0.1-10^{-4} PAL, the distribution is well above zero, while for 10^{-5} PAL, the smallest number of detected Earth-like EECs is 1. Therefore, similarly to LUVOIR-A there are no mission-level false negative scenarios for LUVOIR-B as a mission if $f_E = 1$.

Table 3.4: **Same as Table 3.3 but for $\eta_\oplus$ = 5%.**

Proterozoic O_2 Level	15 m LUVOIR-A	8 m LUVOIR-B	4 m HabEx/SS	4 m HabEx/no-SS
10^{-1} PAL	0.13%	2.9%	33.3%	43.6%
10^{-2} PAL	0.13%	2.9%	33.3%	56.9%
10^{-3} PAL	0.13%	2.9%	33.3%	66.3%
10^{-4} PAL	0.13%	3.9%	33.3%	81.1%
10^{-5} PAL	5.8%	21.0%	35.3%	81.1%

Table 3.5: **Same as Table 3.3 but for $\eta_\oplus$ = 0.5%.**

Proterozoic O_2 Level	15 m LUVOIR-A	8 m LUVOIR-B	4 m HabEx/SS	4 m HabEx/no-SS
10^{-1} PAL	51.6%	70.3%	89.6%	91.0%
10^{-2} PAL	51.6%	70.3%	89.6%	94.5%
10^{-3} PAL	51.6%	70.3%	89.6%	96.0%
10^{-4} PAL	51.6%	72.4%	89.6%	97.9%
10^{-5} PAL	75.3%	85.6%	90.1%	97.9%

For HabEx/SS, with Proterozoic levels of O_2 equal to or larger than 10^{-4} PAL, O_3 is detectable for EECs at all target distances for both modern and Proterozoic levels. At 10^{-5} PAL, O_3 is only detectable on EECs at <13.9 pc. We find that HabEx/SS has a 95% chance of detecting 1-10 Earth-like EECs for all levels of Proterozoic O_2 considered (for $f_E = 1$). Because of the small number of EECs that HabEx can detect, the smallest possible number of Earth-like EECs for HabEx is 0. There is therefore a probability of a mission-level false negative scenario with HabEx even if $f_E = 1$, however it is only 0.5-0.6%.

For HabEx/no-SS, O_3 is only detectable at certain distances for high enough levels of Proterozoic O_2: <13.1 pc for 1 PAL, <9.8 pc for 10^{-1} PAL,<6.6 pc for 10^{-2} PAL, <4.1 pc for 10^{-3} PAL. At Proterozoic O_2 levels of 10^{-4} and 10^{-5} PAL, O_3 is not detectable at any distance. We find that HabEx/no-SS has a 95% chance (for $f_E = 1$) of detecting 1-8 Earth-like EECs for Proterozoic levels of 0.1 PAL, 0-6 for 10^{-2} PAL, 0-5 for 10^{-3} PAL, and 0-3 for 10^{-4} and 10^{-5} PAL. For all cases of Proterozoic O_2, HabEx/no-SS has a mission-level false negative scenario where we do not detect O_2 or O_3 on any of the EECs we observe even though $f_E = 1$. That mission-level false negative probability depends on the assumed

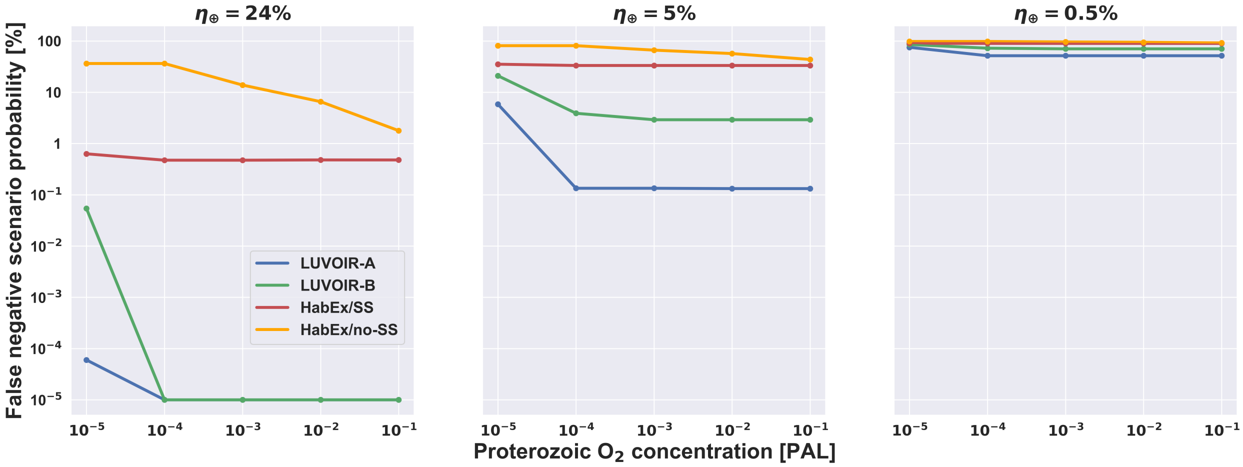

Figure 3.4: **Probability of a mission-level false negative scenario for different assumptions of Proterozoic O_2 concentrations, assuming $f_E = 1$, for $\eta_\oplus = 24\%$, 5%, and 0.5%. LUVOIR-A, given its large expected EEC yield, is most robust to lowering estimates of $\eta_\oplus$, allowing low probabilities of a false negative scenario for an $\eta_\oplus$ estimate down to 5%.** A mission-level false negative scenario is defined as not detecting O_2 or O_3 on any of the observed EECs even though we assume they are all Earth-like. The lowest possible mission-level false negative probability we can estimate is $<10^{-5}\%$ given that we perform 10^7 Monte Carlo simulations.

Proterozoic O_2 level, and in the cases we considered it is: 1.8% for 10^{-1}, 6.6% for 10^{-2}, 13.8% for 10^{-3}, and 36.4% for 10^{-4} and 10^{-5} PAL. We summarize these mission-level false negative probabilities in Table 3.3 and Figure 3.4.

$\eta_\oplus = 5\%$

For the lower $\eta_\oplus$ estimate of 5%, Figure 3.5 shows that all distributions are shifted toward zero compared to Figure 3.3. The most important difference compared to Figure 3.3 is the existence and greater likelihood of mission-level false negative scenarios for $f_E = 1$. LUVOIR-A still has negligible ($\sim 0.13\%$) mission-level false negative scenarios for Proterozoic O_2 levels $\geq 10^{-4}$ PAL, but has a mission-level false negative probability of 5.8% for Proterozoic O_2 of 10^{-5} PAL, for $f_E = 1$. LUVOIR-B has mission-level false negative scenario probabilities for every Proterozoic O_2 case (2.9% for $\geq 10^{-3}$, 3.9% for 10^{-4}, and 21.0% for 10^{-5} PAL), for $f_E = 1$. HabEx/SS and HabEx/no-SS have significantly greater mission-level false negative

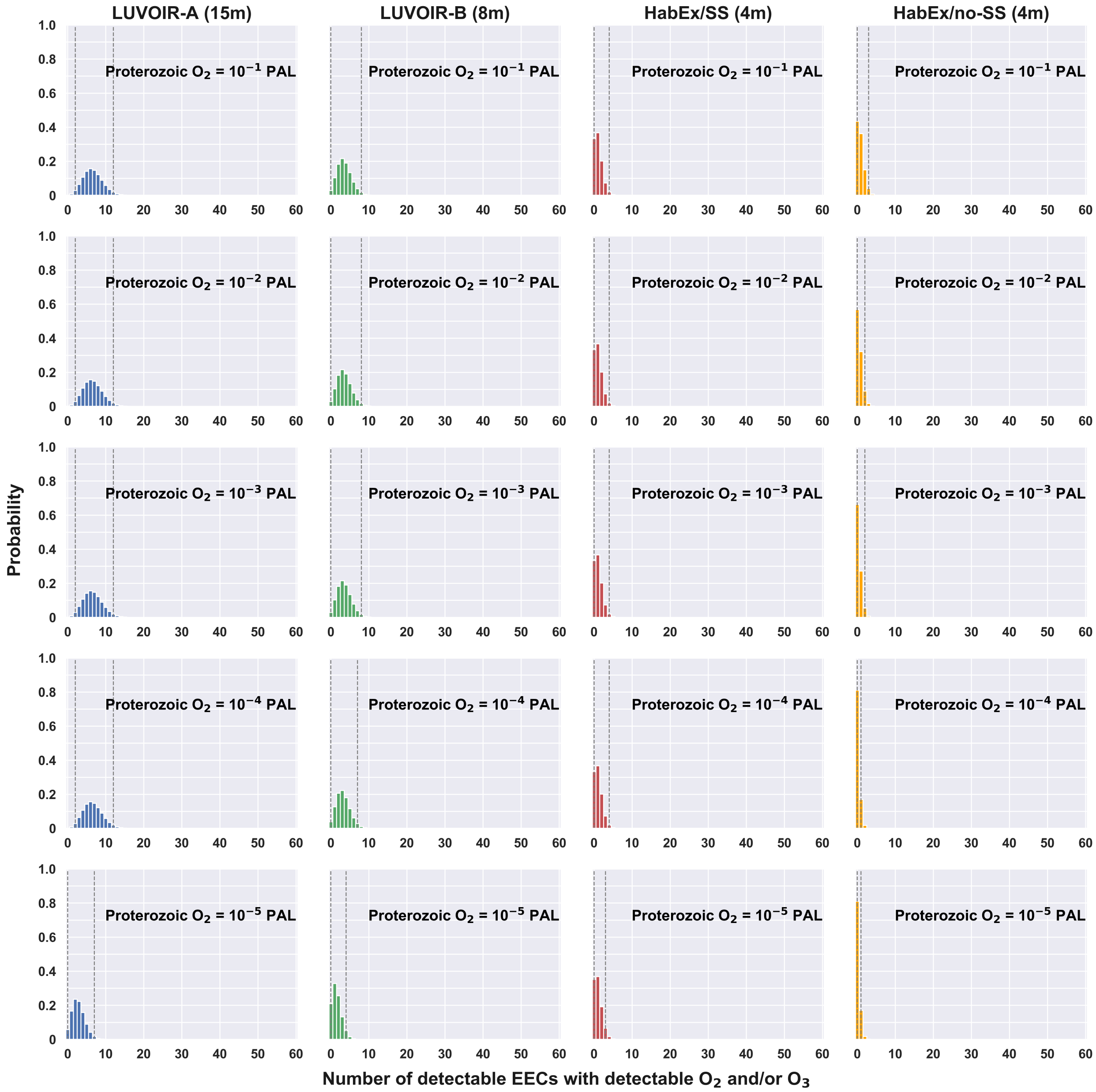

Figure 3.5: **Same as Figure 3.3 but for $\eta_\oplus = 5\%$, assuming $f_E = 1$. For LUVOIR-A, there are no mission-level false negative scenarios for Proterozoic $O_2 \geq 10^{-4}$ PAL. For Proterozoic O_2 of 10^{-5} PAL there is a 5% chance of a mission-level false negative scenario. For LUVOIR-B, there is a 1.4% chance of a mission-level false negative scenario for Proterozoic $O_2 \geq 10^{-3}$ PAL, a 2.3% chance for 10^{-4} PAL, and a 20.2% chance for 10^{-5} PAL. For HabEx/SS, there is a 34.2% chance of a mission-level false negative scenario for Proterozoic $O_2 \geq 10^{-4}$ PAL, and a 36.7% chance for 10^{-5} PAL. For HabEx/no-SS, the mission-level false negative probabilities are as follows: 46.9% for 10^{-1}, 61.6% for 10^{-2}, 71% for 10^{-3}, and 84.5% for $\leq 10^{-4}$ PAL of Proterozoic O_2.** Note that the scale of the y-axis is different than in Figure 3.3.

scenario probabilities. HabEx/SS has a 33.3% chance of a mission-level false negative probability for Proterozoic $O_2 \geq 10^{-4}$ and 35.3% for 10^{-5} PAL, for $f_E = 1$. HabEx/no-SS has a 43.6% chance of a mission-level false negative for Proterozoic O_2 of 10^{-1}, 56.9% for 10^{-2}, 66.3% for 10^{-3}, and 81.1% for $\leq 10^{-4}$ PAL, for $f_E = 1$. We summarize these mission-level false negative probabilities in Table 3.4 and Figure 3.4.

$\eta_\oplus = 0.5\%$

The lowest estimate of $\eta_\oplus$ predicts that EECs are rare enough that it will be difficult to detect them in the first place (see Figure 3.1's right panel), as there is a 27%, 50%, and 81% chance of not detecting any of them for LUVOIR-A, LUVOIR-B, and HabEx, respectively. Because of this, for $f_E = 1$, there is a 51.6% chance of a mission-level false negative scenario with LUVOIR-A for Proterozoic $O_2 \geq 10^{-4}$ PAL and 75.3% for Proterozoic O_2 of 10^{-5} PAL. LUVOIR-B has a 70.3% chance of a false negative for Proterozoic $O_2 \geq 10^{-3}$ PAL, 72.4% for 10^{-4} PAL, and 85.6% for 10^{-5} PAL, for $f_E = 1$. HabEx/SS has a 89.6% chance of a false negative for Proterozoic $O_2 \geq 10^{-4}$ PAL and 90.1% chance for Proterozoic O_2 of 10^{-5} PAL, for $f_E = 1$. HabEx/no-SS has a 91.0%, 94.5%, 96.0%, and 97.9% chance of a false negative for Proterozoic O_2 of 10^{-1} PAL, 10^{-2} PAL, 10^{-3} PAL, and $\leq 10^{-4}$ PAL, for $f_E = 1$. To summarize, if $\eta_\oplus = 0.5\%$, all missions that we considered will detect too few EECs to rule out false negative scenarios even if $f_E = 1$. We do not include a reproduction of Figures 3.3 and 3.5 for $\eta_\oplus = 0.5\%$ as most panels simply show high peaks at zero, but we summarize the mission-level false negative probabilities in Table 3.5 and Figure 3.4.

3.3.4 Using a null detection to constrain the fraction f_E of Earth-like EECs

In the highly likely scenario that only a fraction f_E of EECs are actually Earth-like, the number of planets on which we detect O_2/O_3 will be decreased by a factor f_E. For example, if only 10% of EECs are Earth-like ($f_E = 0.1$), assuming $\eta_\oplus = 24\%$, the peak of Figure 3.3's first row panel for LUVOIR-A would shift from 31 to 3.1. For HabEx/SS the peak of all panels would shift toward zero to create distributions with peaks at zero, making it unlikely that we will be able to detect O_2 or O_3 with HabEx/SS if f_E is low.

An instrument that lacks mission-level false negatives for $f_E = 1$, such as (for $\eta_\oplus = 24\%$) LUVOIR-A, LUVOIR-B, or HabEx/SS, will allow our observations to put a constraint on $\mathrm{f_E}$ even if we cannot detect O_2 or O_3. On the other hand, an instrument such as HabEx/no-SS will not allow us to make any inference about $\mathrm{f_E}$ in the event of a null detection, no matter the value of $\eta_\oplus$, as it could be caused by a mission-level false negative scenario even when $f_E = 1$. For missions lacking mission-level false negative scenarios when $f_E = 1$, how well we can constrain $\mathrm{f_E}$ depends on the mission and on the value of $\eta_\oplus$, and is a function of the number of detectable EECs and of the ability to detect various levels of O_3.

For different values of $\mathrm{f_E}$, we perform Monte Carlo simulations by resampling from the distributions in Figure 3.3 and weighing each draw by $\mathrm{f_E}$, resulting in the number of EECs with detectable O_2 or O_3 for that value of $\mathrm{f_E}$. We show the probability that at least 1 Earth-like EEC will have detectable O_2 or O_3 as a function of the fraction fo Earth-like EECs, $\mathrm{f_E}$, in Figure 3.6.

$\eta_\oplus = 24\%$

If we do not detect O_2 or O_3 on any EECs with LUVOIR-A, this null detection would mean that $\mathrm{f_E} \leq 0.094$ for Proterozoic O_2 levels above 10^{-4} PAL, and ≤ 0.22 for Proterozoic O_2 levels of 10^{-5} PAL. Therefore, a null detection with LUVOIR-A will constrain $\mathrm{f_E}$ with 95% confidence to $\leq 0.094 - 0.22$. Similarly, a null result with LUVOIR-B would mean that $\mathrm{f_E}$ is ≤ 0.18 for Proterozoic O_2 levels above 10^{-3} PAL, ≤ 0.19 for Proterozoic O_2 levels of 10^{-4} PAL, and ≤ 0.40 for Proterozoic O_2 levels of 10^{-5} PAL. Therefore, a null detection with LUVOIR-B will constrain $\mathrm{f_E} \leq 0.18 - 0.40$ with 95% confidence. HabEx/SS will also allow us to constrain $\mathrm{f_E} \leq 0.56$ for Proterozoic O_2 levels above 10^{-4} PAL, and ≤ 0.59 for Proterozoic O_2 levels of 10^{-5} PAL in the case of a null detection, all with 95% confidence. On the other hand, a null detection with HabEx/no-SS will not allow us to constrain $\mathrm{f_E}$ as there are mission-level false negative scenarios where we do not detect O_2 or O_3 even if all EECs are Earth-like. These potential constraints on $\mathrm{f_E}$ are summarized in Figure 3.7.

This also implies that we have a 95% chance of detecting O_2 or O_3 on at least 1 EEC with LUVOIR-A for $f_E > 0.094$, with LUVOIR-B for $f_E > 0.18$, and with HabEx/SS for $f_E > 0.56$ (all for Proterozoic $O_2 \geq 10^{-4}$ PAL, which is the likely lower limit of the Proterozoic O_2 range). However, a null detection is possible with HabEx/no-SS for any value of f_E.

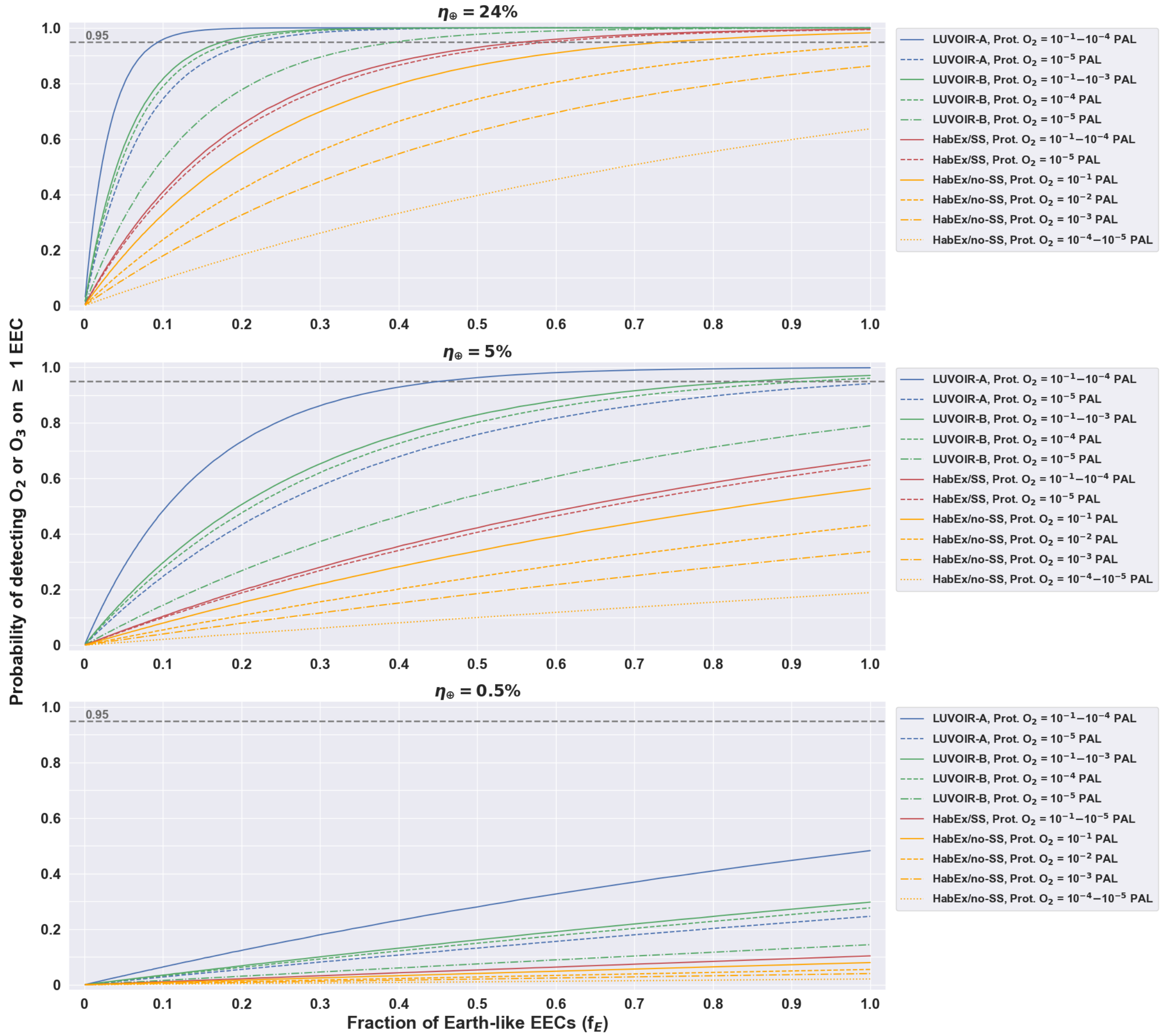

Figure 3.6: **Probability of detecting O_2 or O_3 on at least 1 EEC as a function of the fraction of Earth-like EECs (f_E), for $\eta_\oplus = 24\%$, 5%, and 0.5%. The intersection of each curve with the 95% vertical grey line denotes the upper limit that will be placed on f_E at 95% confidence in the event of a null detection of O_2 and O_3 on all observed EECs.** If the curve does not intersect the 95% grey line, a constraint cannot be placed on f_E in the event of a null detection due to the existence of mission-level false negative scenarios. For a given Proterozoic O_2 level, the mission with the highest expected number of detectable EECs allows for the best constraint to be placed on f_E.

$\eta_\oplus = 5\%$

A lower $\eta_\oplus$ estimate of 5% would also impact the extent to which we could constrain f_E in the case of a null detection. If we do not detect O_2 or O_3 on any EECs with LUVOIR-A, we could constrain $\mathrm{f_E}$ with 95% confidence to ≤ 0.45 for Proterozoic O_2 $\geq 10^{-4}$ PAL. However, for Proterozoic O_2 of 10^{-5} PAL, we will not be able to constrain $\mathrm{f_E}$ as there is a 6% chance of a mission-level false negative scenario. Similarly, a null detection with LUVOIR-B will allow us to constrain $\mathrm{f_E}$ with 95% confidence to ≤ 0.85 for Proterozoic O_2 $\geq 10^{-3}$ PAL, and to ≤ 0.92 for Proterozoic O_2 of 10^{-4} PAL, but we will not be able to constrain it at lower Proterozoic levels as there is a 21% chance of a mission-level false negative for Proterozoic O_2 of 10^{-5} PAL. HabEx/SS and HabEx/no-SS have a $33 - 35\%$ and $44 - 81\%$ chance of a mission-level false negative, respectively, and therefore will not allow us to constrain $\mathrm{f_E}$. These potential constraints on $\mathrm{f_E}$ are summarized in Figure 3.7.

This also implies that we have a 95% chance of detecting O_2 or O_3 on at least 1 EEC with LUVOIR-A for $f_E > 0.45$, with LUVOIR-B for $f_E > 0.85$. However, a null detection is possible with HabEx/SS and HabEx/no-SS for any value of f_E.

$\eta_\oplus = 0.5\%$

Using the lowest estimate of $\eta_\oplus = 0.5\%$ introduces the possibility of detecting no EECs in the first place, hence a null detection of O_2 and O_3 on all EECs is unlikely to help constrain $\mathrm{f_E}$. In this scenario, none of the missions would inform us on the likely value of $\mathrm{f_E}$ in the case of a null detection, and it is likely we would not detect O_2 or O_3 on any EECs even if they are all Earth-like.

3.4 Discussion

If EECs are all Earth-like in that they develop Earth-like oxygenic photosynthesis that oxygenates their atmosphere, we should detect O_2 or O_3 with LUVOIR-A, LUVOIR-B, and HabEx/SS (with starshade) as long as $\eta_\oplus$ is sufficiently large. For $\eta_\oplus = 24\%$, LUVOIR-A and LUVOIR-B have a negligible chance of a mission-level false negative scenario, where EECs are all Earth-like but we do not detect O_2 or O_3 on any of them. HabEx/SS similarly

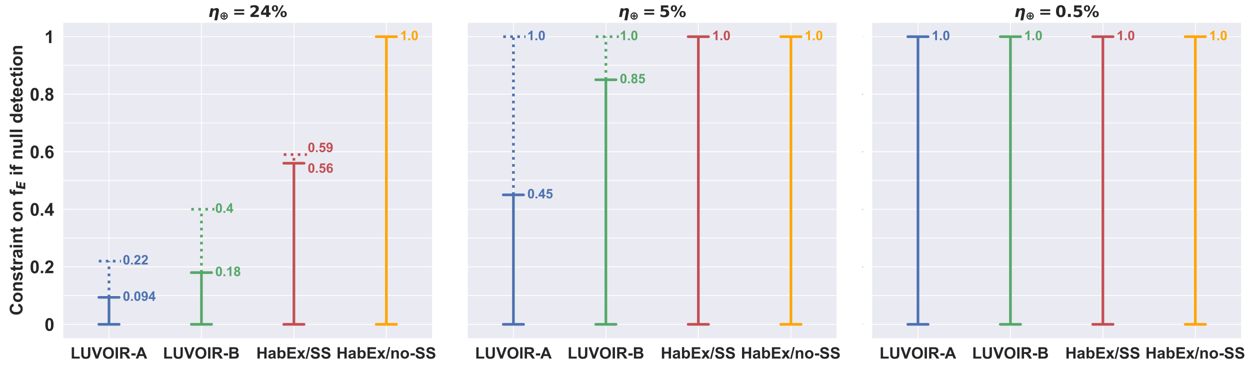

Figure 3.7: **Constraint that we will be able to place on f_E, with 95% confidence, in the case of a null detection where we do not detect O_2 or O_3 on any EECs for $\eta_\oplus = 24\%$, 5%, and 0.5%. These constraints also imply that for f_E greater than the upper limits, we have a 95% chance to detect O_3 on at least 1 EEC.** Solid lines: constraints for Proterozoic O_2 level of $10^{-1} - 10^{-4}$ PAL; Dashed lines: constraints for Proterozoic O_2 level of 10^{-5} PAL. An upper limit of 1.0 for the constraint on f_E means that there is a $\geq 5\%$ chance of a mission-level false negative scenario, where we do not detect O_2 or O_3 on any EECs even if they are all Earth-like, and so f_E cannot be constrained. Note that LUVOIR-B's constraint on f_E will be $\leq 19\%$ for $\eta_\oplus = 24\%$ and Proterozoic O_2 level of 10^{-4} PAL, and $\leq 92\%$ for $\eta_\oplus = 5\%$ and Proterozoic O_2 level of 10^{-4} PAL.

has only a very small chance of such a false negative. For $\eta_\oplus = 5\%$, for Proterozoic $O_2 \geq 10^{-4}$ PAL, LUVOIR-A similarly has a negligible chance of a mission-level false negative scenario, and LUVOIR-B's chance of a mission-level false negative scenario is $< 4\%$, while HabEx/SS has a 33% chance of one. For $\eta_\oplus = 0.5\%$, it is reasonably likely that no EEC will be detected in the first place: there is a 27%, 50%, and 81% chance that LUVOIR-A, LUVOIR-B, and HabEx do not detect any. As a result, all missions have a significant probability of a mission-level false negative scenario even if all EECs are Earth-like ($f_E = 1$). For any value of $\eta_\oplus$, HabEx/no-SS has a significant chance of a mission-level false negative scenario, showing therefore that a starshade is crucial to HabEx's design.

If we detect O_2 or O_3 on a number of EECs that is lower than the number we would expect if $f_E = 1$, we will be able to constrain the fraction of EECs that are actually Earth-like (f_E) with all instruments. In the event that we do not detect O_2 or O_3 on any EECs we will also be able to constrain f_E to different extents based on the mission and based on the value of $\eta_\oplus$. For $\eta_\oplus = 24\%$, LUVOIR-A, LUVOIR-B, and HabEx/SS will allow us to constrain

$f_E \leq 0.094$, $f_E \leq 0.18$, and $f_E \leq 0.56$, respectively, with 95% confidence, for Proterozoic O_2 levels $\geq 10^{-4}$ PAL. On the other hand, HabEx/no-SS will not allow us to constrain f_E due to the existence of mission-level false negative scenarios. For $\eta_\oplus = 5\%$, LUVOIR-A and LUVOIR-B will allow us to constrain $f_E \leq 0.45$ and $f_E \leq 0.85$, respectively, while HabEx/SS and HabEx/no-SS will not allow us to constrain f_E. For $\eta_\oplus = 0.5\%$, none of the missions will allow us to constrain f_E due to the high probability of mission-level false negative scenarios. This illustrates the fact that a mission with a higher expected yield of EECs is more robust to the uncertainty in the value of $\eta_\oplus$, and that further constraining $\eta_\oplus$ should be a priority to allow us to make predictions of the outcome of future observations.

As HabEx and LUVOIR are still mission concepts, their specifications are not yet finalized. The number of EECs that we can detect with either instrument depends on the set of specificities we choose from Stark et al. (2019). Particularly, our analysis was performed using a high throughput scenario for both instruments, which is likely optimistic. We considered a pessimistic scenario where we use a low throughput, and recreated Figure 3.1. For $\eta_\oplus = 24\%$, we found that the number of EECs that we could detect with LUVOIR-A decreases from 62 to 50, with LUVOIR-B from 33 to 27, and with HabEx from 10 to 8. In this low throughput scenario, the peaks of Figure 3.3 are shifted to the left as well. For example, for $\eta_\oplus = 24\%$ and Proterozoic O_2 levels of 10^{-5} PAL, this increases the mission-level false negative scenario probability from 0.6% (in the high throughput scenario) to 1.8% for HabEx/SS, and from 36% to 45% for HabEx/no-SS. On the other hand, assuming a low throughput does not introduce any mission-level false negative scenario for LUVOIR-A and LUVOIR-B for this estimate of $\eta_\oplus$.

Exoplanet atmospheres are expected to be diverse in their composition, even if they are inhabited by Earth-like life. In this work, we considered an Earth-like background atmosphere in our SNR calculations that includes gases such as O_2, O_3, CO_2, H_2O, N_2, and CH_4. However, EEC atmospheres may contain different gases that could affect the SNRs of O_2 and O_3 features. Observations would require a full atmospheric retrieval study to confirm O_2 and O_3 detections (Feng et al., 2018).

The HabEx/SS integration times we calculated for O_2 are greater than those reported in the HabEx report (Gaudi et al., 2020). We find that the integration times necessary to detect O_2 and O_3 with HabEx/SS are 1-4 orders of magnitude larger than in their study (see their Figure 3.3-7). The reason for this is that we included various gases such as O_3, CO_2, and H_2O in our background atmosphere, while the HabEx report calculations only considered N_2 as a background gas. Because of this, in their calculations the difference between the continuum (N_2 only) and the absorption spectrum (N_2 and O_2) is large at $\sim$0.2 μm as N_2 does not absorb there. In Earth-like atmospheres, species such as O_3 and H_2O absorb at these short wavelengths. This minimizes the difference between the continuum spectra (without O_2) and the absorber spectra (with O_2) at 0.2 μm. Therefore, we do not expect the signal to be large at 0.2 μm for Earth-like planets. We note however that our calculations agree closely with simulations made using the Robinson et al. (2016) model when including additional background gases (see Appendix for further details).

The level of O_2 during the Proterozoic is highly uncertain (Reinhard et al., 2017; Olson et al., 2018a), with lower and upper constraints from various geochemical records and modeling efforts that vary by four orders of magnitude from 10^{-5} to 10^{-1} PAL (Pavlov and Kasting, 2002; Planavsky et al., 2014; Lyons et al., 2014; Olson et al., 2018a). The lower limit on Proterozoic O_2 is inferred from the end of mass-independent fractionation of S isotopes in the wake of the "Great Oxidation Event." The upper limit of 10^{-1} PAL comes from the observation that the deep ocean remained anoxic throughout the Proterozoic, implying that surface environments were only mildly oxygenated. More recent work by Planavsky et al. (2014) provides an upper limit of 10^{-3} PAL by leveraging the absence of Cr isotope fractionation in Proterozoic marine sediments. Although such geochemical data constrains the range of Proterozoic O_2 between 10^{-5} and 10^{-3} PAL, the low end of that range is difficult to explain in biogeochemical and photochemical models if oxygenic photosynthesis was occurring at or near modern rates (Ozaki et al., 2019). A number of previous studies that considered the detectability of Proterozoic O_2 remained above an O_2 threshold of approximately 10^{-3} PAL (Reinhard et al., 2017; Schwieterman et al., 2018; Gaudi et al., 2020). We considered Proterozoic O_2 levels as low as 10^{-5} PAL to span the full range of estimates existing in the literature and permissible by existing geochemical data, and to allow us to consider every possible scenario in the search for biosignatures with HabEx and LUVOIR, but we note that the low estimate of 10^{-5} PAL may be less likely than higher estimates.

In this work, we have based the definition of "Earth-like" on the premise that EECs would oxygenate roughly following Earth's oxygenation trajectory, and have used Earth history as a prior. However, the timing and timescale of oxygenation on Earth are not well understood, and it is possible that EECs would follow a different oxygenation trajectory. For example, newly formed planets may have different initial compositions than the Earth did 4 Gyr ago, and therefore, may experience a different oxygenation timeline, even in the presence of Earth-like life. If Earth is rare and EECs never oxygenate past Archean levels, then as per our statistical definition of "Earth-like", EECs would not be statistically Earth-like. Similarly, if only a small fraction of EECs oxygenate past Archean levels, then statistically only a small fraction of EECs are Earth-like and f_E is small. This is something we will be able to test with a mission that includes a large-aperture telescope, as whether or not we detect O_3, it will allow us to infer a maximum value of f_E. We have also explored other possible oxygenation scenarios for $\eta_{\oplus} = 24\%$: 1) Proterozoic O_2 levels are as high as modern levels, and 2) modern levels of O_2 are as low as those of the Proterozoic. In scenario 1, the distributions of detectable EECs with detectable O_3 are similar to those of Figure 3.3's top panels (where Proterozoic O_2 is 0.1 PAL) for LUVOIR-A, LUVOIR-B, and HabEx/SS. That is because O_3 is detectable on every target EEC at every distance in the case where Proterozoic O_2 is 0.1 PAL, so assuming that Proterozoic levels are as high as modern levels will produce the same results. For HabEx/no-SS, the mission-level false negative scenario probability decreases from $1.8 - 36\%$ to 1.5%. In scenario 2, the distributions of detectable EECs with detectable O_3 are the same as those in Figure 3.3 in most cases: for Proterozoic O_2 $\geq 10^{-4}$ PAL for

LUVOIR-A, for Proterozoic O_2 $\geq 10^{-3}$ PAL for LUVOIR-B, and for Proterozoic O_2 $\geq 10^{-4}$ PAL for HabEx/SS. That is because, again, for Proterozoic O_2 above those levels, O_3 is detectable on every target EEC at every distance. For lower Proterozoic O_2, there is still no mission-level false negative scenario probability for the 10^{-5} PAL case for LUVOIR-A and for the 10^{-4} PAL case for LUVOIR-B, but it increases to 1.3% for 10^{-5} PAL for LUVOIR-B and to 1.8% for 10^{-5} PAL for HabEx/SS. For HabEx/no-SS, the mission-level false negative scenario probability increases from $1.8 - 36\%$ to $3.3 - 100\%$. Further oxygenation scenarios could be explored in future work.

Whether the origination of life is an extremely rare occurrence or common throughout the universe is a heavily debated topic. The frequency of life originating on habitable planets is highly uncertain (e.g., Sandberg et al., 2018), and the fact that life originated early in Earth's history does not constrain this frequency very much (Spiegel and Turner, 2012; Lacki, 2016). However, the large number of exoplanets that we may be able to soon characterize with future missions offers an opportunity to test whether the origin of life is common. If we observe a number of EECs and detect clearly biogenic O_2 or O_3 on at least one of them, the origination of life on habitable planets must be common. Conversely, if we don't detect O_2 or O_3 with a LUVOIR-A or LUVOIR-B-like instrument, we'll know that EECs are generally unlikely to be Earth-like. This could mean that either the origination of life is very rare, or that life rarely develops oxygenic photosynthesis. In this scenario of null-life detection, we may be able to improve our estimate of the probability of the origination of life using a Bayesian analysis similar to that of Spiegel and Turner (2012) and Kipping (2020). Future work could look at what constraints we can put on the origination of life using a Bayesian analysis for different observation scenarios.

3.5 Conclusions

In this work, we considered whether observations of exoEarth candidates (EECs) with HabEx and LUVOIR may inform us on the fraction of EECs that are Earth-like (f_E) in that they develop Earth-like, O_2-producing life (oxygenic photosynthesis) and become oxygenated roughly following Earth's oxygenation history. To do that, we first considered the probability that HabEx and LUVOIR will detect O_2 and/or O_3 on EECs. Then, we determined whether a null detection, where we do not detect O_2 or O_3 on any EEC, would allow us to constrain f_E. We adopted a statistical approach to this problem. Instead of investigating false negatives on particular planets, we determined whether there might be mission-level false negatives for missions such as LUVOIR and HabEx based on all of the information that we can gain from all of the EECs that these missions can be expected to observe. We considered four different telescope designs: 15 m on-axis segmented-mirror LUVOIR-A, 8 m off-axis segmented-mirror LUVOIR-B, 4 m off-axis monolithic-mirror HabEx with a starshade ("HabEx/SS", where "SS" refers to HabEx's starshade) and 4 m off-axis monolithic-mirror HabEx without a starshade ("HabEx/no-SS"). We also considered three different estimates for $\eta_\oplus$: 24%, following Stark et al. (2019), 5%, following Pascucci et al. (2019), and 0.5%, following Neil and Rogers (2020). In each case, we explore five different levels of Proterozoic O_2 (10^{-1}–10^{-5} PAL), but we note that the lowest end of this range (10^{-5} PAL) is less likely as it is difficult to explain if oxygenic photosynthesis was occurring at modern rates. Therefore these conclusions report our results for Proterozoic O_2 levels between 10^{-1}–10^{-4} PAL. The main conclusions of this chapter are:

1. First, we considered the possibility of not detecting any EECs. The probability of that occurring depends strongly on both $\eta_\oplus$ and the mirror diameter of the instrument. For the cases we considered, these probabilities are:
    - For $\eta_\oplus = 24\%$: 0% for all missions.
    - For $\eta_\oplus = 5\%$: 11% for HabEx, 0% for LUVOIR-A and LUVOIR-B.
    - For $\eta_\oplus = 0.5\%$: 27%, 50%, and 81%, for LUVOIR-A, LUVOIR-B, and HabEx.
2. Second, we considered the possibility of mission-level false negative scenarios where we do not detect O_2 or O_3 on any of the EECs we observe, even if they were all Earth-

like ($f_E = 1$). We find that the main factor determining whether such mission-level false negative scenarios exist is the yield of detectable EECs, which mainly depends on the value of $\eta_\oplus$ and on the instrument's mirror diameter. We found that the level of Proterozoic O_2 we assume does not matter much for these missions, as long as it is above 10^{-4} PAL, as in that case O_3 is detectable on all target EECs with LUVOIR-A, LUVOIR-B, HabEx/SS. The probabilities of a mission-level false negative scenario are as follows:

  - For $\eta_\oplus = 24\%$: 0% for LUVOIR-A and LUVOIR-B; 0.5% for HabEx/SS; 2−36% for HabEx/no-SS.
  - For $\eta_\oplus = 5\%$: 0.1% for LUVOIR-A; 3-4% for LUVOIR-B; 33% for HabEx/SS; 44−81% for HabEx/no-SS.
  - For $\eta_\oplus = 0.5\%$: 52% for LUVOIR-A; 70−72% for LUVOIR-B; 90% for HabEx/SS; 91-98% for HabEx/no-SS.

3. Finally, we considered whether we could constrain the fraction of EECs that are Earth-like (f_E) even if we do not detect O_2 or O_3 on any EEC. The extent to which we may be able to constrain f_E in the case of a null detection depends on the mission and relies primarily on a sufficiently large number of detectable EECs as well as on the ability to detect low levels of O_3.

  - For $\eta_\oplus = 24\%$, a null detection with LUVOIR-A, LUVOIR-B, or HabEx/SS will allow us to constrain the fraction of Earth-like EECs: $f_E \leq 0.094$ with LUVOIR-A , $f_E \leq 0.18$ with LUVOIR-B, and $f_E \leq 0.56$ with HabEx/SS, all with 95% confidence and for Proterozoic O_2 levels $\geq 10^{-4}$ PAL. These constraints also imply that for f_E greater than these upper limits, we have a 95% chance of detecting O_3 on at least 1 EEC, and are therefore likely to do so with LUVOIR-A for $f_E \geq 0.094$, with LUVOIR-B for $f_E \geq 0.18$, and with HabEx for $f_E \geq 0.56$.

- For $\eta_\oplus = 5\%$, a null detection with LUVOIR-A or LUVOIR-B would similarly allow us to constrain $f_E \leq 0.45$ with LUVOIR-A, and $f_E \leq 0.85$ with LUVOIR-B, with 95% confidence and for Proterozoic O_2 levels $\geq 10^{-4}$ PAL. HabEx/SS and HabEx/no-SS on the other hand will not allow us to constrain f_E due to the existence of mission-level false negative scenarios even for $\mathrm{f_E} = 1$. This also means that we may not detect O_3 on any EECs with HabEx/SS and HabEx/no-SS, while we are likely to do so with LUVOIR-A for $f_E \geq 0.45$, and with LUVOIR-B for $f_E \geq 0.85$.
- For $\eta_\oplus = 0.5\%$, none of the missions would allow us to constrain f_E in the event of a null detection, as all have mission-level false negative scenarios with a probability greater than 5%. Therefore, despite the fact that missions with larger aperture mirrors are more robust to uncertainties in $\eta_\oplus$, all missions are vulnerable to inconclusive null detections if $\eta_\oplus$ is as low as 0.5%.

3.6 Appendix

Computing the integration times required for a detection of O_2 or O_3 requires two simulation components: a planetary spectrum model and a noise model. Molecular signatures for each atmospheric species of interest were computed by taking the difference between the continuum (all atmospheric species except the species of interest) and absorbance (all atmospheric species) spectra. The noise and SNR calculations involve the characterization of the different factors impacting the sensitivity. The signal refers to the planetary photons that are successfully counted by the instrument, after considering the telescope, coronagraph/starshade, optics and detector efficiencies. The noise is a combination of effects that includes the Poisson noise introduced by the planetary photons, noise from residual photons from the star, noise from background sources (e.g., exozodi and local zodiacal fluxes), and the intrinsic noise introduced by the detector.

In order to further expand on these components, the appendix is therefore structured as follows: 1) we show geometric albedo spectra used to calculate the SNR of O_2 and O_3 detections with PSG, 2) we present integration times required for a 5-σ detection of O_2 and O_3 at 10, 15, and 20 pc calculated using PSG, 3) we compare our calculated integration times to those calculated using Robinson et al. (2016)'s model, 4) we further detail the assumptions made in simulating observations with LUVOIR and HabEx using PSG.

3.6.1 Geometric Albedo Spectra

As described in Section 4.2.3, we calculate the SNR of O_2 and O_3 detections by first simulating two spectra: one absorbing spectrum with all atmospheric species, and one continuum spectrum with all atmospheric species except the chosen absorber (either O_2 or O_3). In Figure 3.8, we show both spectra for O_3 (left) and O_2 (right) at the six O_2 levels considered in this work.

O_3's strong feature at $\sim$0.25 μm allows for it to be detected even at very low levels. On the other hand, O_2's strongest feature at 0.76 μm becomes difficult to detect at Proterozoic O_2 levels. We note here that we added the collision-induced O_2-O_2 absorption bands in the UV (Wulf bands) between 0.24-0.3 μm as well as the Herzberg O_2 continuum bands (Fally et al., 2000), and the Herzberg O_2 band system (Jenouvrier et al., 1999; Mérienne et al., 2000, 2001), neither of which are included in the HITRAN database.

3.6.2 Integration times at 10, 15, and 20 pc

Here we present the integration times required for a 5-σ detection of O_2 and O_3 at 10, 15, and 20 pc calculated using PSG (Villanueva et al., 2018) in Tables 3.6, 3.7, and 3.8 for LUVOIR-A, LUVOIR-B, HabEx/SS, and HabEx/no-SS (see Section 4.2.3 for details and for calculations at 5 pc).

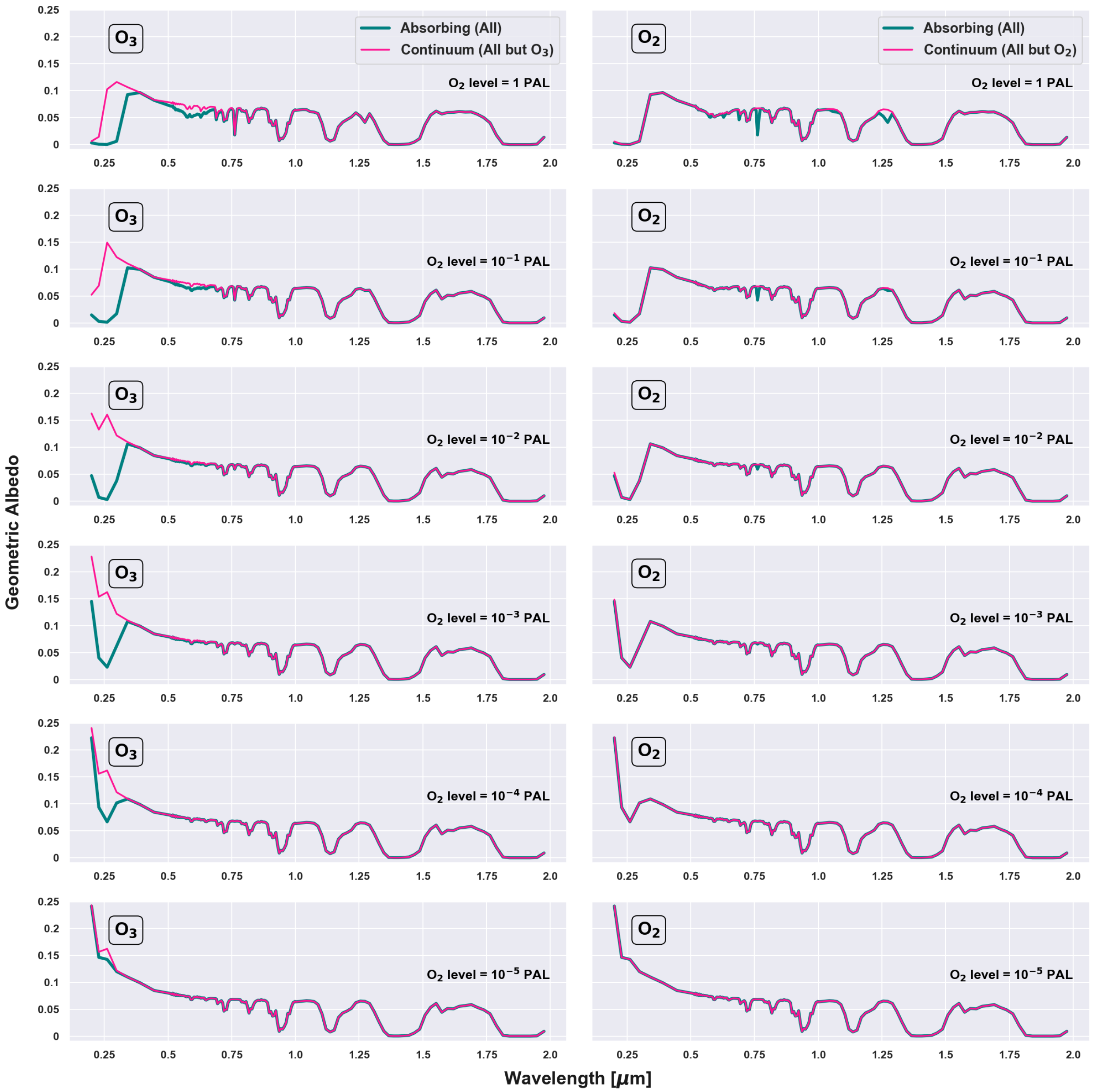

Figure 3.8: **Continuum and absorption spectra for O_3 (left) and O_2 (right) detection for an Earth-like planet orbiting at 1 AU around a Sun-like star at 5 pc with an exposure time of 1000 hours.** We consider six different O_2 levels from 10^{-5} to 1 PAL. Background gases include gases such as N_2, H_2O, CH_4, and CO_2.

Table 3.6: **Integration times [hrs] with LUVOIR-A (15 m), LUVOIR-B (8 m), HabEx/SS (4 m), and HabEx/no-SS (4 m) to yield a 5-σ detection of O_2 and O_3 for an Earth-like planet without clouds at 10 pc for six different O_2 levels.**

O_2 Level	15 m LUVOIR-A	8 m LUVOIR-B	4 m HabEx/SS	4 m HabEx/no-SS
1 PAL	O_2: 5.93 hrs	O_2: 47.7 hrs	O_2: 182.3 hrs	O_2: 1121.5 hrs
	O_3: 1.04 hr	O_3: 4.6 hr	O_3: 3.33 hr	O_3: 332.8 hrs
10^{-1} PAL	O_2: 30.1 hrs	O_2: 241.1 hrs	O_2: 877.8 hrs	O_2: 5376.6 hrs
	O_3: 1.71 hr	O_3: 6.68 hrs	O_3: 2.92 hr	O_3: 1217.6 hrs
10^{-2} PAL	O_2: 288.5 hrs	O_2: 2310.8 hrs	O_2: 7233.8 hrs	O_2: 5.1×10^4 hrs
	O_3: 2.94 hrs	O_3: 10.8 hrs	O_3: 3.12 hr	O_3: 1.1×10^4 hrs
10^{-3} PAL	O_2: 4603.8 hrs	O_2: 3.7×10^4 hrs	O_2: 7.5×10^4 hrs	O_2: 8.1×10^5 hrs
	O_3: 5.24 hrs	O_3: 19.31 hrs	O_3: 4.73 hr	O_3: 2.8×10^4 hrs
10^{-4} PAL	O_2: 2.1×10^5 hrs	O_2: 1.7×10^6 hrs	O_2: 1.4×10^6 hrs	O_2: 3.8×10^7 hrs
	O_3: 23.53 hrs	O_3: 89.33 hrs	O_3: 14.73 hrs	O_3: 1.8×10^6 hrs
10^{-5} PAL	O_2: 1.5×10^8 hrs	O_2: 1.9×10^7 hrs	O_2: 7.9×10^7 hrs	O_2: 3.3×10^9 hrs
	O_3: 740.5 hrs	O_3: 2884.0 hrs	O_3: 387.9 hrs	O_3: 3.8×10^8 hrs

Table 3.7: **Integration times [hrs] with LUVOIR-A (15 m), LUVOIR-B (8 m), HabEx/SS (4 m), and HabEx/no-SS (4 m) to yield a 5-σ detection of O_2 and O_3 for an Earth-like planet without clouds at 15 pc for six different O_2 levels.**

O_2 Level	15 m LUVOIR-A	8 m LUVOIR-B	4 m HabEx/SS	4 m HabEx/no-SS
1 PAL	O_2: 30.56 hrs	O_2: 320.0 hrs	O_2: 951.7 hrs	O_2: 1.6×10^4 hrs
	O_3: 3.34 hr	O_3: 20.7 hr	O_3: 13.2 hr	O_3: 2963.5 hrs
10^{-1} PAL	O_2: 154.8 hrs	O_2: 1614.1 hrs	O_2: 4411.1 hrs	O_2: 8.0×10^4 hrs
	O_3: 5.27 hr	O_3: 28.31 hrs	O_3: 11.27 hr	O_3: 1.1×10^4 hrs
10^{-2} PAL	O_2: 1485.9 hrs	O_2: 1.5×10^4 hrs	O_2: 3.6×10^4 hrs	O_2: 7.6×10^5 hrs
	O_3: 8.93 hrs	O_3: 44.8 hrs	O_3: 11.88 hrs	O_3: 9.5×10^4 hrs
10^{-3} PAL	O_2: 2.4×10^4 hrs	O_2: 2.5×10^5 hrs	O_2: 3.5×10^5 hrs	O_2: 1.2×10^7 hrs
	O_3: 16.2 hrs	O_3: 81.2 hrs	O_3: 17.85 hr	O_3: 2.5×10^5 hrs
10^{-4} PAL	O_2: 1.1×10^6 hrs	O_2: 1.1×10^7 hrs	O_2: 5.8×10^6 hrs	O_2: 5.7×10^8 hrs
	O_3: 77.1 hrs	O_3: 394.7 hrs	O_3: 55.1 hrs	O_3: 1.7×10^7 hrs
10^{-5} PAL	O_2: 9.8×10^7 hrs	O_2: 1.0×10^9 hrs	O_2: 3.3×10^8 hrs	O_2: 5.0×10^{10} hrs
	O_3: 2532.2 hrs	O_3: 1.3×10^4 hrs	O_3: 1442.8 hrs	O_3: 3.4×10^9 hrs

3.6.3 Comparison to Robinson et al. (2016) model

In Figure 3.9 we compare the integration times we calculated using PSG to those calculated using the Robinson et al. (2016) model for an Earth-like planet at 5 pc. In both cases, we calculate the integration times following the method outlined in Section 4.2.3. We note here that Robinson et al. (2016)'s model was updated for these calculations according to the

Table 3.8: **Integration times [hrs] with LUVOIR-A (15 m), LUVOIR-B (8 m), HabEx/SS (4 m), and HabEx/no-SS (4 m) to yield a 5-σ detection of O_2 and O_3 for an Earth-like planet without clouds at 20 pc for six different O_2 levels.**

O_2 Level	15 m LUVOIR-A	8 m LUVOIR-B	4 m HabEx/SS	4 m HabEx/no-SS
1 PAL	O_2: 95.84 hrs	O_2: 1564.0 hrs	O_2: 1.4 $\times 10^4$ hrs	O_2: 1.6 $\times 10^5$ hrs
	O_3: 9.12 hr	O_3: 69.71 hr	O_3: 38.67 hr	O_3: 2.4 $\times 10^4$ hrs
10^{-1} PAL	O_2: 465.8 hrs	O_2: 8033.6 hrs	O_2: 6.4 $\times 10^4$ hrs	O_2: 8.9 $\times 10^5$ hrs
	O_3: 13.2 hr	O_3: 91.1 hrs	O_3: 31.9 hr	O_3: 8.9 $\times 10^4$ hrs
10^{-2} PAL	O_2: 4441.8 hrs	O_2: 7.7 $\times 10^4$ hrs	O_2: 3.4 $\times 10^5$ hrs	O_2: 8.6 $\times 10^6$ hrs
	O_3: 21.6 hrs	O_3: 142.1 hrs	O_3: 33.23 hr	O_3: 7.8 $\times 10^5$ hrs
10^{-3} PAL	O_2: 7.1 $\times 10^4$ hrs	O_2: 1.2 $\times 10^6$ hrs	O_2: 1.7 $\times 10^6$ hrs	O_2: 1.4 $\times 10^8$ hrs
	O_3: 39.4 hrs	O_3: 258.9 hrs	O_3: 49.7 hr	O_3: 2.1 $\times 10^6$ hrs
10^{-4} PAL	O_2: 3.3 $\times 10^6$ hrs	O_2: 5.8 $\times 10^7$ hrs	O_2: 1.9 $\times 10^7$ hrs	O_2: 6.5 $\times 10^9$ hrs
	O_3: 195.4 hrs	O_3: 1292.4 hrs	O_3: 152.3 hrs	O_3: 1.4 $\times 10^8$ hrs
10^{-5} PAL	O_2: 2.9 $\times 10^8$ hrs	O_2: 5.1 $\times 10^9$ hrs	O_2: 1.0 $\times 10^9$ hrs	O_2: 5.7 $\times 10^{11}$ hrs
	O_3: 6625.7 hrs	O_3: 4.4 $\times 10^4$ hrs	O_3: 3983.3 hrs	O_3: 2.9 $\times 10^{10}$ hrs

latest figures reported in the Final Reports (The LUVOIR Team et al., 2019; Gaudi et al., 2020) and we include Earth-like background gases such as O_2, O_3, N_2, H_2O, CO_2, and CH_4 in the atmosphere. Therefore, the Robinson et al. (2016) model calculations may not match those reported in Figure 3.3-7 of the HabEx report (Gaudi et al., 2020).

The integration times calculated using each model agree with each other very closely. This Figure also exhibits the fact that HabEx/SS performs very well in the UV thanks to its starshade and despite its small size. Because of that, it outperforms LUVOIR-A and LUVOIR-B at low O_3 concentrations.

3.6.4 Simulation parameters

The planetary photons being measured by the detector go through a series of optical systems, that each can be assumed to have a specific efficiency or throughput. Background sources also go through the same optical path as the planetary photons. We define the end-to-end throughput for the planetary fluxes as: $T_{total} = T_{Tele} \times T_{coronagraph} \times T_{opt} \times T_{read} \times T_{QE}$, where T_{Tele} accounts for light lost due to contamination and inefficiencies in the main collecting area, $T_{coronagraph}$ is the coronagraphic throughput at this planet-star separation,

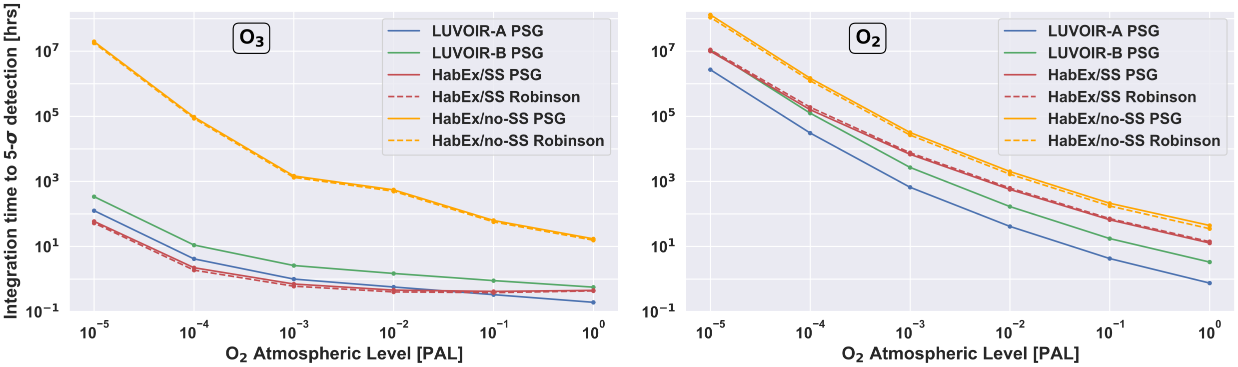

Figure 3.9: **Integration times necessary to detect O_3 (left) and O_2 (right) at 5-σ as a function of O_2 atmospheric level, for an Earth-like planet orbiting at 1 AU around a Sun-like star at 5 pc.** Solid lines: PSG calculations, Dashed lines: Robinson et al. (2016)'s model. Blue: LUVOIR-A, Green: LUVOIR-B, Red: HabEx/SS, Orange: HabEx/no-SS.

T_{opt} is the optical throughput (the transmissivity of all optics), T_{QE} is the raw quantum efficiency (QE) of the detector, and T_{read} is the read-out efficiencies. A summary and representative value for each these parameters can be found in Table 3.1 and we show the coronagraph throughput as a function of separation in Figure 3.10.

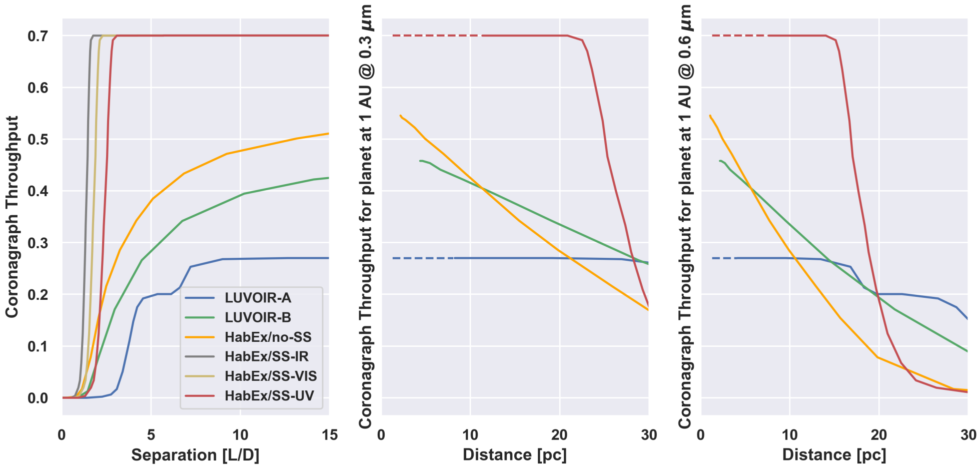

Figure 3.10: **Coronagraph throughput of LUVOIR-A, LUVOIR-B, HabEx/SS, and HabEx/no-SS as a function of separation (left). Coronagraph throughput at 0.3 μm (center) and at 0.6 μm (right) as a function of distance.** Following Stark et al. (2019), LUVOIR-A corresponds to the APLC coronagraph with a segmented on-axis OTA, LUVOIR-B corresponds to the DMVC coronagraph with a segmented on-axis OTA, HabEx/no-SS corresponds to a vortex coronagraph with an off-axis monolithic OTA. The HabEx/SS throughput was taken from Figure 6.4-3 in the HabEx final report and integrates a 70% loss due to PSF losses. The dashed lines correspond to extrapolated coronagraph throughput lines.

For T_{Tele}, we adopt 0.95 for all wavelengths, on par with the particulate coverage fraction for JWST's mirrors. EMCCD detectors are expected to have T_{read} near 0.75 (Stark et al., 2019), while for NIR and other detectors, read-out inefficiencies and bad-pixels may account to a similar value, and we simply adopt T_{read}=0.75 across all detectors as a conservative estimate. The reported quantum efficiency of the different detectors ranges from 0.6 to 0.9 (LUVOIR and HabEx reports (The LUVOIR Team et al., 2019; Gaudi et al., 2020)), yet technological improvements in several of these detectors could be expected in the near future, and we adopt a general T_{QE}=0.9 for all detectors, bands, and for both observatories.

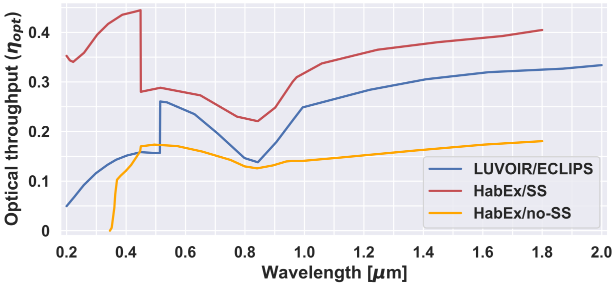

Figure 3.11: **Optical throughput of LUVOIR, HabEx/SS, and HabEx/no-SS as a function of wavelength.** Optical efficiencies for HabEx were taken from the final report (Gaudi et al., 2020), considering the IFS mode for the visible and infrared channels. For LUVOIR, the optical efficiencies were captured from the final report (The LUVOIR Team et al., 2019) and from Figure 4 (IFS mode) of Stark et al. (2019).

Optical efficiencies (T_{opt}) for HabEx were taken from the HabEx report (Gaudi et al., 2020), specifically from Figure 6.4-10 for HabEx/SS and from Figure 6.3-6 for HabEx/no-SS, considering the IFS mode for the visible and infrared channels. For LUVOIR, the optical efficiencies were taken from the final report (The LUVOIR Team et al., 2019) and from Figure 4 (IFS mode) of Stark et al. (2019). These are shown in Figure 3.11.

CHAPTER 4

3D CLOUDS INCREASE OXYGEN AND OZONE DETECTABILITY FOR FUTURE DIRECT IMAGING INSTRUMENTS

This chapter will be submitted for publication as: Checlair, J. H., Chen, H., Villanueva, G. L., Hayworth, B. P. C., & Abbot, D. S. (2021). 3D Clouds Increase Oxygen and Ozone Detectability for Future Direct Imaging Instruments.

4.1 Introduction

In this chapter, we focus on the detectability of the biosignatures Oxygen (O_2) and its photochemical proxy, Ozone (O_3). O_2 has strong absorption lines at UV (<0.2 μm), visible (0.628μm, 0.688μm, 0.762μm), and near-IR (1.269μm) wavelengths (Meadows, 2017; Meadows et al., 2018b). Its photochemical byproduct, O_3, has strong absorption lines in the UV (0.2-0.3μm), visible (0.5-0.7μm), and mid-IR (9.6μm) (ibid).

Previous work probed the capability of LUVOIR and HabEx to detect O_2 and O_3 at different atmospheric concentrations in order to test for whether exoEarth candidates are Earth-like in that they develop Earth-like, O_2-producing life (oxygenic photosynthesis) that oxygenates their atmospheres roughly following Earth's oxygenation history (Checlair et al., 2021). We expand on the past study by exploring the detectability of O_2 and O_3 using a 3D-GCM and including realistic cloud coverage. Expanding to 3-dimensions is important for a number of reasons. First, O_3 is not horizontally homogeneous (e.g., Berggren and Labitzke, 1966), so we must model the photochemistry in 3-dimensions in order to accurately determine the signal from O_3 absorption. This is critical, as previous work determined that O_3 is always easier to detect than O_2 at UV-VIS wavelengths (Checlair et al., 2021). Second, modeling in 3D is required to include the effects of continental, ocean, and sea-ice coverage on the reflectivity and detectability of spectral features (Robinson et al., 2010; Rushby et al., 2019, 2020). Finally, and most importantly, modeling in 3D allows us to include realistic cloud coverage, which has been shown to have an important impact on atmospheric spectra for both transit spectroscopy (e.g., Burrows, 2014; Komacek et al., 2020) and direct imaging (e.g., Fujii et al., 2011; Wang et al., 2018).

This paper is organized as follows. In Section 4.2 we first describe our 3D-GCM simulations. Then, we outline how we simulate observations of those 3D-simulated planets. Finally, we describe our integration time and SNR calculations. In Section 4.3 we present the integration times necessary for LUVOIR and HabEx to detect O_2 and O_3 at 5-σ. We explore the impact of 3D clouds on those estimates, and compare them to previous 1D estimates. In Section 4.4 we discuss some implications and caveats of our work, and we summarize results in Section 4.5.

4.2 Methods

4.2.1 3D Simulations with WACCM

Using the U.S. National Center for Atmospheric Research (NCAR) Whole Atmosphere Community Climate Model (WACCM), we simulate five template exoEarth climates derived from pre-industrial Earths orbiting around the modern Sun. Our numerical setup expands upon one of WACCM's component sets−the F-compset. We use the Community Atmosphere Model v4 (CAM4) (Collins et al., 2006), the Modules for Ozone and Related Chemical Tracers (MOZART) chemical transport model version 3 (Kinnison et al., 2007), but replace the default diagnostic data ocean with a thermodynamic 1.9° × 2.5° slab ocean without internal heat fluxes (q-fluxes). For a more detailed description of the climate model, see Neale et al. (2010) and Marsh et al. (2013).

We probe five different levels of atmospheric O_2: 1, 10^{-1}, 10^{-2}, 10^{-3}, and 10^{-4} Present Atmospheric Level (PAL). This allows us to explore the range of atmospheric O_2 levels believed to have occurred through Earth's Phanerozoic and Proterozoic eras (Pavlov and

Kasting, 2002; Planavsky et al., 2014; Lyons et al., 2014; Reinhard et al., 2017; Olson et al., 2018a; Ozaki et al., 2019). Other gas species included are O_3, H_2O, CH_4, N_2O, CO_2, and N_2. We specify the initial gas concentrations (O_2: $1-10^{-4}$ PAL, CH_4: 0.701 ppmv, N_2O: 0.273 ppmv, CO_2: 288 ppmv) at the start of each simulation and then allow the profiles to freely evolve while conserving mass. N_2 acts as the background gas, and the total pressure is constrained to 1013.25 hPa. The amount of H_2O at any given time is determined by the saturation vapor pressure, whereas the amount of O_3 is determined by photochemical equilibrium established via the Chapman cycle (Chapman, 1930):

$$\begin{aligned} O_2 + hv &\longrightarrow O + O \\ O_2 + O + M &\longrightarrow O_3 + M \\ O_3 + hv &\longrightarrow O_2 + O \\ O_3 + O &\longrightarrow O_2 + O_2 \end{aligned}$$

where M is a third body such as N_2. CH_4 and N_2O have fixed lower boundary mixing ratios. The model simulates cloud ice amount (kg/kg), cloud liquid amount (kg/kg), effective ice particle radius (μm), liquid drop radius (μm), and cloud cover.

We use a horizontal resolution of $1.9^\circ \times 2.5^\circ$, corresponding to 144×96 number of grid cells. The vertical domain has 66 levels and extends from 1013.25 hPa to 5.1×10^{-6} hPa ($\sim$145 km). We set the orbital parameters of all simulated climates (obliquity, eccentricity, and precession) to zero, but keep the planet size, continental configuration, and topography the same as modern Earth. All simulations are integrated for at least 30 Earth years, which is the model time typically needed to achieve top-of-atmosphere radiative balance. All results shown are averaged over the last 10 years.

4.2.2 Simulations of Observations with PSG

We use the Planetary Spectrum Generator (PSG)[1] (Villanueva et al., 2018) to simulate observations with 15 m on-axis segmented-mirror LUVOIR-A, 8 m off-axis segmented-mirror LUVOIR-B, and 4 m off-axis monolithic-mirror HabEx with a starshade. We choose these designs because they bracket the range of reasonably likely space-based direct imaging missions over the next few decades. We start by assuming an exposure time of 1000 hours per planet, and later calculate the integration time required for 5-σ detections of O_2 and O_3 (see Section 4.2.3). Following (Checlair et al., 2021), we choose the instrument parameters based on their reported values in their respective Final Reports (The LUVOIR Team et al., 2019; Gaudi et al., 2020). We summarize these parameters in Table 4.1.

We simulate observations for a planet of 1 $R_\oplus$ and 1 $M_\oplus$ orbiting a Sun-like star at 1AU. We assume an orbital phase of 90° from secondary eclipse, and an orbital plane inclination in the line of sight. The illuminated fraction of the disk is therefore 50%. We set the substellar point at the time of the observation to (0,-150), which corresponds roughly to the center of the Pacific ocean. This will tend to maximize the effect of clouds, since the surface albedo is so low. We assume an orbital distance of 5 pc from the observatory to the planetary system.

We obtain the 3D vertical temperature-pressure and gas mixing ratio atmospheric profiles, as well as the surface data, wind speeds, and cloud profiles from the WACCM GCM output. We include both water ice clouds and water liquid clouds for our base case, and also perform cloud-free simulations to explore the effects of clouds. We include CIA absorption of gases such as O_2-O_2, O_2-N_2, and O_2-CO_2, as well as Rayleigh scattering.

4.2.3 Signal-to-Noise Ratio (SNR) and Integration Time Calculations

We calculate the Signal-to-Noise Ratio (SNR) of O_2 and O_3 following the methodology of Checlair et al. (2021). First, we simulate two spectra using PSG: one absorbing spectrum

---

[1] https://psg.gsfc.nasa.gov

Table 4.1: **Instrument parameters we used in PSG to simulate observations with LUVOIR-A, LUVOIR-B, and HabEx. The throughput values for T$_{coronagraph}$ and T$_{opt}$ are representative average values over the wavelength ranges. Details about all assumed throughputs can be found in Section 3.6.4.**

Parameter	LUVOIR-A	LUVOIR-B	HabEx
Diameter	15 m	8 m	4 m
Wavelength Range	UV: 0.2−0.515μm VIS: 0.515−1.0μm NIR: 1.0−2.0μm	UV: 0.2−0.515μm VIS: 0.515−1.0μm NIR: 1.0−2.0μm	UV: 0.2−0.45μm VIS: 0.45−0.975μm NIR: 0.975−1.8μm
Resolution	UV: 7 VIS: 140 NIR: 70	UV: 7 VIS: 140 NIR: 70	UV: 7 VIS: 140 NIR: 40
Exozodi Level (rel. to Solar Sys.)	4.5	4.5	4.5
Contrast	1×10^{-10}	1×10^{-10}	1×10^{-10}
IWA [λ/D]	4	3.5	39 (UV), 58 (VIS), 104 (NIR) mas
Read noise [e-]	UV: 0 VIS: 0 NIR: 2.5	UV: 0 VIS: 0 NIR: 2.5	UV: 0.008 VIS: 0.008 NIR: 0.32
Dark noise [e-/s]	UV: 3e-5 VIS: 3e-5 NIR: 0.002	UV: 3e-5 VIS: 3e-5 NIR: 0.002	UV: 3e-5 VIS: 3e-5 NIR: 0.005
T$_{coronagraph}$	0.27	0.46	0.7
T$_{opt}$	UV: 0.13 VIS: 0.21 NIR: 0.3	UV: 0.13 VIS: 0.21 NIR: 0.3	UV: 0.38 VIS: 0.27 NIR: 0.36

with all atmospheric species, and one continuum spectrum with all atmospheric species except the chosen absorber (either O_2 or O_3). We then calculate the signal by taking the difference between the two spectra, assuming all species other than the absorber are held fixed. The signal is higher at wavelengths where the absorber gas has stronger absorption features compared to the continuum. We then calculate the SNR by dividing the signal by the noise that PSG simulates for each modeled instrument as a function of wavelength. The total SNR for O_2 or O_3 is then the square root of the sum of the square of the SNRs (Lustig-Yaeger et al., 2019; Checlair et al., 2021):

$$\mathrm{SNR}_{total} = \sqrt{\sum_{\lambda_i} (S_{\lambda_i}/N_{\lambda_i})^2} \tag{4.1}$$

where S_{λ_i} and N_{λ_i} are the signal and the noise for each wavelength. We then calculate the integration time necessary for the total SNR to be equal to 5.0 for a planet at 5 pc:

$$\Delta \mathrm{t} = 1000\ [\mathrm{hrs}] \times \left(\frac{5}{\mathrm{SNR}_{total}}\right)^2 \tag{4.2}$$

4.3 Results

In Figure 4.1, we show horizontally averaged vertical profiles of temperature (A), O_2 (B) and O_3 (C) density, ice cloud (D) and water cloud (E) amount, for five cases of O_2 atmospheric levels: 1, 10^{-1}, 10^{-2}, 10^{-3}, and 10^{-4} PAL. These profiles are calculated by averaging the 3D WACCM output over the illuminated fraction of the globe.

We find that stratospheric O_3 (see panel C) has a strongly nonlinear dependence on low amounts of O_2, making it an easily detectable proxy for even low quantities of O_2. Our averaged O_3 vertical profiles are similar to those photochemically derived by Kasting and Donahue (1980). As we increase O_2 concentration, tropospheric O_3 stops increasing above approximately 10^{-2} PAL of O_2. This is because O_3 is limited by destruction with hydrogen oxides, which are created by tropospheric H_2O photolysis. However, this destruction process

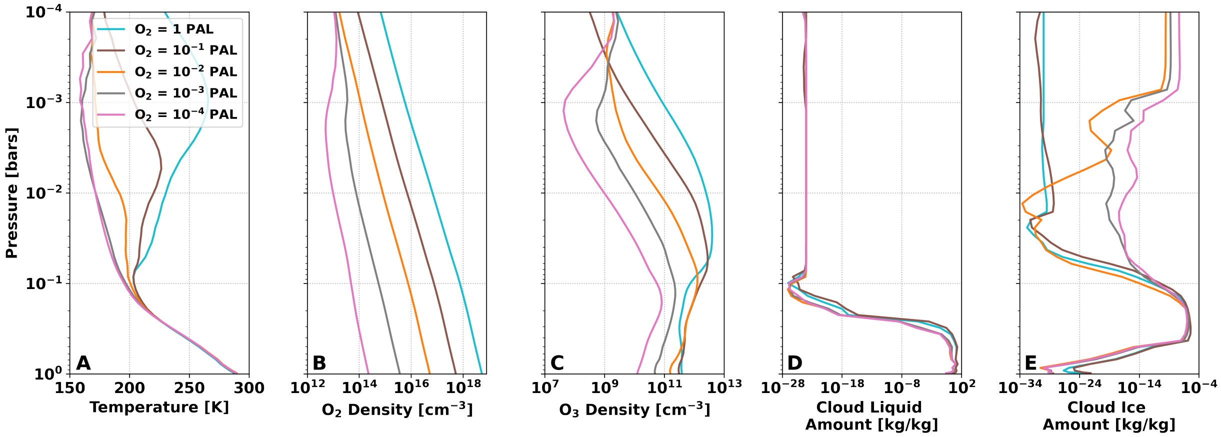

Figure 4.1: **Horizontally averaged vertical profiles of temperature, O_2 and O_3 density, ice and water cloud amount, for five O_2 atmospheric levels.** The 3D WACCM output is averaged over the illuminated fraction of the globe, onto a 1D vertical atmospheric profile. We assume a phase of 90° from secondary eclipse, and an orbital inclination of the orbital plane in the line of sight.

does not impact stratospheric O_3 due to the lack of hydrogen oxides at high altitudes. This is beneficial from an observational perspective, as a lot of the O_3 accumulates above the tropopause cloud deck for both water and ice clouds (see panels D and E). Although clouds do weaken the line depth and density of the gas species by obscuring some of the column mass of O_2 and O_3, clouds also increase the albedo which boosts the signal of gases found above the cloud layer for direct imaging (Wang et al., 2018).

Ozone also creates a temperature inversion in the stratosphere (see panel A) due to its strong absorption features in the UV (Hansen et al., 1997; Pierrehumbert, 2010b). We find that for O_2 levels above 10^{-3} PAL, the temperature inversion is strong enough to limit ice-cloud formation in the stratosphere (see panel E). This may contribute to the heightened detectability of O_2 and O_3 at high concentrations by limiting the density of high-altitude ice clouds.

We show in Figure 4.2 the integration times necessary to achieve a 5-σ detection of O_2 and O_3 with LUVOIR-A, LUVOIR-B, and HabEx, calculated at 5 pc as a function of atmospheric O_2, for two different cases: 3D with clouds (left), 3D cloud-free (center). We

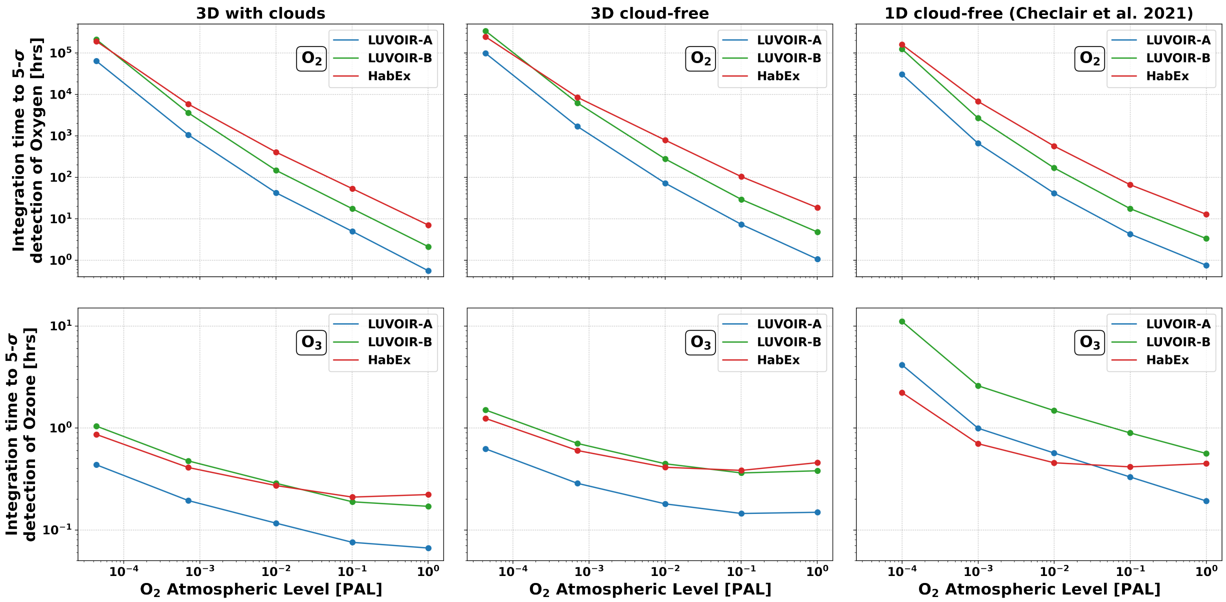

Figure 4.2: **Realistic 3D cloud coverage improved the detectability of O_2 and O_3, thanks to their strong effect on planetary reflectivity and despite the fact that they block some of the column mass of absorbing gas below them from view.** This figure shows integration times required to yield a 5-σ detection of O_2 and O_3 as a function of atmospheric O_2, in 3D with clouds (left), in 3D without clouds (center), and in 1D without clouds based on Checlair et al. (2021) (right). We assume a 1 $R_\oplus$ and 1 $M_\oplus$ planet orbiting a Sun-like star at 1 AU. In all cases, we assume a phase of 90° from secondary eclipse, and an orbital inclination of the orbital plane in the line of sight. Blue: LUVOIR-A; Green: LUVOIR-B; Red: HabEx.

compare these calculations to 1D cloud-free (right) results from Checlair et al. (2021).

For all three missions and at all levels of atmospheric O_2, O_3 is easier to detect than O_2. This is due to O_3's deep and broad feature between 0.2-0.3 μm (Hartley bands) and between 0.5-0.7 μm (Chappuis bands). Thanks to these strong features, O_3 is detectable at 5-σ with all three instruments in under 1.5 hours even at very low O_2 atmospheric levels, for both of our 3D cases. On the other hand, O_2 is more difficult to detect, and the exposure time required to detect it is above 1000 hours in all cases for O_2 atmospheric levels below 10^{-2} PAL.

In general, LUVOIR-A allows for the shortest integration times to detect O_2 and O_3 in all three cases. LUVOIR-B is able to detect O_2 and O_3 more easily than HabEx at high amounts of atmospheric O_2. However, HabEx outperforms LUVOIR-B at low levels of O_2, particularly for O_3 detections. That is because HabEx performs very well in the UV, where O_3 absorbs strongly (with its main absorption band at 0.2-0.3 μm), thanks to its starshade and despite its small size. Interestingly, in most cases all three instruments are able to detect O_3 in a shorter integration time at O_2 levels of 0.1 PAL than for O_2 levels of 1 PAL. This is due to the fact that O_2 also absorbs in the UV. This is not the case for O_2, as O_2 absorbs strongly in the VIS with its strongest band at 0.762 μm, where O_3 does not absorb. This effect is most important for HabEx, which is particularly sensitive in the UV wavelengths.

Comparing the left-most panels (3D with clouds) to the center panels (3D cloud-free) shows that clouds increase the detectability of both O_2 and O_3 at every level of atmospheric O_2, lowering the integration times by a factor of ∼1.3-2.6. This is caused by clouds increasing the albedo and therefore the spectral continuum, allowing for a greater signal. This confirms with previous findings from Wang et al. (2018) who probed the effects of different 1D cloud profiles on the detectability of various atmospheric species, and found that low clouds increase detectability for direct imaging surveys.

We also compare our 3D cloud-free results to the 1D cloud-free integration times calculated by Checlair et al. (2021). We find that our 3D cloud-free calculations yield similar integration times to those calculated in 1D for O_2 detections. However, O_3 integration times calculated in 3D are significantly lower than those calculated in 1D. This is due primarily to two effects. First, the photochemically calculated atmospheric profiles differ from those in Checlair et al. (2021), who fixed the O_2 mixing ratio at all altitudes and let other atmospheric species evolve freely. In this work, we instead set the O_2 mixing ratio at the start of the simulation, and then let all species, including O_2, evolve freely. This leads to a significant difference in the O_3 profiles for low levels of O_2. In Figure 4.3, we show a comparison of the 1D profiles assumed in Checlair et al. (2021) and the horizontally-averaged 3D profiles used in this work, for $O_2 = 10^{-4}$ PAL. Even though the O_2 profiles differ in shape, the O_2 integration times are not significantly different for the two profiles. This is because the increase in O_2 number density at the top of atmosphere is compensated by a decrease at the lower boundary. The difference in O_2 in the upper atmosphere accounts for the drastic change in the O_3 profile, and subsequently, the O_3 integration time. This is because O_3 is highly sensitive to perturbations in stratospheric O_2 (Kasting and Donahue, 1980; Olson et al., 2018a). We also repeated our 3D calculations but with horizontally averaged O_2 and O_3 profiles, and found that the 3D effect was relatively weak, as the integration times calculated in 3D were a factor of ∼2 longer than those calculated in 1D. This further confirms that the main source of the difference in the integration times calculated is a difference in the 1D and 3D photochemical calculations.

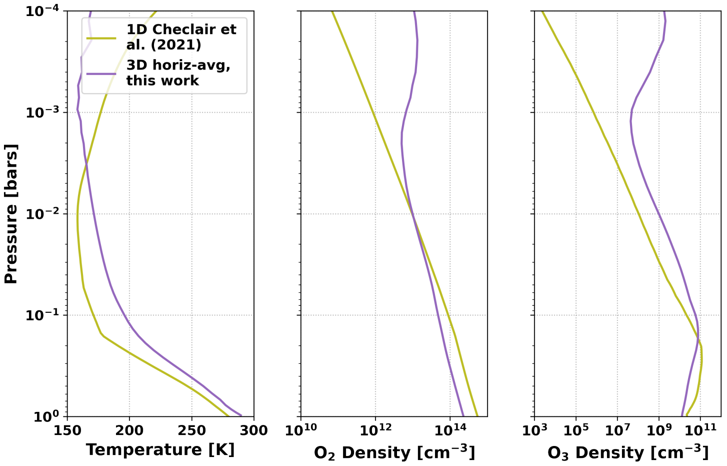

Figure 4.3: **Comparison of 3D horizontally averaged vertical profiles of temperature, O_2, and O_3 density based on WACCM output, with previous 1D profiles from Checlair et al. (2021). The greater O_3 density in the upper atmosphere explains the increase in O_3 detectability when using a 3D model.** The 1D profiles were calculated by fixing O_2 to a given level, and letting other species evolve photochemically, while the 3D profiles were calculated by letting all species, including O_2, evolve freely. The 3D WACCM output is averaged over the illuminated fraction of the globe, onto a 1D vertical atmospheric profile. We assume a phase of 90° from secondary eclipse, and an orbital inclination of the orbital plane in the line of sight.

4.4 Discussion

In this work, we explored the detectability of O_2 and O_3 biosignatures with LUVOIR-A, LUVOIR-B, and HabEx, for various levels of atmospheric O_2. Modeling observations in 3D using WACCM and PSG showed that clouds increase the detectability of both O_2 and O_3 thanks to their strong effect on planetary reflectivity, despite the fact that they block absorbing gas below them from view. Clouds are therefore beneficial to O_2 and O_3 detections for direct imaging surveys, while they are known to hamper transit spectroscopy where albedo is less important. Comparing 3D cloud-free calculations to previous 1D cloud-free calculations (Checlair et al., 2021) showed that the detectability of O_2 was relatively unaffected by 3D modeling. However, O_3 detectability was significantly improved in 3D calculations compared to 1D ones. The difference between 1D and 3D for O_3 was not primarily due to 3D modeling. Instead, it was due to using a different photochemical model in the 3D calculations than the 1D calculations. The photochemical calculations done using WACCM led to a significantly greater O_3 density at pressures below 0.2 bars, and therefore increases detectability.

A caveat of this finding is that clouds may have a reduced effect, and possibly an overall negative effect, on the detectability of spectral features for planets with a high-albedo surface, such as desert planets or bare-granite-rock planets with no land biota. The effect of different surface albedos on the impact of clouds on the detectability of spectral features will be explored in future work.

We focused on the detectability of O_2 and O_3 as biosignatures on terrestrial habitable zone exoplanets. The motivation was that O_2 (and O_3 as its photochemical proxy) may be the most robust biosignature due to its relative lack of geologic sources, long atmospheric lifetime, and strong absorption features at UV and visible wavelengths (Meadows et al., 2018a). Additionally, because LUVOIR and HabEx will be targeting habitable zone planets around G-stars, it is less likely that the O_2 produced will be abiotic in origin than if the planet were orbiting an M-star. This is because G-stars do not experience the intensely luminous pre-main-sequence phase characteristic of low mass stars – which may cause H_2O loss and O_2 buildup early in the planet's evolution (Luger and Barnes, 2015). Also, G-stars have a weaker FUV flux and a stronger MUV-NUV flux than M-stars, which keeps them from rapidly dissociating CO_2 and building up O_2 (Harman et al., 2018). These physical differences between M-star and G-star targets make O_2 false positives less likely for LUVOIR and HabEx targets. However, recent work has isolated 3 other abiotic mechanisms which may lead to detectable quantities of O_2. First, Wordsworth and Pierrehumbert (2014) showed that an atmosphere with low pressures of non-condensable species, such as N_2 or CO_2, can build up O_2 via H_2O photolysis in the upper stratosphere. This false positive scenario could be ruled out by looking for N_2-N_2 collision-induced absorption, strong CO_2 lines, or pressure broadening of other features (Wordsworth and Pierrehumbert, 2014). More recently, Krissansen-Totton et al. (2021) showed that planets with large volatile inventories (waterworlds) may also build up detectable quantities of O_2 on billion-year timescales. This occurs because waterworlds can suppress volcanism and crustal melt, limiting the supply of fresh material to the surface, and therefore, sinks for O_2 (Kite and Ford, 2018; Krissansen-Totton et al., 2021). We may be able to rule out these scenarios by photometric mapping of the surface of the planet with a large aperture telescope to look for continent-ocean dichotomy (Cowan et al., 2009; Fujii et al., 2010). Alternatively, planets with low-volatile inventories (desert worlds) may also build up detectable quantities of O_2 abiotically (Krissansen-Totton et al., 2021). This mechanism could potentially be ruled out by surface mapping of the planet to determine if the surface has low thermal heat capacity (Cowan et al., 2012). However, additional O_2 false positive mechanisms may have yet to be discovered. Even with the possibility of O_2 false positives, O_2 still remains a promising starting point for finding life. By focusing on G-stars, we could rule out some of the false positive scenarios identified above, and with follow-up observations, we can rule out additional false positive scenarios while also looking for secondary biosignatures (other than O_2 and O_3). More work is needed to find additional O_2 false positive cases and to find secondary detections that may aid in ruling them out.

One of the reasons to model the detectability of O_2 and O_3 in 3D is to explore the effects of realistic cloud coverage on direct imaging observations. However, cloud microphysics is a major point of uncertainty when modeling atmospheres, and every GCM has its own parameterization of cloud physics such as cloud-condensation nuclei concentrations, particulate sizes, cloud radiative effects, etc. (Yang et al., 2019b). This means that our integration time calculations are specific to the cloud parameterizations used by WACCM, and other 3D models are expected to yield slightly different results. Despite this, we expect that our result that clouds boost the detectability of O_2 and O_3 by increasing the planetary albedo is robust to assumptions in cloud parameterization, although we leave a detailed investigation of this issue for future work.

The phase and inclination of the planetary orbit provide the planet's illumination geometry, and can therefore enable constraints on different regions of the planetary atmosphere and surface properties. The total number of reflected photons, and therefore the detectability of atmospheric features, depends on the fraction of the illuminated planetary disk and on its surface and atmospheric properties. In this work, we set the phase to 90° and assumed the orbital plane to be in the observation line of sight. The fraction of illuminated disk was therefore assumed to be 50%. We also assumed Earth's continental configuration and fixed the substellar point at the time of observation to center of the Pacific ocean. Different substellar points and surface configurations may affect the planetary albedo and therefore the reflectivity of the illuminated disk. This is particularly true on planets with low cloud coverage, as clouds will lead to a higher top-of-atmosphere albedo even on darker surfaces. Specular reflection of sunlight off oceans (ocean glint) (Robinson et al., 2010) has also been proposed as a way to detect the existence of oceans on an exoplanet. Ocean glint is expected to increase the reflectivity of the planetary surface when near crescent phase, and would therefore affect the number of reflected photons and the detectability of O_2 and O_3 features. Future work will include a full parameter sweep of varying orbital phase, inclination, and substellar point.

The HabEx and LUVOIR missions are still concepts in development, and their specifications have not yet been finalized. We expect these specifications to evolve as the instruments and science goals are further developed. The calculated integration times presented in this work are based on the most recent estimates of instrument parameters for the three mission designs, and may therefore vary if those estimates are updated.

We expect future characterization of terrestrial planets to show that their atmospheres are diverse in their composition, even if they are inhabited by Earth-like life. For lack of a better prior, we considered an Earth-like background atmosphere in our simulations of O_2 and O_3 detections, composed of CO_2, H_2O, N_2, and CH_4. The integration times calculated in this work may be affected by the presence of other background gases that could absorb at wavelengths similar to O_2 and O_3. Future detections of O_2 and O_3 would need to be carried out in the context of a full atmospheric retrieval study that would consider these issues (Feng et al., 2018).

We probed atmospheric O_2 levels ranging from 10^{-4} to 1 PAL, and calculated corresponding photochemically-produced O_3 profiles. We chose these upper and lower limits to span the range of reasonable estimates of O_2 levels in the Proterozoic and Phanerozoic Earth eras (2.5-0 Gya), as we do not expect to detect O_2 and O_3 in either the Archean or the Hadean eras. However, the level of O_2 during the Proterozoic is highly uncertain (Reinhard et al., 2017; Olson et al., 2018a), and estimates based on various geochemical records and modeling efforts vary by four orders of magnitude from 10^{-5} to 10^{-1} PAL (Pavlov and Kasting, 2002; Planavsky et al., 2014; Lyons et al., 2014; Olson et al., 2018a). The upper limit of 10^{-1} PAL is derived from the observation that the deep ocean remained anoxic throughout the Proterozoic, and surface environments would therefore have been only mildly oxygenated. The lower limit of 10^{-5} PAL is derived from the end of mass-independent fractionation of S isotopes following the "Great Oxidation Event." The low end of that range is difficult to explain in biogeochemical and photochemical models if oxygenic photosynthesis was occurring at or near modern rates (Ozaki et al., 2019), therefore we chose to constrain it to 10^{-4} PAL.

4.5 Conclusions

In this chapter, we explored the detectability of O_2 and O_3 biosignatures with LUVOIR-A, LUVOIR-B, and HabEx, for various levels of atmospheric O_2. We used a 3D Global Climate Model, WACCM, to simulate planets of different atmospheric O_2 levels and included photochemical calculations of atmospheric composition. We then used the Planetary Spectrum Generator, PSG, to simulate observations with LUVOIR and HabEx and calculate the integration time required to detect O_2 and O_3 at 5-σ. The main conclusion of this chapter is that clouds increase the detectability of both O_2 and O_3, despite obstructing some of the gas column mass. This is a result of their strong effect on planetary reflectivity for planets with a low-to-intermediate surface albedo, which raises the spectrum continuum and therefore increases the absorbing feature's signal.

Part II

The Snowball Bifurcation on Habitable Tidally Locked Planets

CHAPTER 5

NO SNOWBALL ON HABITABLE TIDALLY LOCKED PLANETS

This chapter was originally published as: Checlair, J., Menou, K., & Abbot, D. S. (2017). No snowball on habitable tidally locked planets. *The Astrophysical Journal, 845*(2), 132.

5.1 Introduction

We note here that in Part II of this dissertation, we will refer to “Earth-like” planets in a different way than in Part I. Here, we define Earth-like to mean a rapidly rotating Earth-sized terrestrial planet in the habitable zone with a functioning silicate-weathering feedback.

As discussed in Chapter 1, terrestrial planets in the habitable zones of three M-dwarfs within 40 light years of Earth have recently been discovered (TRAPPIST-1e, Proxima Centauri b, and LHS 1140b, Anglada-Escudé et al., 2016; Gillon et al., 2017; Dittmann et al., 2017). These planets are expected to be tidally locked to their star, so there has been a large amount of work on whether tidally locked planets in the habitable zone of M-dwarf stars could host life (e.g., Joshi et al., 1997; Segura et al., 2005; Merlis and Schneider, 2010; Kite et al., 2011; Wordsworth et al., 2011; Pierrehumbert, 2011; Yang et al., 2013; Leconte et al., 2013; Menou, 2013; Hu and Yang, 2014; Yang et al., 2014; Hu and Yang, 2014; Kopparapu et al., 2016b; Turbet et al., 2016; Ribas et al., 2016; Barnes et al., 2016; Meadows et al., 2018a; Wolf, 2017; Bolmont et al., 2017).

Snowball events, as described in Chapter 1, could influence habitability through increasing the complexity of life through evolutionary pressure (Kirschvink, 1992; Hoffman et al., 1998) and through increasing the atmospheric oxygen concentration (Hoffman and Schrag, 2002; Laakso and Schrag, 2014, 2017b). Moreover, planets in the habitable zone with low levels of CO_2 outgassing may experience limit cycles between habitable and Snowball climate states (Kadoya and Tajika, 2014; Menou, 2015; Haqq-Misra et al., 2016; Batalha et al., 2016; Abbot, 2016; Paradise and Menou, 2017). It is therefore important to understand the transitions into and out of Snowball events for tidally locked planets.

When considering whether extrasolar planets orbiting stars different from the Sun might exhibit a Snowball bifurcation, one important factor is that ice and snow absorb much better in the near infrared than in the visible (Joshi and Haberle, 2012a; Shields et al., 2013). This means that the difference in albedo between ice and water will be smaller for an M-dwarf spectrum than for the Sun, which would decrease the range of insolation bistability associated with the Snowball bifurcation (Shields et al., 2014). Another important aspect of temperate planets orbiting M-dwarf stars is that they are likely to be tidally influenced, and even tidally locked in 1:1 spin-orbit states (Kasting et al., 1993b). Lucarini et al. (2013) performed simulations using PlaSim, an intermediate-complexity global climate model (GCM), for various planetary rotation rates, and found no Snowball bifurcation as they varied the stellar flux for a tidally locked planet. However, they did not decrease the stellar flux enough to cause global glaciation (Boschi, R., personal communication, March 31, 2017), so we cannot rule out a Snowball bifurcation based on these simulations. Hu and Yang (2014) performed simulations where they varied the stellar flux received by a tidally locked planet orbiting an M-dwarf in an atmospheric GCM (CAM3) coupled to either a mixed layer ocean or a dynamical ocean. They found a smooth transition from a partially to completely ice covered planet in both cases. This suggests the lack of a Snowball bifurcation for tidally locked planets, although they did not show whether there was hysteresis in that paper.

In this chapter we show that tidally locked planets are not required to have a Snowball bifurcation, and in fact are unlikely to have one for realistic parameter assumptions. We show that a primary cause of this behavior is the steady increase in insolation as the substellar point is approached, which contrasts with the Earth-like case where the derivative of insolation with respect to latitude goes to zero as the equator is approached. An additional important factor is that the top-of-atmosphere ice/ocean albedo contrast is small for tidally locked planets because of strong cloud cover over open ocean on the day side. That said, it is possible for tidally locked planets to have a Snowball bifurcation if they have very strong heat transport away from the substellar point or weaker day-side clouds. These conclusions are based on simulations using both an energy balance model (EBM, section 5.2) and PlaSim, an intermediate-complexity global climate model (GCM, section 5.3). We also discuss avenues for further pursuing work in this area in section 5.4 and conclude in section 5.5.

5.2 Energy Balance Model

5.2.1 Earth-like Planet

Here we will solve the Budyko-Sellers energy balance model (Budyko, 1969; Sellers, 1969) for an Earth-like, rapidly rotating planet. For more information see Abbot et al. (2011b) and Roe and Baker (2010). This type of modeling is useful because it allows analytical solutions with clear interpretations. An EBM, however, should only be used to gain qualitative understanding of the climate system, rather than to make quantitative predictions.

Due to rapid rotation and a strong Coriolis force, we will assume that the planet is zonally (East-West) symmetric, as Earth approximately is. We will also assume that the planet is symmetric to reflection across the equator, so we only need to solve for one hemisphere. At steady-state, energy balance is given by

$$\frac{Q}{4}S(x)(1-\alpha(T(x))) = A + BT(x) + C(T(x) - \overline{T}), \tag{5.1}$$

where Q is the solar constant, $S(x)$ describes the meridional distribution of incoming solar radiation, T is the surface temperature, $A + BT$ is a linearization of the outgoing longwave radiation flux as a function of surface temperature, $C(T(x) - \bar{T})$ is a simple parameterization of the meridional redistribution of heat by the atmosphere and ocean, C is a constant with the same units as B, $x = \sin\theta$ is the sine of the latitude with $x \in [0, 1]$. $\alpha(T(x))$ is the albedo, with the form

$$\alpha(T(x)) = \begin{cases} \alpha_1 & T > T_s \\ \alpha_s & T = T_s \\ \alpha_2 & T < T_s \end{cases}, \tag{5.2}$$

where α_1 is a low albedo representing open ocean regions, α_2 is a high albedo representing ice-covered regions, $\alpha_s = \frac{1}{2}(\alpha_1 + \alpha_2)$, and T_s is the annual-mean surface temperature at which ice forms. We will use the insolation from North (1975), which we plot in Figure 5.1. The values assumed for the parameters are chosen for illustrative purposes.

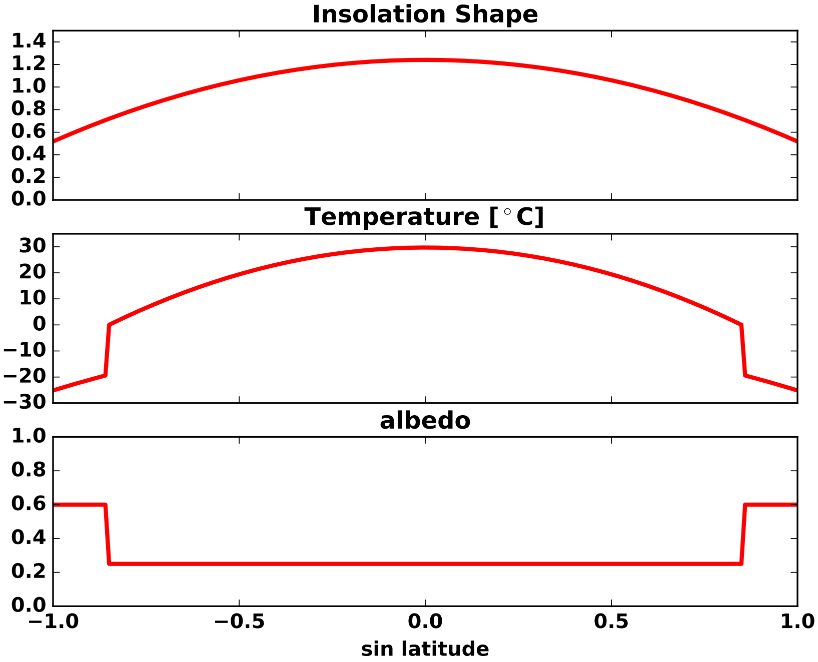

Figure 5.1: **Insolation, temperature, and albedo for the Budyko-Sellers energy balance model in Earth-like configuration.** A latitude of θ=0° (x=sin θ=0) corresponds to the Equator and a latitude of θ=90° (x=sin θ=1) corresponds to the pole. Here a solar constant of Q=1365 W m^{-2} and the following other parameters are used: α_1=0.25, α_2=0.6, A=225 W m^{-2}, B=1.5 W m^{-2} K^{-1}, C=3.0 W m^{-2} K^{-1}, and T_s=-10°C.

We can solve the model to find the following relation for Q as a function of x_s, the sine of the ice latitude,

$$Q = 4\frac{A\left(1+\frac{C}{B}\right)+(B+C)T_s}{S(x_s)(1-\alpha_s)+\frac{C}{B}(1-\alpha_p(x_s))}, \tag{5.3}$$

where $\alpha_p(x_s)$, the global mean albedo, is defined by

$$\begin{aligned}\alpha_p(x_s) &= \frac{\int_0^{90}\alpha(\theta)S(\theta)\cos\theta d\theta}{\int_0^{90}\cos\theta d\theta},\\ &= \int_0^1 \alpha(x)S(x)dx, \\ &= \alpha_1\int_0^{x_s} S(x)dx + \alpha_2\int_{x_s}^1 S(x)dx.\end{aligned} \tag{5.4}$$

Eq. (5.3) represents the solution to the model containing both stable and unstable solutions (see Abbot et al. (2011b) and Roe and Baker (2010) for a discussion of how to figure out which is which) and bifurcations when they join together (Figure 5.2). If we pick a particular value of Q, we can also plot the temperature as a function of latitude (Figure 5.1).

The Snowball bifurcation in the Budyko-Sellers model corresponds to the ice latitude, x_s^*, where $\frac{dQ}{dx_s}\big|_{x_s^*}$=0. This condition can be written as

$$\frac{d}{dx_s}\left(S(x_s)(1-\alpha_s)+\frac{C}{B}(1-\alpha_p(x_s))\right)\bigg|_{x_s^*} = 0, \tag{5.5}$$

or simplifying

$$\frac{dS(x_s^*)}{dx_s}\bigg|_{x_s^*}(1-\alpha_s) = \frac{C}{B}(\alpha_1-\alpha_2)S(x_s^*). \tag{5.6}$$

Physically, we can understand the Snowball bifurcation as a competition between solar forcing and heat transport (Roe and Baker, 2010; Rose, 2015). Both the insolation (warming) and the divergence of the heat flux (cooling) increase as the equator is approached. If the ice latitude is such that when it is perturbed toward the equator the increase in absorbed insolation causes more warming than the increase in heat flux divergence causes cooling, then this ice latitude will be stable. If the opposite is true, then the ice latitude cannot be stable and a Snowball bifurcation occurs. In the Earth-like configuration the derivative

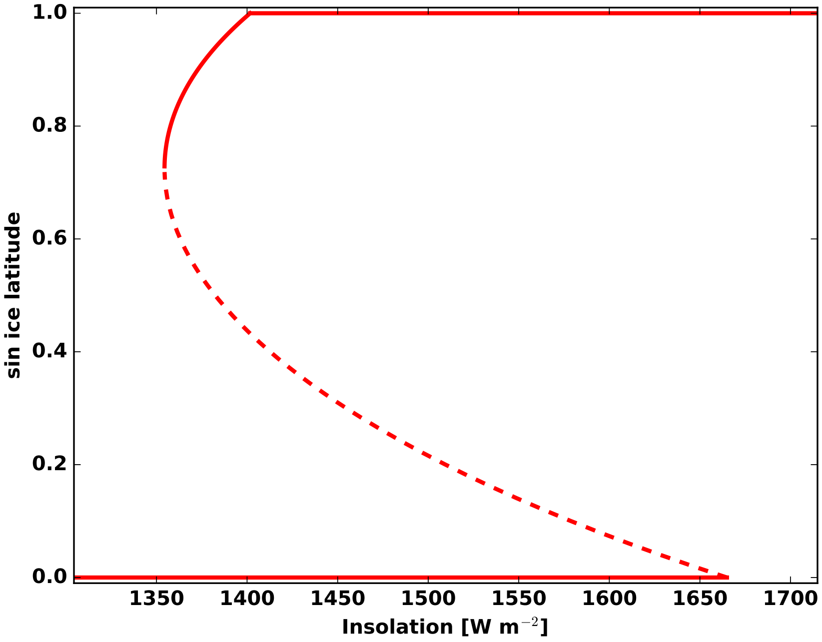

Figure 5.2: **Sine of the ice latitude as a function of solar constant for the Budyko-Sellers energy balance model in Earth-like configuration.** A latitude of θ=0° (x=sin θ=0) corresponds to the Equator and a latitude of θ=90° (x=sin θ=1) corresponds to the pole. A solid line corresponds to stable solutions and a dashed line corresponds to the unstable solution. A bifurcation occurs when stable and unstable solutions join. The following other parameters are used: α_1=0.25, α_2=0.6, A=225 W m^{-2}, B=1.5 W m^{-2} K^{-1}, C=3.0 W m^{-2} K^{-1}, and T_s=-10°C.

of insolation with latitude goes to zero at the equator. As long as $C > 0$ (there is some poleward heat transport) and $\alpha_2 > \alpha_1$ (there is some ice/ocean albedo contrast) this means that there will always be a point where the increase in the divergence of the heat flux exceeds the increase in insolation. A Snowball bifurcation will occur at this point.

5.2.2 Tidally locked planet

We can easily modify the Budyko-Sellers model for the tidally locked configuration. We will use a coordinate system where the tidally locked latitude, θ_{tl}, is the angle from the substellar point. The axis of symmetry here is from the substellar to the antistellar point.

A tidally locked latitude of θ_{tl}=0° corresponds to the substellar point, a latitude of θ_{tl}=90° corresponds to the terminator, and a latitude of θ_{tl}=180° corresponds to the antistellar point (Koll and Abbot, 2015, 2016). The insolation, S_Q, can be written

$$S_Q(\phi_z) = \begin{cases} Q\cos\phi_z & \text{if } \phi_z \leq 90^\circ \\ 0 & \text{if } \phi_z > 90^\circ, \end{cases} \tag{5.7}$$

where ϕ_z is the solar zenith angle. First note that on the day side the solar zenith angle is equal to the tidally locked latitude as we have defined it ($\theta_{tl} = \phi_z$). We can therefore define the insolation shape function for use in Equation 5.1 as

$$S(x) = \begin{cases} 4x & \text{if } x \geq 0, \\ 0 & \text{if } x < 0, \end{cases} \tag{5.8}$$

where we are now using the variable $x = \cos\theta_{tl}$, which is different from the Earth-like case. The tidally locked insolation profile is plotted in Figure 5.3.

We can now apply the Budyko-Sellers model to this insolation profile. We calculate the global mean albedo by integrating over both the day and night sides as follows

$$\begin{aligned} \alpha_p(x_s) &= \frac{\int_0^{180} \alpha(\theta_{tl})S(\theta_{tl})\sin\theta_{tl}d\theta_{tl}}{\int_0^{180}\sin\theta_{tl}d\theta_{tl}}, \\ &= \frac{1}{2}\int_{-1}^{1}\alpha(x)S(x)dx, \\ &= \frac{1}{2}\left(\alpha_2\int_0^{x_s}S(x)dx + \alpha_1\int_{x_s}^{1}S(x)dx\right), \end{aligned} \tag{5.9}$$

Using Equation (5.3), the solution to the tidally locked Budyko-Sellers model is plotted in Figure 5.4. The first thing to note about the tidally locked solution is that for this set of parameters there is no Snowball bifurcation. The reason is that the insolation keeps increasing strongly as the substellar point is approached (x=1). This means the heat export

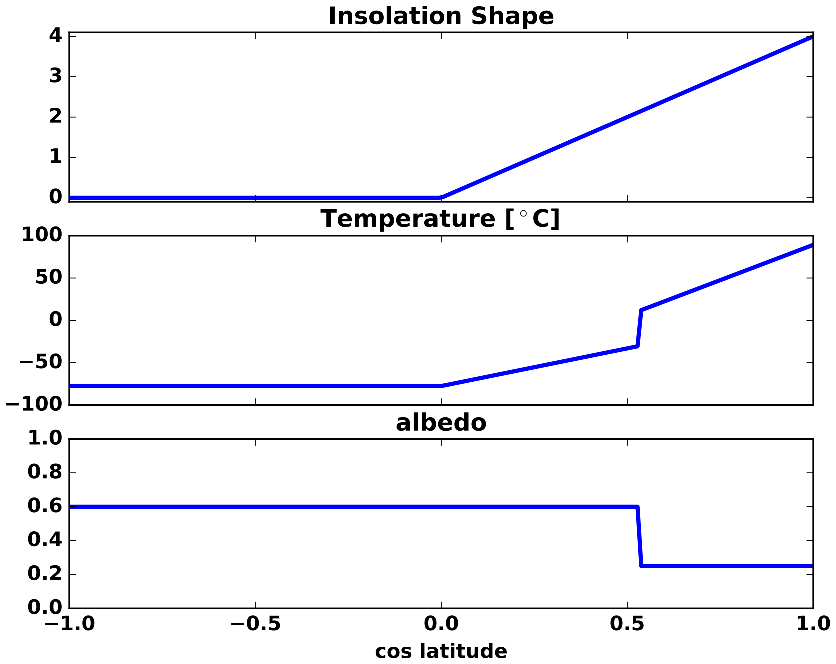

Figure 5.3: **Insolation, temperature, and albedo for the Budyko-Sellers energy balance model in tidally locked configuration.** A latitude of θ_{tl}=0° (x=$\cos\theta_{tl}$=1) corresponds to the substellar point and a latitude of θ_{tl}=180° (x=$\cos\theta_{tl}$=-1) corresponds to the antistellar point in this configuration. Here a solar constant of Q=1100 W m^{-2} and the following other parameters are used: α_1=0.25, α_2=0.6, A=225 W m^{-2}, B=1.5 W m^{-2} K^{-1}, C=3.0 W m^{-2} K^{-1}, and $T_{\rm s}$=-10°C.

has to be very strong for it to overwhelm the warming from increased insolation as the substellar point is approached. If we plug Eq. (5.8) into Eq. (5.6) we find that the ice latitude at which a Snowball bifurcation occurs in the tidally locked model is

$$x_s^* = 2\frac{B}{C}\left(\frac{1-\alpha_s}{\alpha_2-\alpha_1}\right). \tag{5.10}$$

From Eq. (5.10) we can tell that for many parameter choices $x_s^* > 1$, so there is no Snowball bifurcation. This is an important distinction from our condition for the snowball bifurcation in the Earth-like case (Eq. 5.6), which always yields a Snowball bifurcation as long as $C > 0$ and $\alpha_2 > \alpha_1$. We can set $x_s^* = 1$ to solve for the critical value of C, C^*, that allows for a bifurcation

$$C^* = 2B\left(\frac{1-\alpha_s}{\alpha_2-\alpha_1}\right). \tag{5.11}$$

The tidally locked model will exhibit a Snowball bifurcation for $C > C^*$.

Eq. (5.11) has two important implications. First, it shows that if a tidally locked planet is efficient enough at moving heat from warm to cold regions (C is large enough), it is possible for a tidally locked planet to have a Snowball bifurcation. This is important because one might assume that the same planet would have a higher value of C if it were tidally locked because the strong heating and cooling anomalies on the day and night sides should force strong heat transport, and because the planetary rotation rate may be lower. Second, it shows that if the top-of-atmosphere ice/ocean albedo contrast is smaller, a planet is less likely to experience a snowball bifurcation (C^* increases). This is important because tidally locked terrestrial planets should have massive cloud decks on their day sides (Yang et al., 2013; Way et al., 2015; Kopparapu et al., 2016b; Salameh et al., 2017). This should tend to increase the top-of-atmosphere albedo over open ocean regions, making the effective albedo contrast between ocean and ice/snow smaller. Moreover, planets orbiting M-stars should have smaller ice/snow albedos as a result of their stellar spectrum (Joshi and Haberle, 2012a; Shields et al., 2013, 2014).

We can summarize the EBM results in the following way. As long as $C > 0$ (the planet has an atmosphere) and $\alpha_2 > \alpha_1$ (as it should generally be), an Earth-like planet will exhibit a snowball bifurcation. In contrast, the sharp increase in the insolation as the substellar point is approached means that a tidally locked planet will not have a Snowball bifurcation for many parameter choices. Whether a tidally locked planet actually does exhibit a Snowball bifurcation depends on planetary heat transport, ice/snow albedo, and cloud behavior.

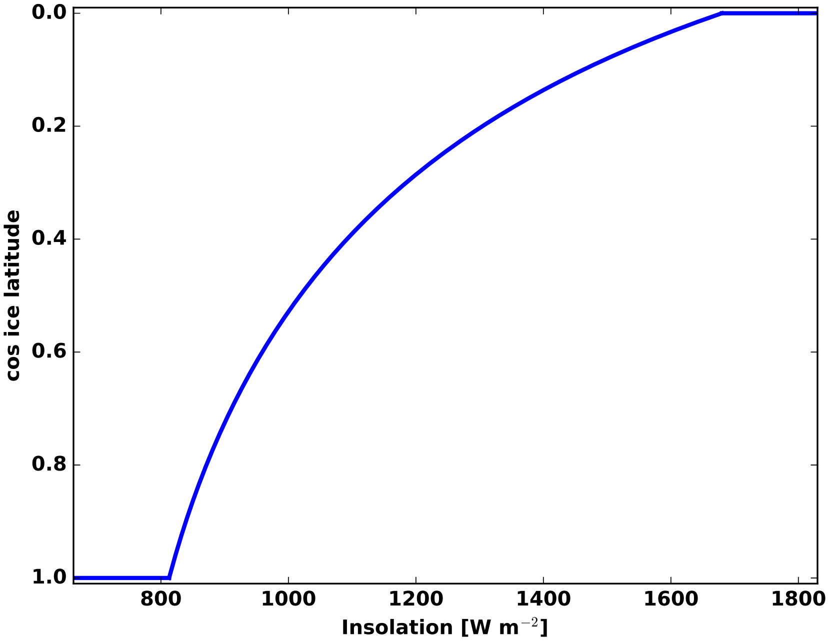

Figure 5.4: **Cosine of the tidally locked ice latitude as a function of solar constant for the Budyko-Sellers energy balance model in tidally locked configuration.** A tidally locked latitude of θ_{tl}=0° (x=$\cos\theta_{tl}$=1) corresponds to the substellar point and a latitude of θ_{tl}=180° (x=$\cos\theta_{tl}$=-1) corresponds to the antistellar point in this configuration. The following other parameters are used: α_1=0.25, α_2=0.6, A=225 W m^{-2}, B=1.5 W m^{-2} K^{-1}, C=3.0 W m^{-2} K^{-1}, and T_{s}=-10°C. There is only a stable solution and there are no bifurcations in this configuration for these parameter choices.

5.3 Planet Simulator

5.3.1 Model

We use PlaSim (Fraedrich et al., 2005), an intermediate-complexity 3D global climate model (GCM), to explore the possibility of bifurcations and bistability for a tidally locked Earth-like planet. PlaSim solves the primitive equations for atmospheric dynamics and has schemes to calculate radiative transfer, convection and clouds, thermodynamic sea ice, and land-atmosphere interactions. One particular aspect of the sea ice scheme that will be relevant in later discussion is that it assumes a gridbox is either completely covered with sea ice or completely ice-free, so that partial sea ice coverage of a grid box is not allowed. We run the model at T21 horizontal resolution (5.625° × 5.625°) with 10 vertical levels. We use modern Earth's continental configuration and set the CO_2 to 360 ppm. We use a 50 m slab ocean with zero imposed ocean heat transport. For the Earth configuration simulations we use modern Earth's orbital configuration and rotation rate. For the tidally locked configuration simulations we set the orbital period (and rotation rate) to 10 Earth days and the eccentricity to zero. We set the obliquity to zero as is appropriate for planets in the habitable zone of M-dwarfs (Heller et al. 2011). We fix the time of day to a constant value in the shortwave radiation scheme. In order to isolate the effects of changes in orbital and rotational configuration, we use the Sun's spectrum for all simulations, including the tidally locked ones. We accidentally used different versions of PlaSim's modern Earth land-sea mask for the Earth and tidally locked configurations. Slight differences in the continental areas can be seen in Figure 5.6. We do not expect these slight differences to affect our conclusions. Given the importance of albedo for this work, we tested PlaSim's top-of-atmosphere albedo in the Earth configuration against modern Earth observations and found a good match (Figure 5.5).

Our methodology for exploring possible bifurcations, bistability, and hysteresis in PlaSim is as follows. For both the tidally locked and Earth configuration we perform a simulation at a high value of stellar flux that leads to a climate with no sea ice and a simulation at a low value of stellar flux that leads to a climate with an ocean that is 100% ice-covered. At various intermediate values of stellar flux we then start simulations from the equilibrated state of either the ice-free climate (henceforth Warm Start) or the ice-covered climate (henceforth Cold Start). We run all simulations until they reach top-of-atmosphere and surface energy balance, for a minimum of 50 years. We then average all displayed variables over the final 5 years of the simulations. If the equilibrated climates that result from Warm Start and Cold Start differ, then there is hysteresis. In the Earth configuration we will find hysteresis that is due to the snowball bifurcation and is associated with bistability. In the tidally locked

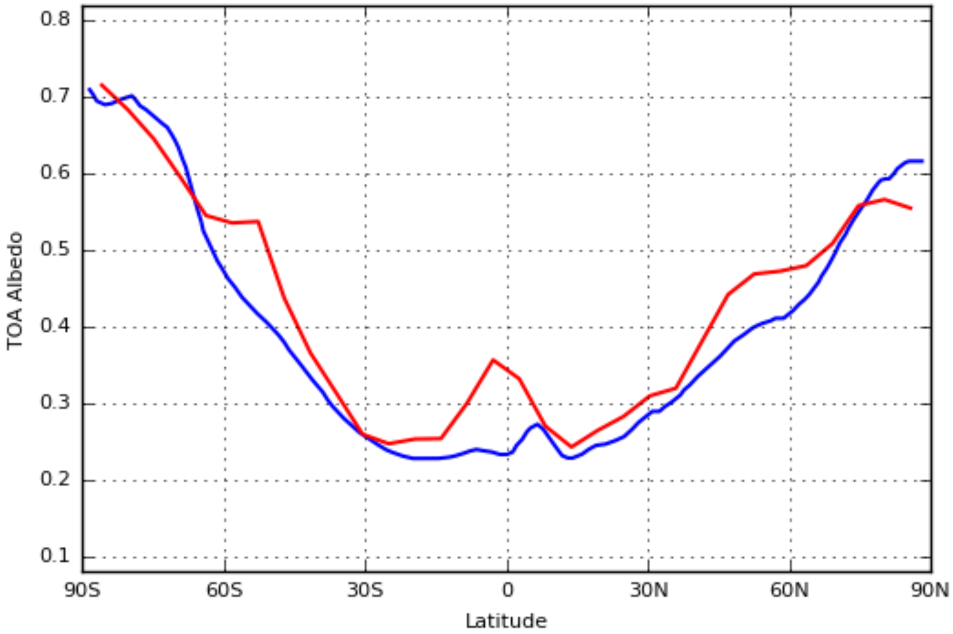

Figure 5.5: **Comparison of the zonal mean top-of-atmosphere albedo from PlaSim in the Earth configuration (red) with observed modern Earth data from Donohoe and Battisti (2011) (blue).**

configuration we will find a small amount of hysteresis that is an artifact of the sea ice scheme and is not related to the snowball bifurcation (Appendix 5.6.1).

5.3.2 Results

Example equilibrated climates

We first present maps of important model output for equilibrated annual mean climates of the tidally locked and Earth configurations (Figure 5.6). We used a stellar flux of 1367 W m^{-2}, roughly modern Earth's value, for the Earth simulation and initialize it from Warm Start conditions. We obtained a climate broadly similar to modern Earth's, which confirms that the low resolution and approximations made by the PlaSim model are acceptable for this study. The features of PlaSim's surface temperature simulation are remarkably similar to modern Earth given that it is an intermediate complexity GCM (Figure 5.6A). Sea ice is

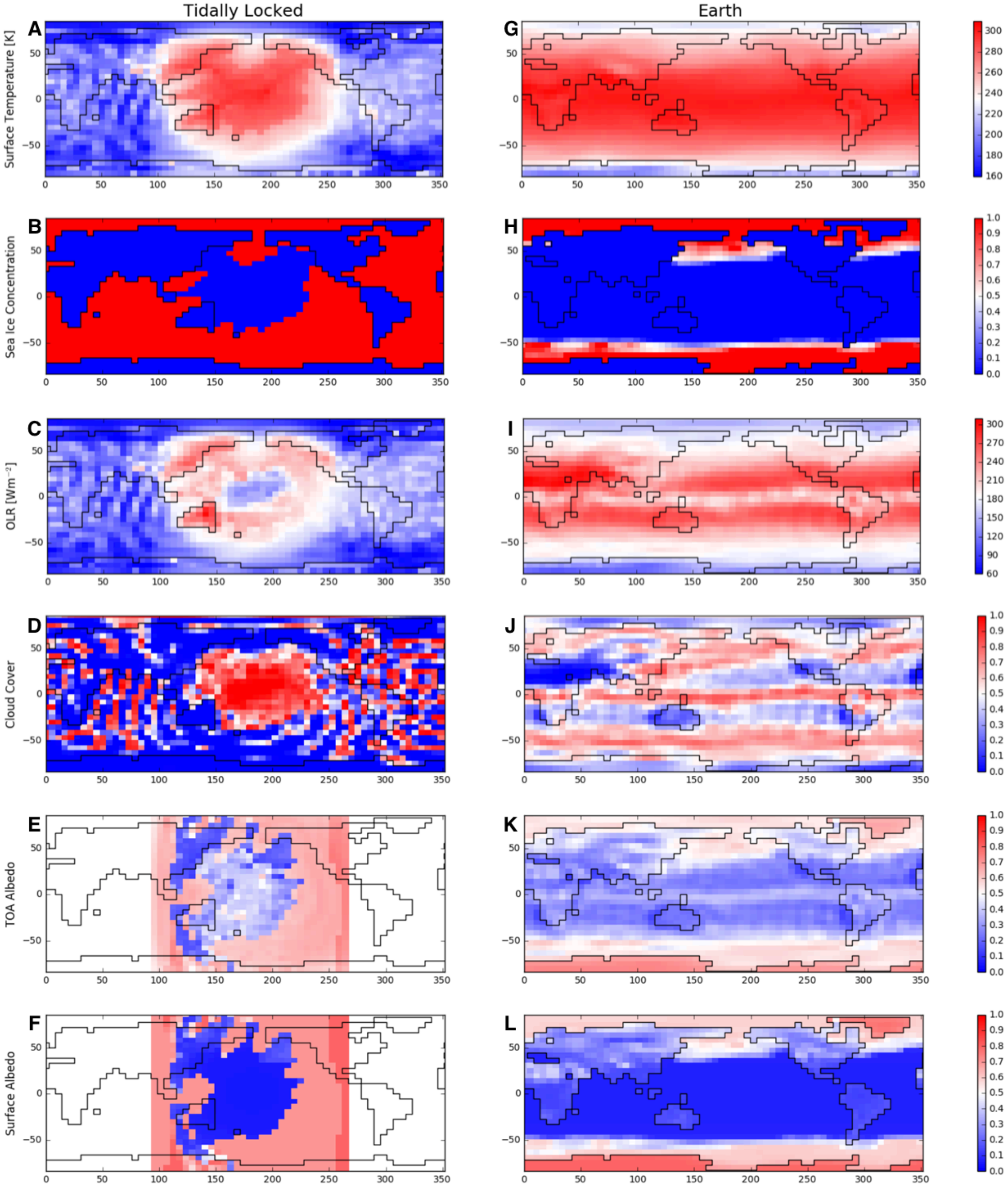

Figure 5.6: **Example states of equilibrated climates for the tidally locked (A-F) and Earth (G-L) configurations.** The mapped variables are surface temperature (A, G), sea ice concentration (B, H), outgoing longwave radiation (OLR) (C, I), cloud cover (D,J), top-of-atmosphere (TOA) albedo (E, K), surface albedo (F, L). The horizontal axis is longitude and the vertical axis is latitude.

slightly more extensive than on modern Earth (Figure 5.6B), which may result from our neglect of ocean heat transport (Winton, 2003; Langen and Alexeev, 2004; Bitz et al., 2005; Rose, 2015). We should also note that partial sea ice coverage is possible in this plot because it is an annual mean. The cloud pattern (Figure 5.6D) shows the Inter-Tropical Convergence zone near the equator and the mid-latitude storm tracks, reflecting a reasonable simulation of atmospheric dynamics and clouds. The other variables are mostly determined by surface temperature, sea ice, and clouds, and they therefore approximate modern Earth well.

For the tidally locked reference simulation, we used a stellar flux of 1100 W m^{-2}. The substellar surface temperature at this stellar flux is similar to the equatorial surface temperature on modern Earth, but the surface temperature is lower in some areas of the night side than at any point on modern Earth (Figure 5.6G). As a result, the ocean is covered in sea ice except for the region near the substellar point (Figure 5.6H). This is sometimes referred to as an "Eyeball" climate (Pierrehumbert, 2011). As expected for a tidally locked planet (Yang et al., 2013; Way et al., 2015; Kopparapu et al., 2016b; Salameh et al., 2017) the open ocean region near the substellar point is mostly covered with clouds (Figure 5.6J). These clouds reflect stellar radiation and raise the top-of-atmosphere albedo (Figure 5.6K), so that the top-of-atmosphere albedo contrast between the sea-ice-free and sea-ice-covered regions is smaller in the tidally locked configuration than in the Earth configuration even though we use the same stellar spectrum for both configurations.

No tidally locked Snowball bifurcation

First we reproduce the well-known result that a Snowball bifurcation exists for modern Earth including bistability and hysteresis (Budyko, 1969; Sellers, 1969; Voigt and Marotzke, 2010; Voigt et al., 2011; Yang et al., 2012a,b). Figures 5.7C and D show the global mean surface temperature and sea ice concentration for the Earth configuration for a range of stellar fluxes starting from both Warm Start and Cold Start conditions. For stellar fluxes between 1274 and 1470 W m^{-2}, PlaSim is bistable, with both a Snowball (ice-covered) state

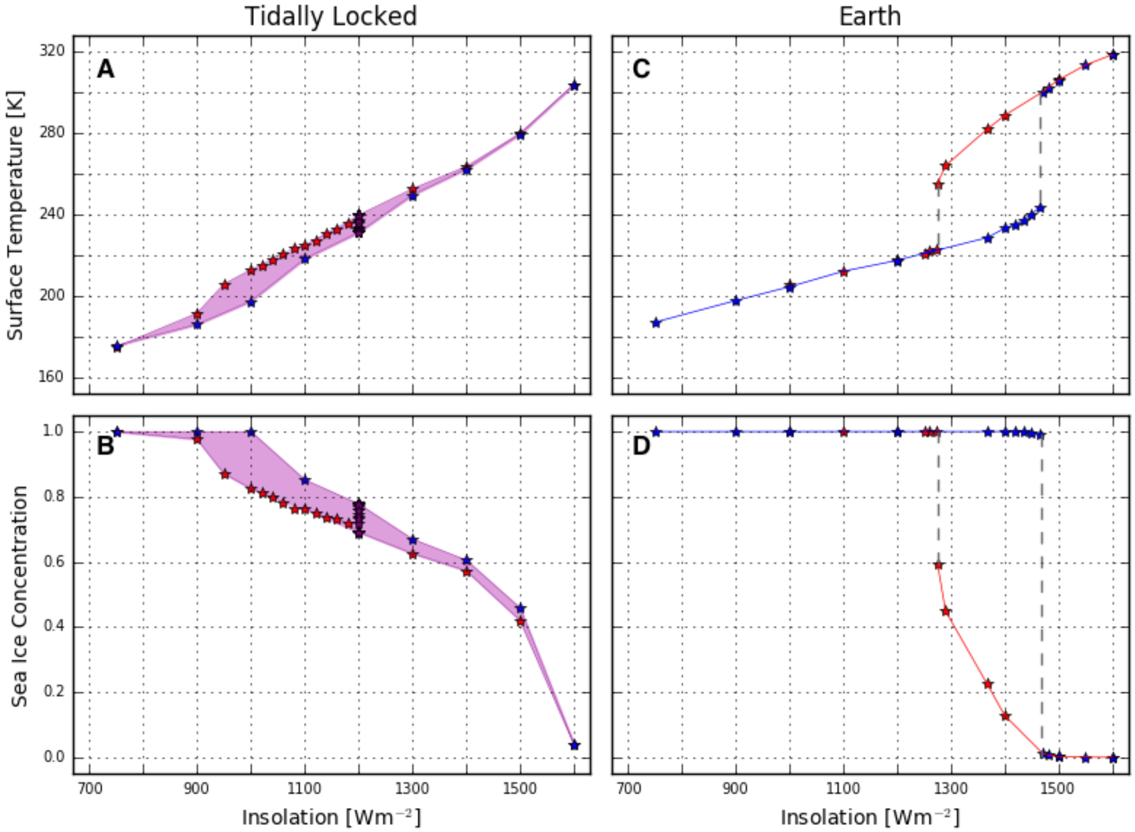

Figure 5.7: **Global mean equilibrated surface temperature (A, C) and sea ice concentration (C, D) as a function of insolation for the tidally locked (A-B) and Earth (C-D) configurations.** Blue stars correspond to a Cold Start (ice-covered planet) initialization and red stars to a Warm Start (ice-free planet) initialization. The purple shaded area corresponds to the continuum of states (A, B). The red line corresponds to the Warm Earth state, the blue line corresponds to the Snowball Earth state, and the grey dashed lines correspond to the unstable states (C,D).

and a Warm state accessible depending on initial conditions. This is similar to the range of bistability observed in the more complex GCM CAM3 with zero ocean heat transport (~1275–1450 Wm^{-2}, Shields et al., 2014; Wolf et al., 2017). The Snowball bifurcation corresponds to the onset of global glaciation in the Warm state, where the Warm state ceases to exist as the stellar flux is decreased.

Next let's consider the tidally locked configuration (Figure 5.7A-B). As the stellar flux is decreased in the Warm state, sea ice and temperature vary smoothly and fairly linearly (especially temperature) toward global glaciation. Similarly, sea ice and temperature vary smoothly out of global glaciation when the stellar flux is increased starting in the snowball state. This suggests that no Snowball bifurcation exists in the tidally locked configuration. A small amount of hysteresis remains between simulations initialized from Warm Start and Cold Start conditions, but this is an artifact of the simple sea ice scheme used in PlaSim (Appendix 5.6.1). We show in Appendix 5.6.1 that the apparently different warm and cold states in the tidally locked configuration are in fact a single continuum of states, as depicted by the shaded purple area in Figure 5.7A-B. The model exhibits no Snowball bifurcation associated with a runaway ice-albedo feedback. We can therefore conclude that while PlaSim shows a clear Snowball bifurcation and jump into globally glaciated conditions in the Earth configuration, it smoothly transitions to global glaciation with no Snowball bifurcation in the tidally locked configuration.

Understanding the GCM results

In section 5.2 we showed that in an EBM a snowball bifurcation is not required in a tidally locked configuration as a result of the insolation pattern. Eq. (5.11) gives the condition for a Snowball bifurcation in tidally locked configuration in the EBM. In the context of understanding the GCM results, the EBM results should be interpreted qualitatively. Specifically, we should expect that a Snowball bifurcation is more likely if the horizontal heat transport is higher or if the top-of-atmosphere ice/ocean albedo contrast is higher.

We infer effective EBM parameters by fitting the parameterizations used in the EBM to the example PlaSim simulations discussed in section 5.3.2. To do this we take the zonal mean of variables in the Earth configuration and the axial mean around the insolation axis in the tidally locked configuration (Koll and Abbot, 2015, 2016). The resulting parameters are displayed in Table 5.1 and the plots from which they are inferred are displayed in Figure 5.8. Figure 5.8 demonstrates that the fits are only approximate, as expected when fitting three-dimensional GCM results to a qualitative one-dimensional EBM. For example, the PlaSim albedo changes smoothly, rather than abruptly as in the EBM, between a high albedo in icy regions and a low albedo ice-free regions as a result of heterogeneities in clouds, land, snow, and the solar zenith angle (Figure 5.8A,B,E,F). The PlaSim outgoing longwave radiation is relatively linear in surface temperature only below 290-300 K (Figure 5.8C,G). Higher temperatures tend to be associated with deep convective clouds that significantly reduce the outgoing longwave radiation. Finally, the linearization of heat transport as a function of the surface temperature appears to be much better in the Earth configuration (Figure 5.8H) than in the tidally locked configuration (Figure 5.8D), where the heat transports are much larger and the night side has a fairly constant heat transport despite some variation in surface temperature.

Despite these limitations, the parameter values we infer for the Earth-like simulation are similar to those we used to obtain an Earth-like EBM simulation, which lends confidence to this methodology. Strikingly, we find that the effective value of C, which represents atmospheric heat transport, is 7.6 times larger in tidally locked than in the Earth configuration (Table 5.1). As a result of the low rotation rate and strongly asymmetric stellar forcing, the tidally locked planet is significantly more efficient at transporting heat from the day to night side than Earth is at transporting heat from the equator to pole. This should tend to promote a snowball bifurcation. There is, however, a much smaller top-of-atmosphere ice/ocean albedo contrast in the tidally locked than the Earth configuration (Table 5.1), despite the fact that we use the Sun's spectrum for both simulations. This results from strong cloud cover over the open ocean region in the tidally locked simulations (Figure 5.6J) and should tend to repress a snowball bifurcation. These two emergent properties of the PlaSim simulation therefore work in opposite directions.

If we simply plug our inferred tidally locked EBM parameters into the condition in Eq. (5.11), we find that it predicts that a Snowball bifurcation should occur for a heat transport parameter above the critical value $C^{*} = 6.3\ W\ m^{-2}\ K^{-1}$. From our tidally locked simulations we infer a heat transport parameter of $C = 13.0\ W\ m^{-2}\ K^{-1}$ (Table 5.1), yet PlaSim does not exhibit a Snowball bifurcation in the tidally locked configuration (section 5.3.2).

This underscores the fact that the EBM results should not be interpreted quantitatively. The EBM does, however, suggest that both the shape of the insolation and the decrease in ocean-ice albedo contrast as a result of cloud cover make a Snowball bifurcation less likely in the tidally locked configuration, whereas the increase in the efficiency of heat transport makes a Snowball bifurcation more likely.

Table 5.1: **A list of the energy balance model parameters inferred from GCM simulations, for both configurations.**

Parameter	Description	Tidally locked	Earth
α_1	lower TOA albedo	0.4	0.3
α_2	upper TOA albedo	0.55	0.55
surface α_1	lower surface albedo	0.1	0.1
surface α_2	upper surface albedo	0.65	0.6
B	OLR parameter	0.9 W m^{-2} K^{-1}	1.4 W m^{-2} K^{-1}
C	heat transport parameter	13.0 W m^{-2} K^{-1}	1.7 W m^{-2} K^{-1}

5.4 Discussion

An important implication of this work is that tidally locked planets in the habitable zone with a functioning silicate-weathering feedback (Walker et al., 1981b) should not be able to exist in a Snowball state for an extended period of time. If such a planet were somehow perturbed into a Snowball state, weathering would shut down and the atmospheric CO_2 would rise (Walker et al., 1981b). With no snowball bifurcation and hysteresis, the planet would quickly warm enough to open up ocean at the substellar point or at continental margins if there were land at the substellar point. Further elaboration on this idea could be made using a coupled climate-weathering model. A Snowball would only be possible for such a planet if it were located in the outer regions of the habitable zone and there was significant CO_2 deposition on the night side. CO_2 deposition has been calculated for Earth-like planets (Turbet et al., 2017), but not yet for tidally locked planets. Coincidentally, this implies that the location of the outer edge of the habitable zone is not well understood for tidally locked planets.

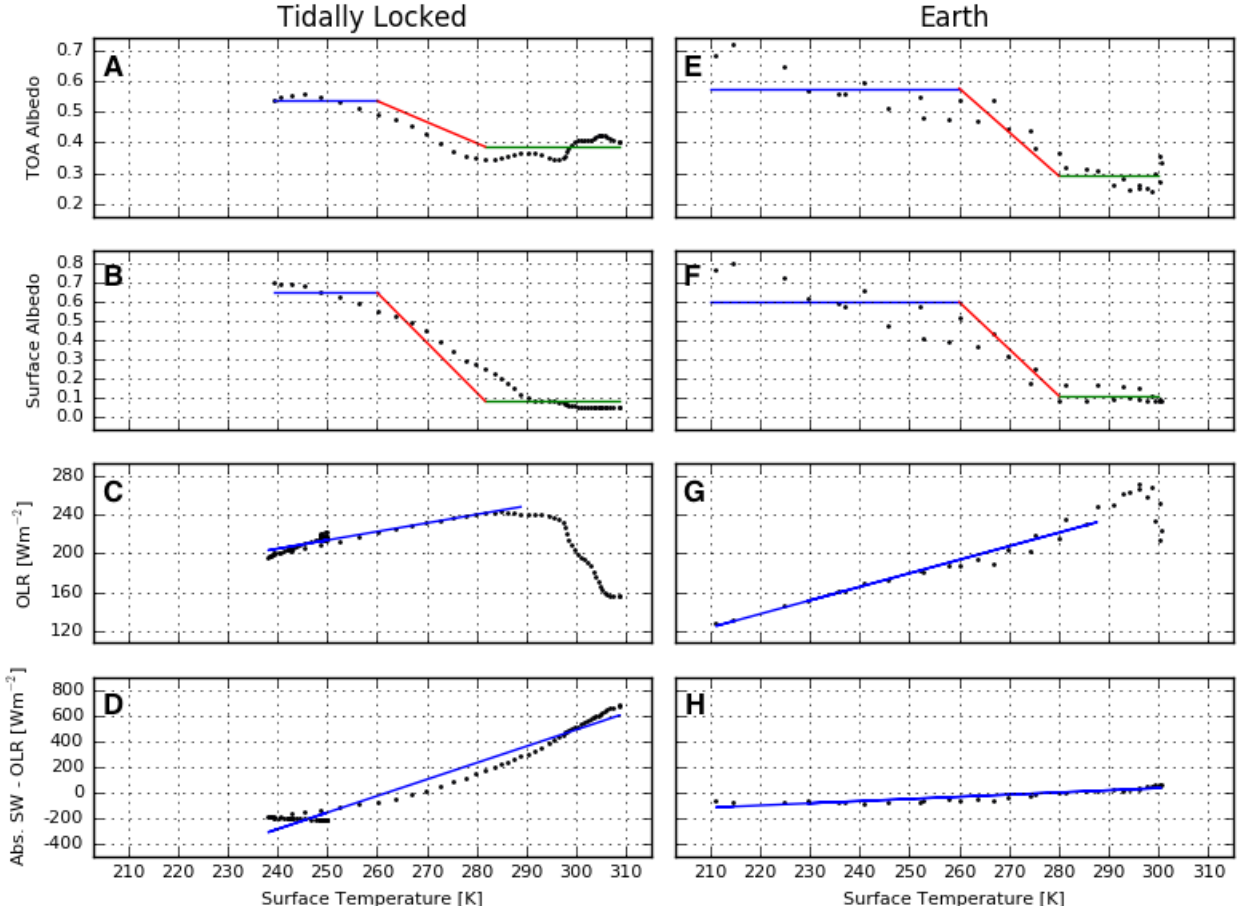

Figure 5.8: **Fits to equilibrated GCM simulations that we used to determine equivalent energy balance model variables for both the tidally locked (A-D) and Earth (E-H) configurations.** The variables considered are top-of-atmosphere (TOA) albedo (A, E), surface albedo (B, F), outgoing longwave radiation (OLR) (C, G), and absorbed shortwave radiation (Abs. SW) minus outgoing longwave radiation (D, H). In panels A-B and E-F the blue lines show the value of inferred ice-covered albedo and the range over which is was calculated and the green lines shown the ice-free albedo and the range over which it was calculated. In panels C-D and G-H the blue lines show the linear fit used to calculate the appropriate EBM variable and the range over which it was calculated. We exclude higher temperatures, where cloud effects become important, from the OLR fit.

We only considered fully evolved tidally locked planets in a 1:1 spin-orbit state in this work. Some M-star planets may be only partially tidally influenced (Leconte et al., 2015), or they could be trapped in higher order spin-eccentricity states (Wang et al., 2014). Considering the Snowball bifurcation in other spin states would be an interesting topic of future research. A study of this issue would require global climate model simulations because many intermediate spin-orbit states lack a clear axis of symmetry to average around when using an EBM.

We found that the value of C, the parameter governing horizontal heat transport in the EBM, helps determine whether a snowball bifurcation occurs for a tidally locked planet. The appropriate value of C, which can be estimated from a GCM simulation, should be inversely proportional to planetary rotation rate (Williams and Kasting, 1997; Vallis and Farneti, 2009; Rose et al., 2017). Moreover, the value of C necessary to cause a bifurcation (Eq. (5.11)) depends on the stellar spectrum because this affects the ice albedo (Joshi and Haberle, 2012a; Shields et al., 2013, 2014). Both the stellar spectrum and the planetary rotation rate for a tidally locked planet receiving a given stellar flux depend on the mass of the M-dwarf. A topic of future work would therefore be to determine whether planets orbiting earlier M-dwarfs are more or less likely to exhibit a Snowball bifurcation than those orbiting later M-dwarfs. In addition, many planetary parameters such as the atmospheric mass and the greenhouse gas complement will affect C (as well as B) and could be explored in GCM simulations.

There has been a fair amount of recent work on the possibility of limit cycles between a Snowball climate state and a Warm climate state for planets in the habitable zone with a CO_2 outgassing rate that is too low to maintain the Warm climate state (Kadoya and Tajika, 2014; Menou, 2015; Haqq-Misra et al., 2016; Batalha et al., 2016; Abbot, 2016; Paradise and Menou, 2017). If tidally locked planets do not exhibit a Snowball bifurcation, then they will not be subject to this type of climate limit cycle. Instead the planet would just comfortably settle into an Eyeball state.

Hu and Yang (2014) found that including a dynamic ocean causes the expansion of sea ice to be more sensitive to changes in the stellar flux. This motivates further research into the effect of ocean circulation on the Snowball bifurcation for tidally locked planets. Since the ocean can transport heat in addition to the atmosphere, and since more heat transport makes a Snowball bifurcation more likely, including a dynamic ocean could potentially make a snowball bifurcation more likely. But because ocean heat transport is a mechanical process and not a simple diffusive one, it may also lead to more complex bifurcation behavior with additional folds and stable states (Rose and Marshall, 2009; Ferreira et al., 2011; Pierrehumbert et al., 2011; Rose, 2015).

The substellar point in our simulations was located over the pacific ocean. We also tried aquaplanet simulations and achieved similar results. It would be interesting to test whether locating the substellar point over a large land mass such as Asia would significantly affects our results.

5.5 Conclusions

The main conclusions of this chapter are:

1. Tidally locked planets will not necessarily exhibit a snowball bifurcation. This is in contrast with planets with Earth-like rotation and orbit, which are required to exhibit a snowball bifurcation except in unrealistic edge cases.
2. The reason tidally locked planets are not required to exhibit a Snowball bifurcation is that the insolation increases strongly as the substellar point is approached.
3. Whether a tidally locked planet actually does exhibit a snowball bifurcation depends on the heat transport and ice/ocean albedo contrast. Higher heat transport and a higher ice/ocean albedo contrast both favor a Snowball bifurcation.
4. We performed global climate model simulations that suggest that realistic tidally locked planets will not exhibit a snowball bifurcation. Although they should tend to have stronger heat transport, the top-of-atmosphere ice/ocean albedo contrast should tend to be smaller.
5. This work suggests that we will not find habitable tidally locked exoplanets with an

active carbon cycle in a Snowball state. This should be verified with a model incorporating an active carbon cycle.

5.6 Appendix

5.6.1 Artifact of Sea Ice Scheme

Interestingly and in contrast with Lucarini et al. (2013), we find a small separation between equilibrated states that were initialized from Warm and Cold Starts. The most likely reason Lucarini et al. (2013) did not observe this separation is that they started their Cold Start simulations from a significantly warmer climate state that was not globally glaciated. To further investigate this issue we show global mean sea ice concentration for a series of simulations with a stellar flux of 1200 W m^{-2} and initial conditions representing equilibrated climate states with different amounts of sea ice (Fig. 5.9). We find that states started within the apparent separation band are stable, rather than approaching separate stable warm and cold states at the upper and lower ends of the separation band. This means that the separation band actually represents a smeared state, which we can consider a continuum of states rather than two distinct "fixed points" with separate basins of attraction. This is clearly unrelated to a Snowball bifurcation and does not alter our interpretation that there is no snowball bifurcation in PlaSim in the tidally locked configuration.

By further investigating the simulations that represent the continuum of states, we determined that the root cause of this behavior is the sea ice scheme, in which each grid cell must either be completely ice-covered or completely ice-free. A grid cell becomes completely ice-covered when the thickness of the sea ice in it exceeds 0.1 m. The continuum of states is possible because within it an additional ocean grid cell can become ice-covered without leading to enough cooling in adjacent grid cells for them to become ice-covered as well. Therefore the climate is stable both with this additional grid box ice-covered and without it ice-covered. We tried to collapse the continuum of states from the PlaSim results into a single state by increasing the horizontal resolution, changing the ice thickness threshold for 100% ice coverage, removing continents, and adding ocean heat diffusion, but the continuum of states remained despite all of these modifications. The issue can therefore only be fully settled by simulations in a GCM that contains a more sophisticated sea ice scheme. Nevertheless we feel that our investigation has shown that the continuum of states in PlaSim in the tidally locked configuration is not related to a Snowball bifurcation.

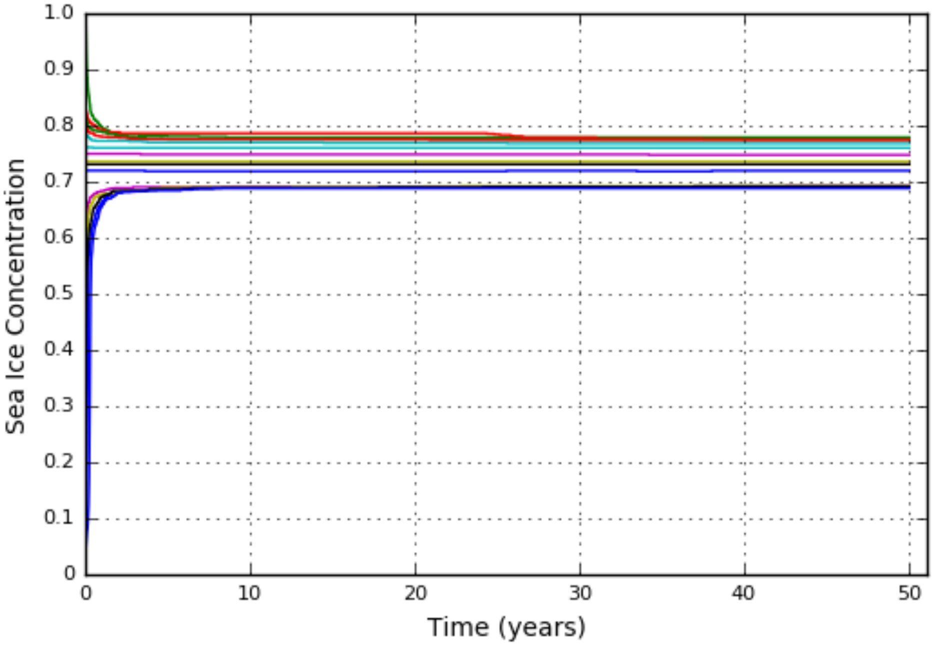

Figure 5.9: **Timeseries of global mean sea ice concentration for a series of simulations at a stellar flux of 1200 W m^{-2} with different initial conditions.** This plot demonstrates that the solution is a continuum of states rather than two distinct fixed points.

CHAPTER 6

NO SNOWBALL ON HABITABLE TIDALLY LOCKED PLANETS WITH A DYNAMIC OCEAN

This chapter was originally published as: Checlair, J. H., Olson, S. L., Jansen, M. F., & Abbot, D. S. (2019). No snowball on habitable tidally locked planets with a dynamic ocean. *The Astrophysical Journal Letters, 884*(2), L46.

6.1 Introduction

Checlair et al. (2017) argued using simple and complex atmospheric models that tidally locked planets are much less likely to exhibit the Snowball bifurcation as a result of the strong increase in stellar irradiation as the substellar point is approached. Moreover, an M-star spectrum reduces the region of climate bistability by lessening the contrast in albedo between ice and ocean, making a Snowball bifurcation less likely (Joshi and Haberle, 2012b; Shields et al., 2013, 2014).

Planetary heat transport, if efficient enough, could destabilize partially glaciated states on a tidally locked planet and reintroduce a Snowball bifurcation as was discussed by Checlair et al. (2017). However, the authors did not explicitly model ocean heat transport, motivating further investigation into its role in possibly retrieving the Snowball bifurcation. Considering dynamic oceanic processes could increase the overall planetary heat transport, potentially making a bifurcation possible. Hu and Yang (2014) previously modeled a tidally locked planet orbiting an M-star using an atmospheric GCM (CAM3) coupled to a dynamic ocean. They did not directly look for bifurcations or hysteresis, but found a smooth transition from a partially glaciated to a fully ice-covered planet, suggesting the potential lack of a bifurcation. In this paper, we investigate the effects of including a dynamic ocean on the Snowball bifurcation for tidally locked planets in a coupled ocean-atmosphere GCM (ROCKE-3D).

6.2 Methods

6.2.1 Model Description

We performed our calculations using ROCKE-3D (Way et al., 2017), a fully coupled ocean-atmosphere general circulation model (GCM) that is derived from NASA Goddard Institute for Space Studies (GISS) ModelE2. ROCKE-3D has previously been used to examine the climate states of slowly rotating and tidally locked exoplanets, including Warm and Snowball climates (Del Genio et al., 2017; Jansen et al., 2019; Way et al., 2018). The reader is referred to Way et al. (2017) and references therein for details regarding ROCKE-3D and its parent model, but we note that ROCKE-3D includes a thermodynamic-advective sea ice model. In contrast with previous studies of Snowball bifurcations on tidally locked planets (Checlair et al., 2017), ROCKE-3D considers ice advection, allows for partial ice coverage within cells, and includes dynamical ocean heat transport. Our present investigation using ROCKE-3D thus represents a significant advance over prior work.

6.2.2 Model Configurations

Our experiments consider an Earth-like planet with regard to mass, radius, surface gravity, and atmospheric mass and composition (although we exclude O_3). Our simulated planet nonetheless differs from the Earth in several ways. We simulate a tidally locked planet in a circular orbit with a 50 day period around an M-star (Kepler 1649, M5V). We chose the stellar spectrum from ROCKE-3D's default spectra. It is based on the BT-Settl spectrum with $T_{eff} = 3200$K, logg = 5, Fe/H = 0 (Allard et al., 2012). The surface of the planet is covered exclusively by ocean. The ocean in our model consists of 5 layers and is considerably shallower than Earth's, reaching a maximum depth of 189 m. In this configuration, running the model on 44 CPU cores requires on average 180 hours of wall time. A deeper ocean would increase the computational cost considerably. Our model configuration is summarized in Table 6.1.

Table 6.1: **Model configuration**

Planetary Parameter	Value
Mass	$M_\oplus$
Radius	$R_\oplus$
Surface pressure	1 bar
Atmospheric composition	Pre-industrial Earth (78% N_2, 21% O_2, 1% Ar, 285 ppm CO_2, variable H_2O)
Continental configuration	Aquaplanet
Ocean depth	189 m (5 layers)
Obliquity	0
Eccentricity	0
Orbital period	50 days
Rotation period	50 days
Stellar spectrum	Kepler 1649 (M5V star)
Stellar irradiation	variable (500 - 1600 Wm^{-2})

6.2.3 Modeled Scenarios

We first performed simulations at stellar irradiations, S, of 1600 Wm^{-2} and 500 Wm^{-2}, yielding an equilibrated ice-free climate state and an equilibrated globally glaciated state, respectively. We then investigated potential climate hysteresis by using the ice-free equilibrated state (S=1600 Wm^{-2}) as the initial condition for our "Warm Start" experiments and the globally glaciated equilibrated state (S=500 Wm^{-2}) as the initial condition for our "Cold Start" experiments. For our Warm Start experiments, we restarted the model from an ice-free initial condition at progressively lower stellar irradiation. For our Cold Start experiments, we restarted the model from a globally-glaciated condition at progressively higher stellar irradiation. The Warm Start and Cold Start scenarios are shown at the upper left and lower right corners of Figures 6.1 and 6.2. For both sets of experiments, we examined the resulting climate state at stellar irradiations of 1500, 1350, 1200, 1050, 900, and 750 Wm^{-2}. We diagnosed steady-state for each model scenario based on a net planetary radiation balance of +/- 0.2 Wm^{-2}. This was typically achieved on a timescale of $\sim$ 500 - 1000 model years.

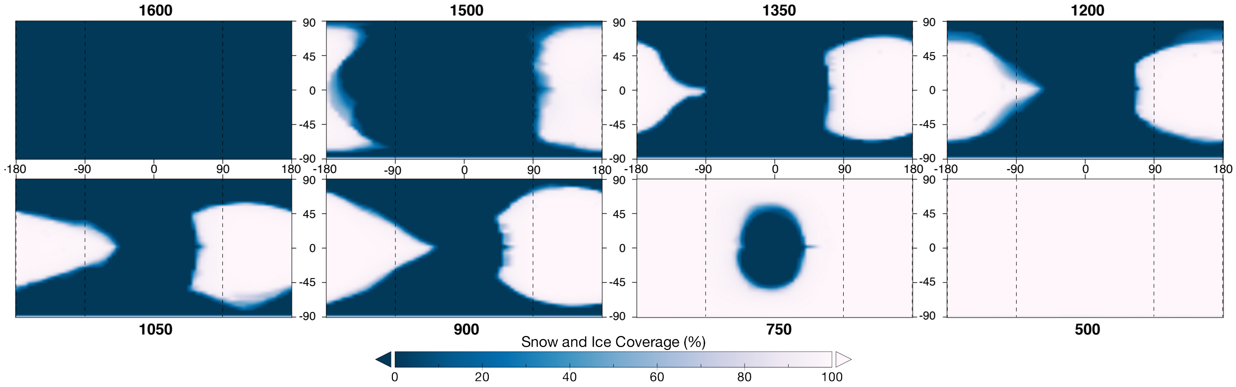

Figure 6.1: **Asymmetric progression of ice coverage on a tidally locked aquaplanet with a dynamic ocean (warm start).** Steady-state snow and ice coverage (% area) for decreasing stellar irradiation, from 1600 Wm^{-2} (upper left) to 500 Wm^{-2} (lower right) as a function of longitude (horizontal axis) and latitude (vertical axis). Although ice coverage monotonically increases with decreasing stellar irradiation, ice does not uniformly advance. Each panel is centered on the substellar point.

6.3 Results

The net effect of a dynamic ocean is to transport heat from the substellar region where energy is gained to the nightside where energy is lost. In addition to this, the ocean transports heat north and south of the substellar point, warming higher latitudes. To illustrate this, we first present maps of sea ice cover (Figure 6.1), surface temperature (Figure 6.2), and ocean surface currents (Figure 6.3) for equilibrated annual-mean climates of the simulated tidally locked aquaplanet. As the stellar irradiation decreases, sea ice begins to form on the antistellar point and gradually progresses towards the substellar point in an asymmetrical manner (Figure 6.1). Similarly, the increase in sea surface temperature is not radially uniform approaching the substellar point (Figure 6.2) as occurs for tidally locked planets without a dynamic ocean ("Eyeball states," Pierrehumbert, 2011; Menou, 2015). There are two areas north and south of the substellar point, and one smaller area eastward of it, that are warmer than the substellar point itself. These patterns are reflected in the sea ice cover patterns (Figure 6.1) and are caused by circulation gyres, which can be seen in maps of upper layer oceanic circulation (Figure 6.3). They were similarly found by Hu and Yang (2014) and Yang et al. (2019a), who attributed them to superrotating equatorial surface winds caused by Rossby and Kelvin atmospheric and oceanic waves that drag sea ice from the night side to the dayside. This limits the overall heat transport to the nightside and shapes the asymmetrical progression of sea ice and sea surface temperature as stellar irradiation is varied.

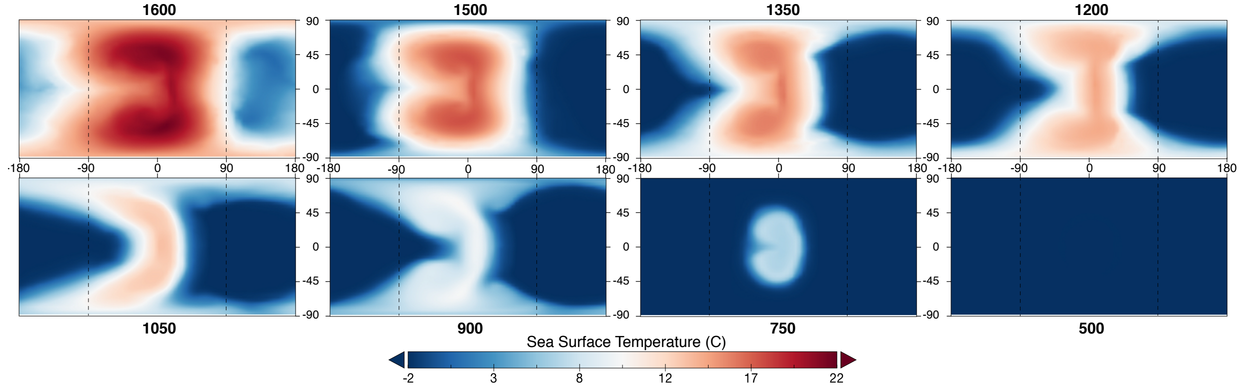

Figure 6.2: **Asymmetric progression of sea surface temperature on a tidally locked aquaplanet with a dynamic ocean (warm start).** Steady-state sea surface temperature (°C) for decreasing stellar irradiation, from 1600 Wm^{-2} (upper left) to 500 Wm^{-2} (lower right) as a function of longitude (horizontal axis) and latitude (vertical axis). Ocean circulation redistributes heat poleward on the day side (Figure 3), promoting equatorial ice advance from the night side. Each panel is centered on the substellar point.

We next explore the possibility of bifurcations and bistability for a tidally locked planet with a dynamic ocean (Figure 6.4). As the stellar flux decreases, the planet's ice cover increases gradually, until reaching a globally ice-covered state between 500 and 750 Wm^{-2}. Similarly, if we increase the stellar flux, the planet gradually deglaciates and reaches an ice-free state between 1500 and 1600 Wm^{-2}. There is no bistability or hysteresis in the climate, as both the Warm Start and Cold Start configurations result in the same equilibrated climate at all stellar fluxes.

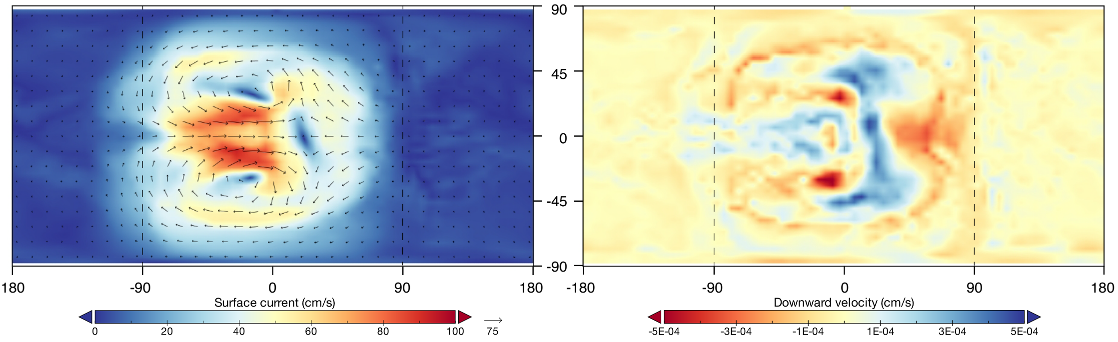

Figure 6.3: **Ocean circulation patterns that drive the asymmetric progression of ice coverage and surface temperature on a tidally locked aquaplanet with a dynamic ocean.** Steady-state surface ocean currents (left) and vertical velocities (right) for the ice-free 1600 Wm^{-2} scenario as a function of longitude (horizontal axis) and latitude (vertical axis). The plots are centered on the substellar point. The development of gyres (i.e. horizontally circulating currents) to the north-west and south-west of the substellar point preferentially warms the poles and limits eastward equatorial heat transport to the night side.

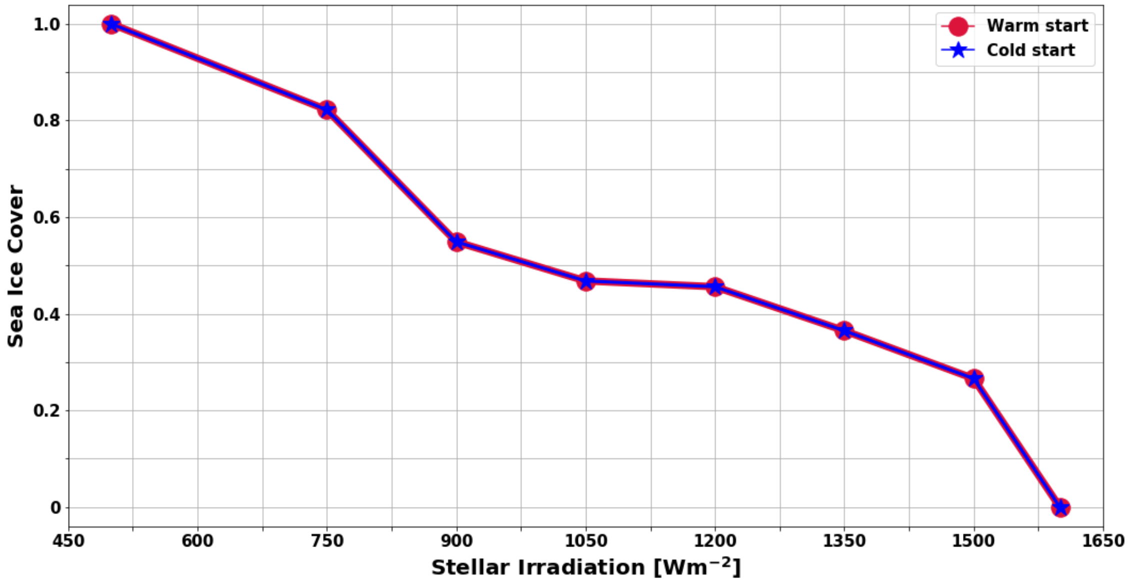

Figure 6.4: **No Snowball bifurcation for the tidally locked planet.** Global-mean equilibrated sea ice cover as a function of stellar irradiation. Blue stars correspond to a Cold Start (ice-covered planet) initialization and red circles to a Warm Start (ice-free planet) initialization. For all values of irradiation the planet equilibrates to the same final state regardless of its initial state.

6.4 Discussion

An important issue in planetary habitability is the possibility for terrestrial planets to go through global glaciations, called Snowball events. Earth itself is believed to have gone through a number of Snowball events in its history (Kirschvink, 1992; Hoffman et al., 1998, 2017). Although extreme glaciation might be expected to challenge life, Snowball events are associated with increases in biological and ecological complexity in Earth's history. The reasons for this relationship are poorly understood, but may arise from accelerated evolution in the wake of environmental perturbation or enhanced nutrient delivery from glacial weathering and resulting increases in environmental oxygen following more than a billion years of apparent biogeochemical stasis (Hoffman et al., 1998; Planavsky et al., 2010; Brocks et al., 2017; Laakso and Schrag, 2017a). Similar events may be required to trigger increasing complexity on other inhabited planets as well.

Snowball events are the result of the existence of the Snowball bifurcation in the climate of rapidly rotating planets like the Earth. Checlair et al. (2017) previously showed using an intermediate-complexity GCM with a slab ocean that tidally locked planets such as those orbiting in the habitable zones of M-stars are unlikely to go through Snowball bifurcations. This is a result of the strong increase in stellar irradiation as the substellar point is approached. However, they found that if planetary heat transport is increased to a critical value, the bifurcation may be recovered. Although this could theoretically reintroduce the Snowball bifurcation, here we found that this does not occur in a complex ocean-atmosphere GCM with a dynamic ocean (ROCKE-3D). Instead, sea ice extent on tidally locked planets gradually increases as irradiation is decreased, with a wide range of states of intermediate glaciation ("Eyeball" states).

The most important consequence of this work is that habitable tidally locked planets should not be found in a Snowball state for an extended period of time. Consider a partially glaciated tidally locked planet with open ocean at the substellar point. If some perturbation such as a volcanic eruption or asteroid impact drove it into a Snowball state, it would quickly return to the original, partially glaciated state. The reason is that tidally locked planets lack Snowball bifurcations and bistability, so the partially glaciated state is the only stable state at the that stellar irradiation.

One caveat of our study is that the ocean depth is only 189 m. Increasing this depth could alter our results by increasing the ocean heat capacity and allowing deep circulation. In Earth's ocean, the heat transport by the wind-driven gyres is concentrated in the upper ocean but can reach to around 500 m depth (e.g., Boccaletti et al., 2005). This suggests that a deeper ocean might lead to somewhat stronger ocean heat transport, possibly amplifying the effect of the gyres on sea ice cover. A much deeper ocean would also raise the possibility of a deep ocean overturning circulation between the day and night sides, which could additionally contribute to heat transport and potentially keep the night side ice-free at lower stellar irradiations. However, the strength of the deep ocean overturning is controlled by small-scale turbulent mixing, which needs to be parameterized in the GCM, and which is very hard to constrain (Wunsch and Ferrari, 2004). Using a similar GCM as presented here, Yang et al. (2019a) found that the climate state of tidally locked aquaplanets is sensitive to ocean depth, although the relationship between ocean depth and global climate is not straightforward. In summary, the sensitivity of planetary climate and of the Snowball bifurcation to ocean depth is complex and represents an intriguing topic for future work.

Land configuration may also affect ocean heat transport and glaciation dynamics. Yang et al. (2019a) found that adding continental barriers reduces the heat transport from the day side to the night side on a tidally locked planet. Therefore, we chose to model a tidally locked aquaplanet to maximize ocean heat transport. Further work could be done to explore the effect that different land configurations have on planetary heat transport and on the Snowball bifurcation for a tidally locked planet. In particular, whether the substellar region is dominated by land mass or ocean will affect evaporation and atmospheric water vapor (Chen et al., 2018), which may influence the balance of latent heat-driven atmospheric vs. oceanic heat transport.

In our simulations, we kept rotation rate (and therefore orbital period) fixed as we varied stellar irradiation. This was similarly done in previous work by Way et al. (2015); Fujii et al. (2017); Yang et al. (2019a). The advantage of this setup is that it allows us to isolate the effects of changes in radiative forcing when looking for a Snowball bifurcation. In reality, different stellar irradiations (and therefore different orbital radii) correspond to different rotation rates/orbital periods. Future work could self-consistently vary rotation rate and stellar irradiation, which may impact planetary climate (Kopparapu et al., 2016a; Haqq-Misra et al., 2018; Wolf et al., 2017).

6.5 Conclusions

The main conclusion of this chapter is that we do not find a Snowball bifurcation for tidally locked planets using a coupled ocean-atmosphere GCM (ROCKE-3D). Habitable tidally locked planets are therefore unlikely to be found in a Snowball state for a geologically significant period of time.

CHAPTER 7

NO SNOWBALL CYCLES AT THE OUTER EDGE OF THE HABITABLE ZONE FOR HABITABLE TIDALLY LOCKED PLANETS

This chapter was originally published as: Checlair, J. H., Salazar, A. M., Paradise, A., Menou, K., & Abbot, D. S. (2019). No Snowball Cycles at the Outer Edge of the Habitable Zone for Habitable Tidally Locked Planets. *The Astrophysical Journal Letters, 887*(1), L3.

7.1 Introduction

The silicate-weathering feedback is an important regulator of surface temperature on Earth and potentially other terrestrial planets (Walker et al., 1981a), as described in Chapter 1. This feedback balances the planet's volcanic outgassing rate of CO_2 with its CO_2 removal rate by weathering. The outgassing rate is a function of the planet's thermal evolution and initial volatile inventory, while the weathering rate is a function of the surface temperature and partial pressure of CO_2. If the surface temperature decreases, continental weathering slows, allowing atmospheric CO_2 to build up and bringing the temperature back up. This feedback allows a planet to maintain habitable conditions within the habitable zone (Kasting et al., 1993a). However, if the CO_2 outgassing and received stellar flux are too low, a planet would be subject to climate cycles between Snowball and warm climate states (Kadoya and Tajika, 2014; Menou, 2015; Haqq-Misra et al., 2016; Batalha et al., 2016; Abbot, 2016; Paradise and Menou, 2017). Haqq-Misra et al. (2016) suggested that climate limit cycles may not occur for planets orbiting M-stars because of the reduced ice-albedo feedback (Joshi and Haberle, 2012b; Shields et al., 2013). However, they used a 1D climate model so they could not consider the effects of tidal locking.

In this chapter we use a 3D Global Climate Model (GCM) that calculates weathering to show that tidally locked planets in the habitable zone with an active carbon cycle cannot stay in a Snowball state and will not be subject to climate cycling due to the lack of hysteresis in their climate, regardless of stellar type. They will instead settle into stable "Eyeball" states (Pierrehumbert, 2010a) with open ocean in the substellar region. The size of this unglaciated region gradually increases as the stellar irradiation or the CO_2 outgassing rate increase. We perform our simulations with a G-star spectrum, to show that these conclusions hold even if the ice-albedo feedback is strong.

7.2 Methods

We use PlaSim (Planet Simulator, Fraedrich et al. (2005)), an intermediate-complexity 3D GCM. We simulate and compare both a rapidly rotating and a tidally locked configuration. In both cases, we use the same PlaSim configuration as Checlair et al. (2017), with 32 latitudes, 64 longitudes, and 10 vertical layers. In order to isolate the effects of tidal locking, we perform simulations with a G-star spectrum here. One important aspect of PlaSim that we will later refer to is that the sea ice scheme assumes that a gridbox is either completely covered with sea ice or completely ice-free, so that partial sea ice coverage of a grid box is not allowed.

We modified PlaSim following the method of Paradise and Menou (2017) to calculate the weathering rate at every model gridbox and timestep for a fixed amount of atmospheric CO_2. This method is similar to that of Edson et al. (2012). We use the weathering rate formulation used by Menou (2015), which is based on a parameterization of Earth's continental silicate-weathering in the absence of plants and is motivated by observations and laboratory measurements:

$$\frac{W}{W_\oplus} = \begin{cases} \left(\frac{pCO_2}{pCO_{2,\oplus}}\right)^\beta e^{[k_{act}(T_s-288)]} \left[1 + k_{run}(T_s - 288)\right]^{0.65}, & \text{if } T_s \geq 273.15K \\ \frac{W}{W_\oplus} = 0, & \text{if } T_s < 273.15K \end{cases} \tag{7.1}$$

where T_s is the surface temperature, $pCO_{2,\oplus}$ is the pre-industrial pCO_2 of 330 μbar, and

$W_\oplus$ is the weathering rate at T_s = 288 K. k_{act} is related to the chemical activation energy of the weathering reaction and is set to 0.09, and k_{run} is a runoff efficiency factor set to 0.045, which helps account for changes in precipitation. β is the dependence on pCO_2, and is set to 0.5 (Kump et al., 2000; Pierrehumbert, 2010b; Menou, 2015). As in Paradise and Menou (2017), we evaluate Equation 7.1 at each land grid cell if the surface temperature is above 273.15 K every 6 hours of model simulation. These local rates are then averaged over the planet to obtain globally averaged weathering rates.

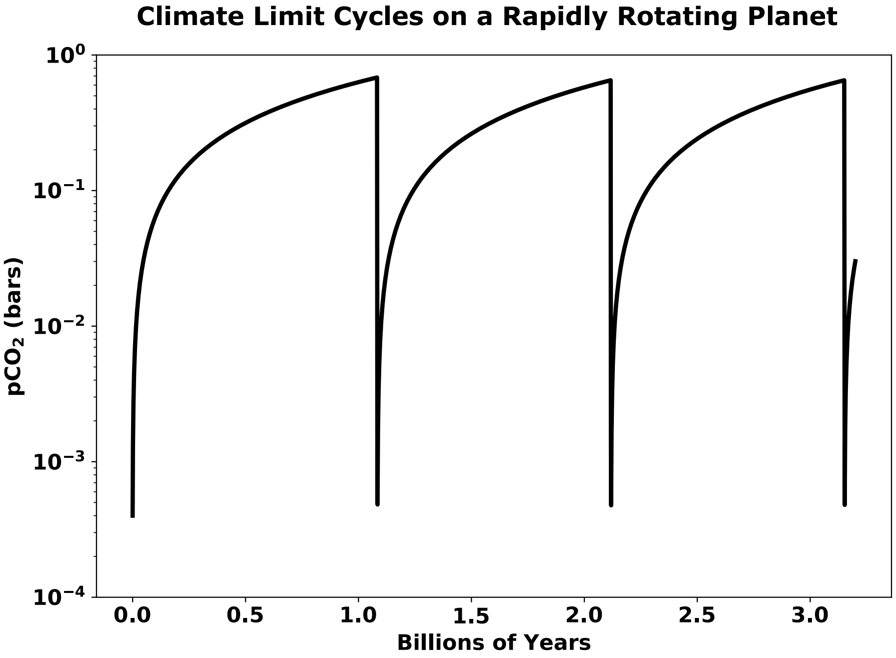

Figure 7.1: **Rapidly rotating Earth-like planets with low outgassing rates are subject to climate limit cycles between warm and Snowball states.** This figure shows the CO_2 cycles between Warm and Snowball climate states for a rapidly rotating Earth-like planet. Since weathering is near zero in the Snowball state, the CO_2 slowly builds up until a critical point at which the planet deglaciates. Warm continent is then exposed, allowing weathering, and the CO_2 rapidly decreases until the Snowball state is entered again. The timescale from the initial deglaciation to the reglaciation is geologically instantaneous. Outgassing rate is set to $V = 0.09\ V_\oplus$. Stellar irradiation is fixed at 1300 Wm^{-2}.

We run a total of 24 simulations with fixed values of CO_2 pressure ranging from 0.1 to 4.6×10^5 μbars. Each simulation is run for 100 years, or until thermal equilibrium is reached.

We compute the globally averaged weathering rate for each of these fixed CO_2 pressures at equilibrium using the method laid out in Section 6.2. This gives us weathering as a function of CO2 (W(CO2)). Note that the Snowball bifurcation allows W(CO2) to be multivalued. We evolve CO_2 in time using the differential equation

$$\frac{d}{dt}CO_2 = V - W(CO_2) \tag{7.2}$$

for a chosen outgassing rate (V). In this work we assume Earth's outgassing rate is $V_\oplus = 7$ bars Gyr^{-1} as in Menou (2015).

7.3 Results

7.3.1 Rapidly rotating planet

First, we reproduce the results of Paradise and Menou (2017) who demonstrated that CO_2 limit cycles occur for an Earth-like rapidly rotating planet at a stellar irradiation of 1300 Wm^{-2}. We plot cycles for an outgassing rate of $V = 0.09\ V_\oplus$ in Figure 7.1, and obtain cycles similar to those of Paradise and Menou (2017) (see their Figure 3).

Paradise and Menou (2017) used an outgassing rate an order of magnitude lower than ours, yet the periods of our cycles unexpectedly differ only slightly. This is due to different assumptions made in obtaining our normalizing factors and to a conversion factor bug in their work that was fixed for this work. These differences do not change the qualitative nature of their results. In addition to this, the timescales found in both of our results are highly dependent on our simplified weathering prescription and should therefore be taken only as qualitative results.

Next, we vary the outgassing rate in Equation 7.2 to search for the value at which a climate cycle first appears. We summarize our results in Figure 7.2. When no cycle occurs, the planet is in a stable state and we plot the equilibrium CO_2 (red solid line, Warm state).

When cycles occur, the planet is in a nonlinear limit cycle, and we plot the maximum and minimum CO_2 pressures for that cycle (red and blue dashed lines, Warm and Snowball states). Outgassing rates higher than 0.87 bars Gyr^{-1} (0.12 $V_{\oplus}$) do not allow for climate cycles. This is roughly an order of magnitude higher than what Paradise and Menou (2017) found and can be attributed to the conversion factor bug mentioned above. We note that the critical outgassing value at a stellar irradiation of 1300 Wm^{-2} is still one order of magnitude smaller than Earth's outgassing.

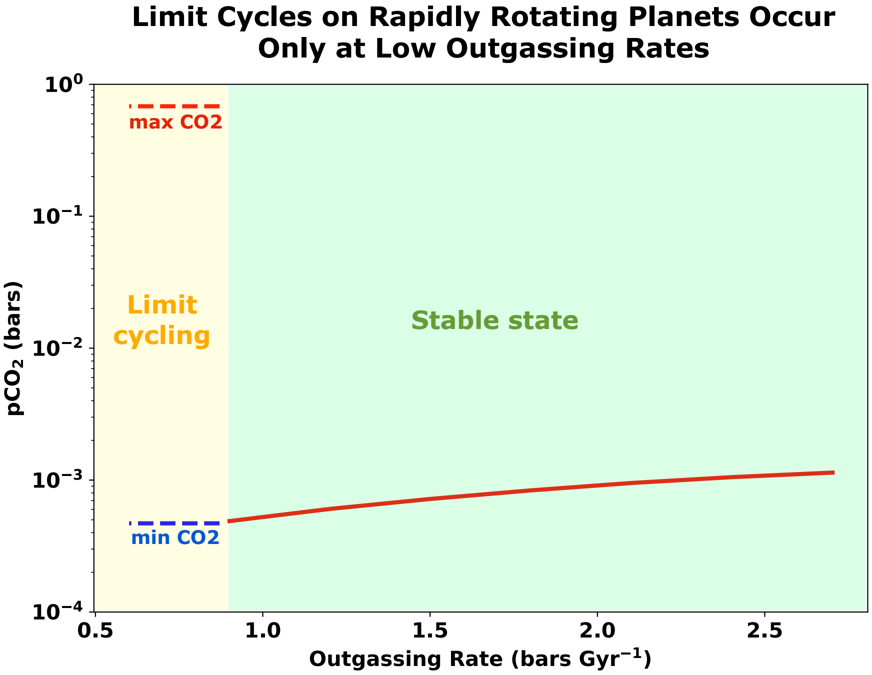

Figure 7.2: **Outgassing rates must be lower than a critical value to allow for climate limit cycles between warm and Snowball states on rapidly rotating Earth-like planets.** This figure shows that for a stellar irradiation of 1300 Wm^{-2}, the outgassing rate must be lower than the critical value of 0.87 bars Gyr^{-1} (0.12 $V_{\oplus}$) to allow for climate cycles. The dashed lines represent the upper (red dashed) and lower (blue dashed) limits between which CO_2 oscillates as part of a nonlinear limit cycle when the outgassing rate is lower than the critical value. The solid line represents climates where the outgassing rate is too high for limit cycles to occur so that CO_2 equilibrates to a fixed value with the planet in a stable Warm state. One exception to this figure is if the outgassing rate is too low to build up sufficient CO_2 to deglaciate a planet over its habitable zone lifetime, in which case it will not cycle and remain in a Snowball state.

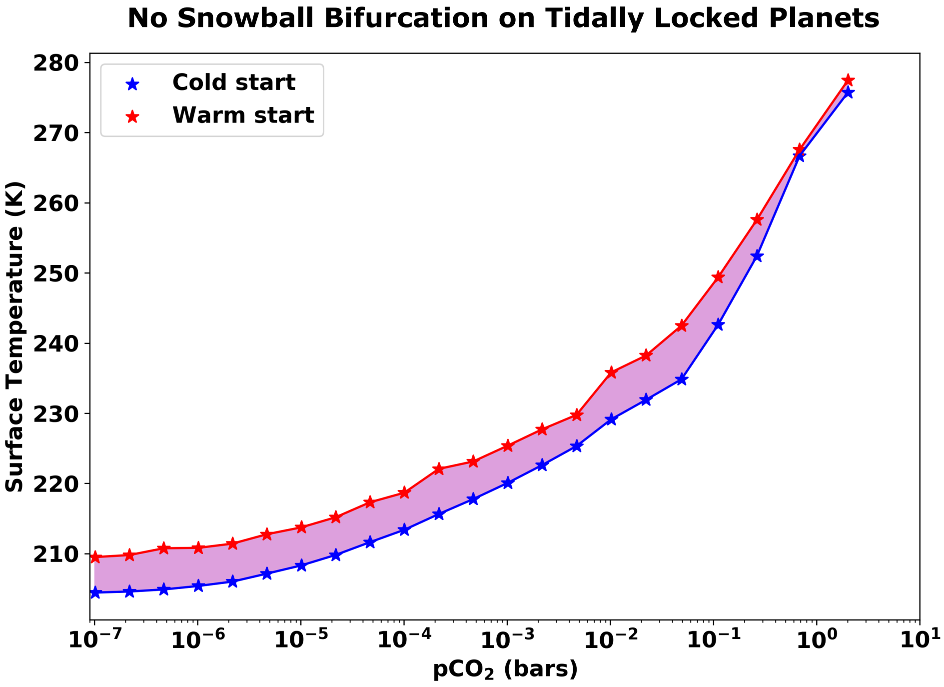

Figure 7.3: **Tidally locked planets do not exhibit a Snowball bifurcation.** Planets initialized from both an ice-free (red) and an ice-covered (blue) state equilibrate to the same final continuum of states (purple). Stellar irradiation is fixed at 1100 Wm^{-2}.

7.3.2 Tidally locked planet

We begin by reproducing the results of Checlair et al. (2017), who showed that habitable tidally locked planets do not exhibit a Snowball bifurcation, but here we vary CO_2 rather than stellar irradiation. We refer the reader to Checlair et al. (2017) (Figure 7) for a bifurcation diagram of a rapidly-rotating planet exhibiting the Snowball bifurcation. Specifically, we compute the globally averaged equilibrium surface temperature for a planet initialized from a warm (globally ice-free) and a cold (globally ice-covered) state for a variety of CO_2 pressures with a stellar irradiation of 1100 Wm^{-2} and a G-star spectrum (Figure 7.3). We find similar results to Checlair et al. (2017), with a single continuum of states smeared over about 5K in global mean temperature and no bifurcation. This compares to a difference in temperature of 40-60K between the warm and cold states when there is a bifurcation (Checlair et al., 2017).

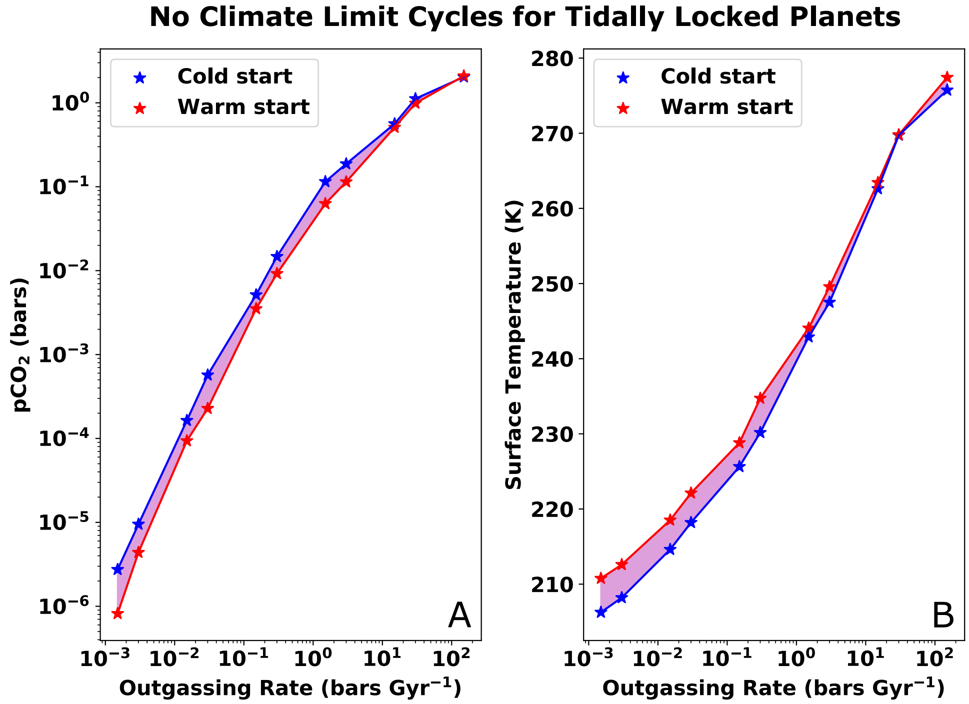

Figure 7.4: **Tidally locked planets do not go through climate limit cycles.** As the outgassing rate is increased, the equilibrium CO_2 pressure (A) and surface temperature (B) increase. This corresponds to an "Eyeball planet" with a substellar unglaciated region gradually increasing in size. This is a result of tidally locked planets lacking the Snowball bifurcation. Stellar irradiation is fixed at 1100 Wm^{-2}. The purple shaded region represents a continuum of states. Note that we consider extremely low CO_2 outgassing rates.

Any simulation started within the continuum of states equilibrates to the same state it started in. The continuum of states is an artifact of PlaSim's simple sea ice scheme where a grid cell can only be fully ice-covered or fully ice-free. We refer the reader to Checlair et al. (2017) (Appendix) for further analysis on the origin of the continuum of states and here simply note that it is unrelated to the Snowball bifurcation. In separate work (Checlair et al., 2019b), we used ROCKE-3D, a sophisticated 3D-GCM that allows for partially ice-covered grid cells (Way et al., 2017), to reproduce these results for a tidally locked aquaplanet and found no continuum of states. We repeated these calculations for other stellar irradiations and found similar results. However, we note that we are never able to reach a fully glaciated state in a Warm State configuration and a fully ice free state in a Cold Start configuration for the same value of irradiation. The reason for this is that the partially glaciated state is stable over an extremely large range of radiative forcing and the PlaSim radiation scheme becomes significantly less accurate for CO_2 values greater than $\sim$1 bar.

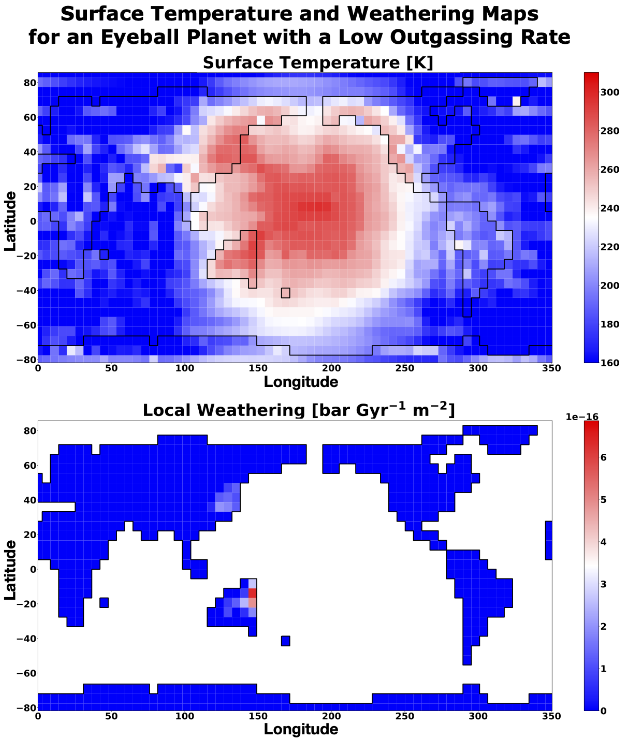

Figure 7.5: **Example equilibrium state of a tidally locked planet at the outer edge of the habitable zone. The planet is in an Eyeball state with an unglaciated region centered at the substellar point.** This figure shows maps of the equilibrated annual mean surface temperature (top) and weathering rate (bottom) of a tidally locked planet at a very low equilibrium outgassing rate of 1.1×10^{-3} bars/Gyr (1.66×10^{-4} $V_\oplus$). The unglaciated region expands just enough for the temperature to be high enough in a small region of land that weathering there can balance this low CO_2 outgassing rate. Stellar irradiation is fixed at 1100 Wm^{-2}. The horizontal axis is longitude and the vertical axis is latitude.

To investigate whether climate cycles can occur on tidally locked planets, we proceed with the same method used in our rapidly rotating case (Section 7.3.1). As Figure 7.4 shows, the planet equilibrates to a fixed value of CO_2 for all outgassing rates and no cycles occur. Note that this is true even for extremely low CO_2 outgassing rates, even three orders of magnitude lower than Earth's. The gap between the two curves (purple shaded region) is again due to the continuum of states that results from PlaSim's sea ice scheme.

Instead of cycling between warm and Snowball states, tidally locked planets settle into an "Eyeball" state with open ocean in the substellar region (Pierrehumbert, 2010a). This is shown in Figure 7.5, where we map equilibrated annual-mean surface temperature and weathering rate for a tidally locked planet at an equilibrium outgassing rate of 1.1×10^{-3} bars/Gyr, or 1.66×10^{-4} $V_{\oplus}$. Figure 7.5 suggests that the size of the open ocean region will be strongly dependent on the continental configuration. For a low CO_2 outgassing rate, the climate adjusts so that the temperature is above freezing and weathering occurs in only a small region of land. If there is land closer to the substellar point, then the open ocean region will be smaller. Small increases in temperature cause large increases in weathering rate (Equation 7.1), so the climate can exist in a very similar state for a large range of CO_2 outgassing rates.

The position of the continents affects the weathering rate. To investigate this effect, we moved the substellar point from over the Pacific ocean (our default case) to over the African continent. We reproduced Figure 7.4 for these cases and found that although our qualitative results remained the same, the equilibrium surface temperatures and the CO_2 pressures reached for each outgassing rate vary as a function of substellar point location. Given that a planet will always move towards weathering-outgassing equilibrium, sea ice must retreat until enough land is exposed for weathering to match outgassing. The distance between the substellar point and land therefore sets an upper limit on the amount of open ocean a tidally locked planet can have. Proximity of land to the substellar point on habitable tidally locked planets is therefore a dominant factor in determining equilibrium sea ice extent for a given outgassing rate.

7.4 Discussion

The most important outcome of this work is that tidally locked planets will not experience climate limit cycles. This is in contrast to rapidly rotating planets that can oscillate between globally ice-covered and globally ice-free states at low stellar irradiation and CO_2 outgassing. The difference between these two configurations is due to the stellar irradiation pattern of tidally locked planets, which suppresses the Snowball bifurcation and hysteresis. Instead of limit cycling, we predict that tidally locked planets with an active carbon cycle will be found in an "Eyeball" state with a deglaciated substellar region. Moreover, we do not expect to find a tidally locked planet with an active carbon cycle in a globally glaciated state for a geologically significant period of time. If the planet were ever perturbed into a Snowball state with zero weathering, it would quickly reopen ocean in the substellar region due to warming from CO_2 outgassing.

This may have important implications for the habitability of planets in the outer regions of the habitable zone, but these implications may be complex and are difficult for us to predict. Oscillating in and out of a Snowball may eradicate some complex developed life forms, while being settled in an Eyeball state may allow them to survive and evolve. On the other hand, periods of global glaciation on Earth may be associated with an increase in atmospheric oxygen concentration (Hoffman and Schrag, 2002; Laakso and Schrag, 2014, 2017b) as well as an increase in the complexity of life (Kirschvink, 1992; Hoffman et al., 1998). Snowball events may therefore be essential for the increase in complexity of life.

The weathering parameterization used in Equation 7.1 assumes that the weathering rate is a function of only temperature and not of precipitation following Menou (2015). This assumes that precipitation scales linearly with temperature. This assumption is a source of uncertainty in our local weathering calculations. In addition to this, the weathering parameters used in Equation 7.1 (β, k_{act}, k_{run}) themselves are highly uncertain (e.g., Kump et al., 2000). However, these caveats will only affect our quantitative results. For example, for a rapidly rotating planet the critical outgassing rate at which a cycle first appears and the period of cycles at any given outgassing rate may be different for different values of weathering parameters. For a tidally locked planet, the size of the unglaciated substellar region at a given stellar irradiation may depend on the details of the weathering scheme.

However, the fact that tidally locked planets do not go through climate limit cycles is a result of their lack of a Snowball bifurcation and is independent of the weathering parameterization.

7.5 Conclusions

The main conclusions of this chapter are:

1. Tidally locked planets should not exhibit climate limit cycles. This is in contrast to rapidly rotating planets such as Earth, which will oscillate between Snowball and warm climate states for CO_2 outgassing rates and stellar irradiations that are too low to maintain the warm state.
2. Tidally locked planets are likely to instead settle into an "Eyeball" state with an unglaciated substellar region. The distance between the substellar point and land sets an upper limit on the amount of open ocean a tidally locked planet can have. More generally, the size of this region is set by the stellar irradiation received by the planet, the rate of CO_2 outgassing, and the distribution of continents.

CHAPTER 8

SUMMARY AND OUTLOOK

8.1 Summary of Results

The next few decades are expected to be very productive for exoplanet science. In the near future, the James Webb Space Telescope (JWST) will allow us to spectrally characterize terrestrial planets orbiting M-stars. In the more distant future, telescopes such as LUVOIR and HabEx will allow us to direct image Earth-sized habitable zone terrestrial planets orbiting Sun-like stars (exoEarths). To address these two prospects, this dissertation explored the habitability of both G-star and M-star habitable zone planets.

In part 1 of this dissertation, I focused on habitable zone planets around Sun-like stars, and explored testing key theories of habitability statistically with direct imaging missions. These tests would exploit statistical marginalization of uncertainty inherent to both terrestrial planets and observations by using large samples of detected exoEarths.

In Chapter 2, I proposed a statistical test for the silicate-weathering feedback, which is a stabilizing negative feedback believed to help maintain habitable conditions on habitable zone planets. Specifically, I proposed measuring CO_2 on a large number of exoEarths, and testing for whether a negative trend between CO_2 and irradiation can be confirmed statistically. Such a trend would indicate a working negative feedback on exoEarths. I explored the feasibility of such a test for future direct imaging missions LUVOIR and HabEx. My main findings are that if the silicate-weathering feedback is common on exoEarths, we are highly likely to detect it with LUVOIR-A, and may detect it with LUVOIR-B if the natural spread of planetary parameters is small. We are unlikely to detect it with HabEx due to its small expected exoEarth yield.

In Chapter 3, I developed a statistical test for whether exoEarths tend to be Earth-like. Specifically, I considered whether observations with LUVOIR and HabEx could inform us on the fraction of exoEarths that are Earth-like (f_E) in that they develop Earth-like, O_2-

producing life (oxygenic photosynthesis) that oxygenates their atmospheres roughly following Earth's oxygenation history. I first showed that the probability of not detecting O_2 or O_3 on any exoEarth, even if all of them are Earth-like, depends mainly on the yield of detectable exoEarths, which depends on the occurrence rate of exoEarths ($\eta_\oplus$) and on the instrument's mirror diameter. Then, I considered whether we could constrain the fraction of exoEarths that are Earth-like (f_E) in the event of a null detection of O_2 or O_3 on every exoEarth. The constraint that could be placed on f_E, whether or not we detect O_2 or O_3 on exoEarths, can only be an upper limit. The possibility of false positive scenarios prevent us from placing a lower limit on f_E even if we detect O_2 or O_3 on some exoEarths, and if we do not detect any O_2 or O_3, the null detection f_E could be explained by $f_E = 0$. I found that the extent to which we may be able to constrain f_E in the case of a null detection relies primarily on exoEarth yield (and therefore on $\eta_\oplus$ and mirror diameter), as well as on the ability to detect low levels of O_3. In general, large estimates of $\eta_\oplus$ will allow us to constrain f_E to different extents with both LUVOIR and HabEx. Constraining f_E in the case of a null detection with intermediate estimates of $\eta_\oplus$ will necessitate a larger telescope such as LUVOIR-A or LUVOIR-B. The lowest estimates of $\eta_\oplus$ will prevent us from constraining f_E entirely. Missions with larger aperture mirrors are therefore more robust to uncertainties in $\eta_\oplus$, but all missions are vulnerable to inconclusive null detections if $\eta_\oplus$ is very low.

In Chapter 4, I quantified the detectability of O_2 and O_3 for future direct imaging missions LUVOIR and HabEx using a 3D Global Climate Model. This allowed me to include realistic cloud coverage and to calculate atmospheric profiles photochemically in 3D. I found that realistic cloud coverage increases the detectability of both O_2 and O_3, despite the fact that clouds obstruct some of the absorbing gas column mass. That is because clouds have a strong effect on planetary reflectivity for planets with a low-to-intermediate surface albedo, which raises the spectrum continuum and therefore increases the absorbing feature's signal.

In part 2 of this dissertation, I focused on habitable zone planets orbiting M-stars, which are expected to be tidally locked. Specifically, I explored the Snowball bifurcation on tidally locked planets.

In Chapter 5, I showed that tidally locked planets do not exhibit a Snowball bifurcation, regardless of stellar spectrum, as a direct result of the spatial pattern of insolation they receive. Instead, they will smoothly transition from partial to complete ice coverage and back. The main implication of this is that we should not find habitable tidally locked exoplanets that have an active carbon cycle in a Snowball state for a geologically significant period of time.

In Chapter 6, I included a dynamic ocean to explore whether realistic ocean heat transport can reintroduce the Snowball bifurcation for habitable tidally locked planets by destabilizing partially glaciated states. I showed that including ocean heat transport does not reintroduce the Snowball bifurcation and that the lack of a Snowball bifurcation on tidally locked planets is robust to realistic levels of ocean heat transport.

In Chapter 7, I explored whether limit cycling between Warm and Snowball states at the outer edge of the habitable zone occurs for tidally locked planets. I showed that tidally locked planets with an active carbon cycle will not experience limit cycling as a result of their lack of a Snowball bifurcation. Instead, outer edge tidally locked planets will settle into "Eyeball" states with a small unglaciated substellar region.

8.2 Closing Thoughts and Outlook

As we plan to observe habitable zone terrestrial planets orbiting Sun-like stars with future direct imaging missions such as LUVOIR or HabEx, it is important to carefully consider the ways in which we could maximize the missions' scientific return. This is especially important in the event where we do not detect any convincing evidence of life. The large yield of exoEarths presents us with an exciting opportunity to test key theories of habitability by statistically marginalizing over uncertainties inherent to terrestrial planets and their observations. In this dissertation, I proposed testing the concept of the habitable zone, as well as testing whether exoEarths tend to be Earth-like. I showed that the feasibility of these tests depends strongly on the mission's exoEarth yield. Because of that, missions with a larger aperture mirrors may be necessary for statistical tests, as the mirror diameter is the primary factor affecting a mission's exoEarth yield.

In the next few years (fingers crossed), JWST will launch and is expected to find and will attempt to characterize numerous terrestrial planets around M-stars, some of which may be orbiting within the habitable zone. M-star habitable zone planets will orbit very close to their stars and are expected to be tidally locked. In this dissertation, I showed that habitable tidally locked planets do not exhibit a Snowball bifurcation and do not limit cycle between Warm and Snowball states. Instead, they smoothly and gradually glaciate and deglaciate. They are therefore not expected to be found in a Snowball state for a geologically significant period time if they have an active carbon cycle. This presents some implications for their habitability. Snowball events could be an acute stressor on existing life, but they could also increase the complexity of life and the atmospheric oxygen concentration, as those events seem to have been correlated on Earth. Oxygen is a promising biosignature, and its joint detection with other biogenic gases may be one of our best avenues to detecting convincing evidence of life. If Snowball events are necessary to evolve complex life and build up atmospheric oxygen concentration, tidally locked habitable zone planets may be found to lack both complex life and detectable levels of oxygen.

REFERENCES

Abbot, D. S. (2016). Analytical investigation of the decrease in the size of the habitable zone due to limited CO_2 outgassing rate. *The Astrophysical Journal*, 827:117.

Abbot, D. S., Voigt, A., and Koll, D. (2011a). The Jormungand global climate state and implications for Neoproterozoic glaciations. *Journal of Geophysical Research: Atmospheres*, 116(D18).

Abbot, D. S., Voigt, A., and Koll, D. (2011b). The Jormungand global climate state and implications for Neoproterozoic Glaciations. *Journal of Geophysical Research*, 116.

Abe, Y., Abe-Ouchi, A., Sleep, N. H., and Zahnle, K. J. (2011). Habitable zone limits for dry planets. *Astrobiology*, 11(5):443–460.

Allard, F., Homeier, D., and Freytag, B. (2012). Models of very-low-mass stars, brown dwarfs and exoplanets. *Philosophical Transactions of the Royal Society A: Mathematical, Physical and Engineering Sciences*, 370(1968):2765–2777.

Anglada-Escudé, G., Amado, P. J., Barnes, J., Berdinas, Z. M., Butler, R. P., Coleman, G. A., de la Cueva, I., Dreizler, S., Endl, M., Giesers, B., et al. (2016). A terrestrial planet candidate in a temperate orbit around proxima centauri. *Nature*, 536(7617):437–440.

Barnes, R., Deitrick, R., Luger, R., Driscoll, P. E., Quinn, T. R., Fleming, D. P., Guyer, B., McDonald, D. V., Meadows, V. S., Arney, G., et al. (2016). The Habitability of Proxima Centauri b I: Evolutionary Scenarios. *arXiv preprint arXiv:1608.06919*.

Barstow, J. K. and Irwin, P. G. (2016). Habitable worlds with jwst: transit spectroscopy of the trappist-1 system? *Monthly Notices of the Royal Astronomical Society: Letters*, 461(1):L92–L96.

Batalha, N. E., Kopparapu, R. K., Haqq-Misra, J., and Kasting, J. F. (2016). Climate cycling on early mars caused by the carbonate–silicate cycle. *Earth and Planetary Science Letters*, 455:7–13.

Bean, J. L., Abbot, D. S., and Kempton, E. M.-R. (2017). A statistical comparative planetology approach to the hunt for habitable exoplanets and life beyond the solar system. *The Astrophysical Journal Letters*, 841(2):L24.

Belikov, R., Stark, C., Angerhausen, D., Apai, D., Bendek, E., Bennett, D., Blackwood, G., Boss, A., Brown, R., Bryden, G., et al. (2017). Exoplanet occurrence rates and distributions. *ExoPAG SAG-13 Final Report*.

Berggren, R. and Labitzke, K. (1966). A detailed study of the horizontal and vertical distribution of ozone 1. *Tellus*, 18(4):761–772.

Berner, R. A. and Berner, R. A. (2004). *The Phanerozoic carbon cycle:* CO_2 *and* O_2. Oxford University Press on Demand.

Berner, R. A. and Caldeira, K. (1997). The need for mass balance and feedback in the geochemical carbon cycle. *Geology*, 25(10):955–956.

Bishop, C. M. (2006). Pattern recognition. *Machine learning*, 128(9).

Bitz, C., Holland, M., Hunke, E., and Moritz, R. (2005). Maintenance of the sea-ice edge. *Journal of climate*, 18(15):2903–2921.

Bixel, A. and Apai, D. (2020). Testing Earth-like atmospheric evolution on exo-Earths through oxygen absorption: required sample sizes and the advantage of age-based target selection. *arXiv preprint arXiv:2005.01587*.

Board, S. S., National Academies of Sciences, E., Medicine, et al. (2019). *Exoplanet Science Strategy*. National Academies Press.

Boccaletti, G., Ferrari, R., Adcroft, A., Ferreira, D., and Marshall, J. (2005). The vertical structure of ocean heat transport. *Geophysical Research Letters*, 32(10).

Bolmont, E., Selsis, F., Owen, J. E., Ribas, I., Raymond, S. N., Leconte, J., and Gillon, M. (2017). Water loss from terrestrial planets orbiting ultracool dwarfs: implications for the planets of TRAPPIST-1. *Monthly Notices of the Royal Astronomical Society*, 464(3):3728–3741.

Bond, I. A., Udalski, A., Jaroszyński, M., Rattenbury, N., Paczyński, B., Soszyński, I., Wyrzykowski, L., Szymański, M., Kubiak, M., Szewczyk, O., et al. (2004). Ogle 2003-blg-235/moa 2003-blg-53: a planetary microlensing event. *The Astrophysical Journal Letters*, 606(2):L155.

Borucki, W. J., Koch, D., Basri, G., Batalha, N., Brown, T., Caldwell, D., Caldwell, J., Christensen-Dalsgaard, J., Cochran, W. D., DeVore, E., et al. (2010). Kepler planet-detection mission: introduction and first results. *Science*, 327(5968):977–980.

Brocks, J. J., Jarrett, A. J., Sirantoine, E., Hallmann, C., Hoshino, Y., and Liyanage, T. (2017). The rise of algae in cryogenian oceans and the emergence of animals. *Nature*, 548(7669):578.

Budyko, M. I. (1969). The effect of solar radiation variations on the climate of the Earth. *Tellus*, 21(5):611–619.

Burke, C. J., Christiansen, J. L., Mullally, F., Seader, S., Huber, D., Rowe, J. F., Coughlin, J. L., Thompson, S. E., Catanzarite, J., Clarke, B. D., et al. (2015). Terrestrial planet occurrence rates for the Kepler GK dwarf sample. *The Astrophysical Journal*, 809(1):8.

Burrows, A. S. (2014). Spectra as windows into exoplanet atmospheres. *Proceedings of the National Academy of Sciences*, 111(35):12601–12609.

Caldeira, K. and Kasting, J. F. (1992). The life span of the biosphere revisited. *Nature*, 360(6406):721–723.

Catanzarite, J. and Shao, M. (2011). The occurrence rate of Earth analog planets orbiting Sun-like stars. *The Astrophysical Journal*, 738(2):151.

Catling, D., Buick, R., Brownlee, D., and Newport, S. (2019). Atmospheric CO_2 levels from 2.7 billion years ago using micrometeorite oxidation.

Caves, J. K., Jost, A. B., Lau, K. V., and Maher, K. (2016). Cenozoic carbon cycle imbalances and a variable weathering feedback. *Earth and Planetary Science Letters*, 450:152–163.

Chapman, S. (1930). Xxxv. on ozone and atomic oxygen in the upper atmosphere. *The London, Edinburgh, and Dublin Philosophical Magazine and Journal of Science*, 10(64):369–383.

Charbonneau, D., Brown, T. M., Latham, D. W., and Mayor, M. (1999). Detection of planetary transits across a sun-like star. *The Astrophysical Journal Letters*, 529(1):L45.

Checlair, J., Menou, K., and Abbot, D. S. (2017). No snowball on habitable tidally locked planets. *The Astrophysical Journal*, 845(2):132.

Checlair, J. H., Abbot, D. S., Webber, R. J., Feng, Y. K., Bean, J. L., Schwieterman, E. W., Stark, C. C., Robinson, T. D., Kempton, E., Alcabes, O. D., et al. (2019a). A statistical comparative planetology approach to maximize the scientific return of future exoplanet characterization efforts. *arXiv preprint arXiv:1903.05211*.

Checlair, J. H., Olson, S. L., Jansen, M. F., and Abbot, D. S. (2019b). No snowball on habitable tidally locked planets with a dynamic ocean. *The Astrophysical Journal Letters*, 884(2):L46.

Checlair, J. H., Villanueva, G. L., Hayworth, B. P., Olson, S. L., Komacek, T. D., Robinson, T. D., Popović, P., Yang, H., and Abbot, D. S. (2021). Probing the capability of future direct-imaging missions to spectrally constrain the frequency of Earth-like planets. *The Astronomical Journal*, 161(3):150.

Chen, H., Wolf, E. T., Kopparapu, R., Domagal-Goldman, S., and Horton, D. E. (2018). Biosignature anisotropy modeled on temperate tidally locked m-dwarf planets. *The Astrophysical Journal Letters*, 868(1):L6.

Collins, W. D., Bitz, C. M., Blackmon, M. L., Bonan, G. B., Bretherton, C. S., Carton, J. A., Chang, P., Doney, S. C., Hack, J. J., Henderson, T. B., et al. (2006). The community climate system model version 3 (ccsm3). *Journal of Climate*, 19(11):2122–2143.

Cowan, N., Greene, T., Angerhausen, D., Batalha, N., Clampin, M., Colón, K., Crossfield, I., Fortney, J., Gaudi, B., Harrington, J., et al. (2015). Characterizing transiting planet atmospheres through 2025. *Publications of the Astronomical Society of the Pacific*, 127(949):311.

Cowan, N. B., Agol, E., Meadows, V. S., Robinson, T., Livengood, T. A., Deming, D., Lisse, C. M., A'Hearn, M. F., Wellnitz, D. D., Seager, S., et al. (2009). Alien maps of an ocean-bearing world. *The Astrophysical Journal*, 700(2):915.

Cowan, N. B., Voigt, A., and Abbot, D. S. (2012). Thermal phases of Earth-like planets: Estimating thermal inertia from eccentricity, obliquity, and diurnal forcing. *The Astrophysical Journal*, 757(1):80.

Del Genio, A. D., Way, M. J., Amundsen, D. S., Aleinov, I., Kelley, M., Kiang, N. Y., and Clune, T. L. (2017). Habitable climate scenarios for proxima centauri b with a dynamic ocean. *Astrobiology*, 19(1):99–125.

Deming, D., Seager, S., Winn, J., Miller-Ricci, E., Clampin, M., Lindler, D., Greene, T., Charbonneau, D., Laughlin, G., Ricker, G., et al. (2009). Discovery and characterization of transiting super Earths using an all-sky transit survey and follow-up by the James Webb Space Telescope. *Publications of the Astronomical Society of the Pacific*, 121(883):952.

Des Marais, D. J., Harwit, M. O., Jucks, K. W., Kasting, J. F., Lin, D. N., Lunine, J. I., Schneider, J., Seager, S., Traub, W. A., and Woolf, N. J. (2002). Remote sensing of planetary properties and biosignatures on extrasolar terrestrial planets. *Astrobiology*, 2(2):153–181.

Dittmann, J. A., Irwin, J. M., Charbonneau, D., Bonfils, X., Astudillo-Defru, N., Haywood, R. D., Berta-Thompson, Z. K., Newton, E. R., Rodriguez, J. E., Winters, J. G., et al. (2017). A temperate rocky super-Earth transiting a nearby cool star. *Nature*, 544(7650):333.

Dodd, M. S., Papineau, D., Grenne, T., Slack, J. F., Rittner, M., Pirajno, F., O'Neil, J., and Little, C. T. (2017). Evidence for early life in Earth's oldest hydrothermal vent precipitates. *Nature*, 543(7643):60–64.

Dole, S. H. (1964). Habitable planets for man. *Blaisdell Publishing Company, New York*.

Donohoe, A. and Battisti, D. S. (2011). Atmospheric and surface contributions to planetary albedo. *Journal of Climate*, 24(16):4402–4418.

Edmond, J. M. and Huh, Y. (2003). Non-steady state carbonate recycling and implications for the evolution of atmospheric pCO_2. *Earth and Planetary Science Letters*, 216(1-2):125–139.

Edson, A. R., Kasting, J. F., Pollard, D., Lee, S., and Bannon, P. R. (2012). The carbonate-silicate cycle and CO_2/climate feedbacks on tidally locked terrestrial planets. *Astrobiology*, 12(6):562–571.

Fally, S., Vandaele, A. C., Carleer, M., Hermans, C., Jenouvrier, A., Mérienne, M.-F., Coquart, B., and Colin, R. (2000). Fourier transform spectroscopy of the O_2 herzberg bands. III. absorption cross sections of the collision-induced bands and of the herzberg continuum. *Journal of molecular spectroscopy*, 204(1):10–20.

Feng, Y. K., Robinson, T. D., Fortney, J. J., Lupu, R. E., Marley, M. S., Lewis, N. K., Macintosh, B., and Line, M. R. (2018). Characterizing Earth analogs in reflected light: atmospheric retrieval studies for future space telescopes. *The Astronomical Journal*, 155(5):200.

Ferreira, D., Marshall, J., and Rose, B. (2011). Climate determinism revisited: multiple equilibria in a complex climate model. *Journal of Climate*, 24(4):992–1012.

Fraedrich, K., Jansen, H., Kirk, E., Luksch, U., and Lunkeit, F. (2005). The Planet Simulator: Towards a user friendly model. *Meteorologische Zeitschrift*, 14(3):299–304.

Fujii, Y., Del Genio, A. D., and Amundsen, D. S. (2017). Nir-driven moist upper atmospheres of synchronously rotating temperate terrestrial exoplanets. *The Astrophysical Journal*, 848(2):100.

Fujii, Y., Kawahara, H., Suto, Y., Fukuda, S., Nakajima, T., Livengood, T. A., and Turner, E. L. (2011). Colors of a second Earth. II. effects of clouds on photometric characterization of Earth-like exoplanets. *The Astrophysical Journal*, 738(2):184.

Fujii, Y., Kawahara, H., Suto, Y., Taruya, A., Fukuda, S., Nakajima, T., and Turner, E. L. (2010). Colors of a second Earth: estimating the fractional areas of ocean, land, and vegetation of Earth-like exoplanets. *The Astrophysical Journal*, 715(2):866.

Gardner, J. P., Mather, J. C., Clampin, M., Doyon, R., Greenhouse, M. A., Hammel, H. B., Hutchings, J. B., Jakobsen, P., Lilly, S. J., Long, K. S., et al. (2006). The james webb space telescope. *Space Science Reviews*, 123(4):485–606.

Gaudi, B. S., Seager, S., Mennesson, B., Kiessling, A., Warfield, K., Cahoy, K., Clarke, J. T., Domagal-Goldman, S., Feinberg, L., Guyon, O., et al. (2020). The habitable exoplanet observatory (habex) mission concept study final report. *arXiv preprint arXiv:2001.06683*.

Gelaro, R., McCarty, W., Suárez, M. J., Todling, R., Molod, A., Takacs, L., Randles, C. A., Darmenov, A., Bosilovich, M. G., Reichle, R., et al. (2017). The modern-era retrospective analysis for research and applications, version 2 (merra-2). *Journal of Climate*, 30(14):5419–5454.

Gillon, M., Triaud, A. H., Demory, B.-O., Jehin, E., Agol, E., Deck, K. M., Lederer, S. M., De Wit, J., Burdanov, A., Ingalls, J. G., et al. (2017). Seven temperate terrestrial planets around the nearby ultracool dwarf star trappist-1. *Nature*, 542(7642):456–460.

Hansen, J., Sato, M., and Ruedy, R. (1997). Radiative forcing and climate response. *Journal of Geophysical Research: Atmospheres*, 102(D6):6831–6864.

Haqq-Misra, J., Kopparapu, R. K., Batalha, N. E., Harman, C. E., and Kasting, J. F. (2016). Limit cycles can reduce the width of the habitable zone. *The Astrophysical Journal*, 827(2):120.

Haqq-Misra, J., Wolf, E. T., Joshi, M., Zhang, X., and Kopparapu, R. K. (2018). Demarcating circulation regimes of synchronously rotating terrestrial planets within the habitable zone. *The Astrophysical Journal*, 852(2):67.

Harman, C., Felton, R., Hu, R., Domagal-Goldman, S. D., Segura, A., Tian, F., and Kasting, J. (2018). Abiotic O_2 levels on planets around F, G, K, and M stars: effects of lightning-produced catalysts in eliminating oxygen false positives. *The Astrophysical Journal*, 866(1):56.

Harman, C., Schwieterman, E., Schottelkotte, J. C., and Kasting, J. (2015a). Abiotic O_2 levels on planets around F, G, K, and M stars: possible false positives for life? *The Astrophysical Journal*, 812(2):137.

Harman, S., Schottelkotte, J., and Kasting, J. (2015b). Constraining oxygen false positives for terrestrial planets around F, G, and K stars. *Pathways Towards Habitable Planets*, page 46.

Hart, M. H. (1979). Habitable zones about main sequence stars. *Icarus*, 37(1):351–357.

Hoffman, P. F., Abbot, D. S., Ashkenazy, Y., Benn, D. I., Brocks, J. J., Cohen, P. A., Cox, G. M., Creveling, J. R., Donnadieu, Y., Erwin, D. H., et al. (2017). Snowball Earth climate dynamics and Cryogenian geology-geobiology. *Science Advances*, 3(11):e1600983.

Hoffman, P. F., Kaufman, A. J., Halverson, G. P., and Schrag, D. P. (1998). A Neoproterozoic snowball Earth. *Science*, 281(5381):1342–1346.

Hoffman, P. F. and Schrag, D. P. (2002). The snowball Earth hypothesis: testing the limits of global change. *Terra Nova*, 14(3):129–155.

Hu, Y. and Yang, J. (2014). Role of ocean heat transport in climates of tidally locked exoplanets around m dwarf stars. *Proceedings of the National Academy of Sciences*, 111(2):629–634.

Ingersoll, A. P. (1969). The runaway greenhouse: A history of water on venus. *Journal of Atmospheric Sciences*, 26(6):1191–1198.

Isson, T. T., Planavsky, N. J., Coogan, L., Stewart, E., Ague, J., Bolton, E., Zhang, S., McKenzie, N., and Kump, L. (2020). Evolution of the global carbon cycle and climate regulation on Earth. *Global Biogeochemical Cycles*, 34(2):e2018GB006061.

Jansen, T., Scharf, C., Way, M., and Del Genio, A. (2019). Climates of warm Earth-like planets. II. rotational "goldilocks" zones for fractional habitability and silicate weathering. *The Astrophysical Journal*, 875(2):79.

Jenouvrier, A., Mérienne, M.-F., Coquart, B., Carleer, M., Fally, S., Vandaele, A. C., Hermans, C., and Colin, R. (1999). Fourier transform spectroscopy of the O_2 herzberg bands: I. rotational analysis. *Journal of molecular spectroscopy*, 198(1):136–162.

Joshi, M., Haberle, R., and Reynolds, R. (1997). Simulations of the atmospheres of synchronously rotating terrestrial planets orbiting M dwarfs: Conditions for atmospheric collapse and the implications for habitability. *Icarus*, 129(2):450–465.

Joshi, M. M. and Haberle, R. M. (2012a). Suppression of the Water Ice and Snow Albedo Feedback on Planets Orbiting Red Dwarf Stars and the Subsequent Widening of the Habitable Zone. *Astrobiology*, 12(1):3–8.

Joshi, M. M. and Haberle, R. M. (2012b). Suppression of the water ice and snow albedo feedback on planets orbiting red dwarf stars and the subsequent widening of the habitable zone. *Astrobiology*, 12(1):3–8.

Kadoya, S. and Tajika, E. (2014). Conditions for oceans on Earth-like planets orbiting within the habitable zone: Importance of volcanic CO_2 degassing. *The Astrophysical Journal*, 790(2):107.

Kasting, J. and Donahue, T. (1980). The evolution of atmospheric ozone. *Journal of Geophysical Research: Oceans*, 85(C6):3255–3263.

Kasting, J. F. (1988). Runaway and moist greenhouse atmospheres and the evolution of Earth and Venus. *Icarus*, 74(3):472–494.

Kasting, J. F. (1991). CO_2 condensation and the climate of early mars. *icarus*, 94(1):1–13.

Kasting, J. F., Liu, S., and Donahue, T. (1979). Oxygen levels in the prebiological atmosphere. *Journal of Geophysical Research: Oceans*, 84(C6):3097–3107.

Kasting, J. F. and Pollack, J. B. (1983). Loss of water from venus. i. hydrodynamic escape of hydrogen. *Icarus*, 53(3):479–508.

Kasting, J. F., Whitmire, D. P., and Reynolds, R. T. (1993a). Habitable zones around main sequence stars. *Icarus*, 101(1):108–128.

Kasting, J. F., Whitmire, D. P., and Reynolds, R. T. (1993b). Habitable zones around main-sequence stars. *Icarus*, 101(1):108–128.

Kinnison, D., Brasseur, G. P., Walters, S., Garcia, R., Marsh, D., Sassi, F., Harvey, V., Randall, C., Emmons, L., Lamarque, J., et al. (2007). Sensitivity of chemical tracers to meteorological parameters in the mozart-3 chemical transport model. *Journal of Geophysical Research: Atmospheres*, 112(D20).

Kipping, D. (2020). An objective bayesian analysis of life's early start and our late arrival. *Proceedings of the National Academy of Sciences*, 117(22):11995–12003.

Kirschvink, J. (1992). Late Proterozoic low-latitude global glaciation: The snowball Earth. In Schopf, J. and Klein, C., editors, *The Proterozoic Biosphere: A Multidisciplinary Study*, pages 51–52. Cambridge University Press, New York.

Kite, E., Gaidos, E., and Manga, M. (2011). Climate instability on tidally locked exoplanets. *Astrophys Journal*, 743(1).

Kite, E. S. and Ford, E. B. (2018). Habitability of exoplanet waterworlds. *The Astrophysical Journal*, 864(1):75.

Kocis, L. and Whiten, W. J. (1997). Computational investigations of low-discrepancy sequences. *ACM Transactions on Mathematical Software (TOMS)*, 23(2):266–294.

Koll, D. D. B. and Abbot, D. S. (2015). Deciphering thermal phase curves of dry, tidally locked terrestrial planets. *The Astrophysical Journal*, 802:21.

Koll, D. D. B. and Abbot, D. S. (2016). Temperature structure and atmospheric circulation of dry, tidally locked rocky exoplanets. *The Astrophysical Journal*, 825:99.

Kollig, T. and Keller, A. (2002). Efficient multidimensional sampling. *Computer Graphics Forum*, 21(3):557–563.

Komacek, T. D., Fauchez, T. J., Wolf, E. T., and Abbot, D. S. (2020). Clouds will likely prevent the detection of water vapor in jwst transmission spectra of terrestrial exoplanets. *The Astrophysical Journal Letters*, 888(2):L20.

Kopparapu, R., Wolf, E. T., Haqq-Misra, J., Yang, J., Kasting, J. F., Meadows, V., Terrien, R., and Mahadevan, S. (2016a). The inner edge of the habitable zone for synchronously rotating planets around low-mass stars using general circulation models. *The Astrophysical Journal*, 819(1):84.

Kopparapu, R. K., Hébrard, E., Belikov, R., Batalha, N. M., Mulders, G. D., Stark, C., Teal, D., Domagal-Goldman, S., and Mandell, A. (2018). Exoplanet classification and yield estimates for direct imaging missions. *The Astrophysical Journal*, 856(2):122.

Kopparapu, R. K., Ramirez, R., Kasting, J. F., Eymet, V., Robinson, T. D., Mahadevan, S., Terrien, R. C., Domagal-Goldman, S., Meadows, V., and Deshpande, R. (2013). Habitable zones around main-sequence stars: new estimates. *The Astrophysical Journal*, 765(2):131.

Kopparapu, R. K., Ramirez, R. M., Schottelkotte, J., Kasting, J. F., Domagal-Goldman, S., and Eymet, V. (2014). Habitable zones around main-sequence stars: dependence on planetary mass. *The Astrophysical Journal Letters*, 787(2):L29.

Kopparapu, R. K., Wolf, E. T., Haqq-Misra, J., Yang, J., Kasting, J. F., Meadows, V., Terrien, R., and Mahadevan, S. (2016b). The inner edge of the habitable zone for synchronously rotating planets around low-mass stars using general circulation models. *The Astrophysical Journal*, 819(1):84.

Kreidberg, L. and Loeb, A. (2016). Prospects for characterizing the atmosphere of proxima centauri b. *The Astrophysical Journal Letters*, 832(1):L12.

Krissansen-Totton, J., Arney, G. N., and Catling, D. C. (2018a). Constraining the climate and ocean pH of the early Earth with a geological carbon cycle model. *Proceedings of the National Academy of Sciences*, 115(16):4105–4110.

Krissansen-Totton, J., Fortney, J. J., Nimmo, F., and Wogan, N. (2021). Oxygen false positives on habitable zone planets around sun-like stars. *AGU Advances*, 2(2):e2020AV000294.

Krissansen-Totton, J., Olson, S., and Catling, D. C. (2018b). Disequilibrium biosignatures over Earth history and implications for detecting exoplanet life. *Science advances*, 4(1):eaao5747.

Kump, L. R., Brantley, S. L., and Arthur, M. A. (2000). Chemical weathering, atmospheric CO_2, and climate. *Annual Review of Earth and Planetary Sciences*, 28(1):611–667.

Laakso, T. A. and Schrag, D. (2017a). A theory of atmospheric oxygen. *Geobiology*, 15(3):366–384.

Laakso, T. A. and Schrag, D. P. (2014). Regulation of atmospheric oxygen during the Proterozoic. *Earth and Planetary Science Letters*, 388:81–91.

Laakso, T. A. and Schrag, D. P. (2017b). A theory of atmospheric oxygen. *Geobiology*, 15:366–384.

Lacki, B. C. (2016). The log log prior for the frequency of extraterrestrial intelligences. *arXiv preprint arXiv:1609.05931*.

Langen, P. L. and Alexeev, V. A. (2004). Multiple equilibria and asymmetric climates in the ccm3 coupled to an oceanic mixed layer with thermodynamic sea ice. *Geophysical research letters*, 31(4).

Leconte, J., Forget, F., Charnay, B., Wordsworth, R., Selsis, F., Millour, E., and Spiga, A. (2013). 3d climate modeling of close-in land planets: Circulation patterns, climate moist bistability, and habitability. *Astronomy & Astrophysics*, 554:A69.

Leconte, J., Wu, H., Menou, K., and Murray, N. (2015). Asynchronous rotation of Earth-mass planets in the habitable zone of lower-mass stars. *Science*, 347(6222):632–635.

Lehmer, O. R., Catling, D. C., and Krissansen-Totton, J. (2020). Carbonate-silicate cycle predictions of Earth-like planetary climates and testing the habitable zone concept. *Nature communications*, 11(1):1–10.

Lincowski, A. P., Lustig-Yaeger, J., and Meadows, V. S. (2019). Observing isotopologue bands in terrestrial exoplanet atmospheres with the james webb space telescope: implications for identifying past atmospheric and ocean loss. *The Astronomical Journal*, 158(1):26.

Lovelock, J. E. (1965). A physical basis for life detection experiments. *Nature*, 207(4997):568–570.

Lucarini, V., Pascale, S., Boschi, R., Kirk, E., and Iro, N. (2013). Habitability and multistability in Earth-like planets. *Astronomische Nachrichten*, 334(6):576–588.

Luger, R. and Barnes, R. (2015). Extreme water loss and abiotic o_2 buildup on planets throughout the habitable zones of M dwarfs. *Astrobiology*, 15(2):119–143.

Lustig-Yaeger, J., Meadows, V. S., and Lincowski, A. P. (2019). The detectability and characterization of the trappist-1 exoplanet atmospheres with jwst. *The Astronomical Journal*, 158(1):27.

Lyons, T. W., Reinhard, C. T., and Planavsky, N. J. (2014). The rise of oxygen in Earth's early ocean and atmosphere. *Nature*, 506(7488):307–315.

Macdonald, F. A., Swanson-Hysell, N. L., Park, Y., Lisiecki, L., and Jagoutz, O. (2019). Arc-continent collisions in the tropics set Earth's climate state. *Science*, 364(6436):181–184.

Marsh, D. R., Mills, M. J., Kinnison, D. E., Lamarque, J.-F., Calvo, N., and Polvani, L. M. (2013). Climate change from 1850 to 2005 simulated in cesm1 (waccm). *Journal of climate*, 26(19):7372–7391.

Mayor, M. and Queloz, D. (1995). A Jupiter-mass companion to a solar-type star. *Nature*, 378(6555):355–359.

Meadows, V. S. (2008). Planetary environmental signatures for habitability and life. In *Exoplanets*, pages 259–284. Springer.

Meadows, V. S. (2017). Reflections on O_2 as a biosignature in exoplanetary atmospheres. *Astrobiology*, 17(10):1022–1052.

Meadows, V. S., Arney, G. N., Schwieterman, E. W., Lustig-Yaeger, J., Lincowski, A. P., Robinson, T., Domagal-Goldman, S. D., Deitrick, R., Barnes, R. K., Fleming, D. P., et al. (2018a). The habitability of proxima centauri b: environmental states and observational discriminants. *Astrobiology*, 18(2):133–189.

Meadows, V. S. and Crisp, D. (1996). Ground-based near-infrared observations of the venus nightside: The thermal structure and water abundance near the surface. *Journal of Geophysical Research: Planets*, 101(E2):4595–4622.

Meadows, V. S., Reinhard, C. T., Arney, G. N., Parenteau, M. N., Schwieterman, E. W., Domagal-Goldman, S. D., Lincowski, A. P., Stapelfeldt, K. R., Rauer, H., DasSarma, S., et al. (2018b). Exoplanet biosignatures: understanding oxygen as a biosignature in the context of its environment. *Astrobiology*, 18(6):630–662.

Menou, K. (2013). Water-trapped worlds. *The Astrophysical Journal*, 774(1):51.

Menou, K. (2015). Climate stability of habitable Earth-like planets. *Earth and Planetary Science Letters*, 429:20–25.

Mérienne, M.-F., Jenouvrier, A., Coquart, B., Carleer, M., Fally, S., Colin, R., Vandaele, A. C., and Hermans, C. (2000). Fourier transform spectroscopy of the O_2 herzberg bands: Ii. band oscillator strengths and transition moments. *Journal of Molecular Spectroscopy*, 202(2):171–193.

Mérienne, M.-F., Jenouvrier, A., Coquart, B., Carleer, M., Fally, S., Colin, R., Vandaele,

A. C., and Hermans, C. (2001). Improved data set for the herzberg band systems of 16 o 2. *JMoSp*, 207(1):120–120.

Merlis, T. M. and Schneider, T. (2010). Atmospheric dynamics of Earth-like tidally locked aquaplanets. *Journal of Advances in Modeling Earth Systems*, 2.

Mulders, G. D., Pascucci, I., Apai, D., and Ciesla, F. J. (2018). The exoplanet population observation simulator. i. the inner edges of planetary systems. *The Astronomical Journal*, 156(1):24.

Neale, R. B., Chen, C.-C., Gettelman, A., Lauritzen, P. H., Park, S., Williamson, D. L., Conley, A. J., Garcia, R., Kinnison, D., Lamarque, J.-F., et al. (2010). Description of the ncar community atmosphere model (cam 5.0). *NCAR Tech. Note NCAR/TN-486+ STR*, 1(1):1–12.

Neil, A. R. and Rogers, L. A. (2020). A joint mass–radius–period distribution of exoplanets. *The Astrophysical Journal*, 891(1):12.

North, G. (1975). Analytical solution to a simple climate model with diffusive heat transport. *J Atmos Sci*, 32(7):1301–1307.

Olson, S. L., Schwieterman, E. W., Reinhard, C. T., and Lyons, T. W. (2018a). Earth: Atmospheric evolution of a habitable planet. *Handbook of Exoplanets*, page 189.

Olson, S. L., Schwieterman, E. W., Reinhard, C. T., Ridgwell, A., Kane, S. R., Meadows, V. S., and Lyons, T. W. (2018b). Atmospheric seasonality as an exoplanet biosignature. *The Astrophysical Journal Letters*, 858(2):L14.

Owen, T. (1980). The search for early forms of life in other planetary systems: future possibilities afforded by spectroscopic techniques. In *Strategies for the Search for Life in the Universe*, pages 177–185. Springer.

Ozaki, K., Reinhard, C. T., and Tajika, E. (2019). A sluggish mid-Proterozoic biosphere and its effect on Earth's redox balance. *Geobiology*, 17(1):3–11.

Paradise, A. and Menou, K. (2017). Gcm simulations of unstable climates in the habitable zone. *The Astrophysical Journal*, 848(1):33.

Pascucci, I., Mulders, G. D., and Lopez, E. (2019). The impact of stripped cores on the frequency of Earth-size planets in the habitable zone. *The Astrophysical Journal Letters*, 883(1):L15.

Pavlov, A. and Kasting, J. (2002). Mass-independent fractionation of sulfur isotopes in archean sediments: strong evidence for an anoxic archean atmosphere. *Astrobiology*, 2(1):27–41.

Pedregosa, F., Varoquaux, G., Gramfort, A., Michel, V., Thirion, B., Grisel, O., Blondel, M., Prettenhofer, P., Weiss, R., Dubourg, V., et al. (2011). Scikit-learn: Machine learning in python. *the Journal of machine Learning research*, 12:2825–2830.

Penman, D. E., Rugenstein, J. K. C., Ibarra, D. E., and Winnick, M. J. (2020). Silicate weathering as a feedback and forcing in Earth's climate and carbon cycle. *Earth-Science Reviews*, page 103298.

Petigura, E. A., Howard, A. W., and Marcy, G. W. (2013). Prevalence of Earth-size planets orbiting Sun-like stars. *Proceedings of the National Academy of Sciences*, 110(48):19273–19278.

Pierrehumbert, R., Abbot, D., Voigt, A., and Koll, D. (2011). Climate of the Neoproterozoic. *Annual Review of Earth and Planetary Sciences*, 39:417–460.

Pierrehumbert, R. T. (2010a). A palette of climates for gliese 581g. *The Astrophysical Journal Letters*, 726(1):L8.

Pierrehumbert, R. T. (2010b). *Principles of planetary climate*. Cambridge University Press.

Pierrehumbert, R. T. (2011). A palette of climates for Gliese 581g. *Astrophys J Lett*, 726(1):L8.

Planavsky, N. J., Reinhard, C. T., Wang, X., Thomson, D., McGoldrick, P., Rainbird, R. H., Johnson, T., Fischer, W. W., and Lyons, T. W. (2014). Low Mid-Proterozoic atmospheric oxygen levels and the delayed rise of animals. *science*, 346(6209):635–638.

Planavsky, N. J., Rouxel, O. J., Bekker, A., Lalonde, S. V., Konhauser, K. O., Reinhard, C. T., and Lyons, T. W. (2010). The evolution of the marine phosphate reservoir. *Nature*, 467(7319):1088.

Reinhard, C. T., Olson, S. L., Schwieterman, E. W., and Lyons, T. W. (2017). False negatives for remote life detection on ocean-bearing planets: lessons from the early Earth. *Astrobiology*, 17(4):287–297.

Ribas, I., Bolmont, E., Selsis, F., Reiners, A., Leconte, J., Raymond, S. N., Engle, S. G., Guinan, E. F., Morin, J., Turbet, M., et al. (2016). The habitability of Proxima Centauri b-I. Irradiation, rotation and volatile inventory from formation to the present. *Astronomy & Astrophysics*, 596:A111.

Robinson, T. D., Meadows, V. S., and Crisp, D. (2010). Detecting oceans on extrasolar planets using the glint effect. *The Astrophysical Journal Letters*, 721(1):L67.

Robinson, T. D., Stapelfeldt, K. R., and Marley, M. S. (2016). Characterizing rocky and gaseous exoplanets with 2 m class space-based coronagraphs. *Publications of the Astronomical Society of the Pacific*, 128(960):025003.

Roe, G. H. and Baker, M. B. (2010). Notes on a Catastrophe: A Feedback Analysis of Snowball Earth. *J Climate*, 23(17):4694–4703.

Rogers, L. A. (2015). Most 1.6 Earth-radius planets are not rocky. *The Astrophysical Journal*, 801(1):41.

Rose, B. E. (2015). Stable waterbelt climates controlled by tropical ocean heat transport: A nonlinear coupled climate mechanism of relevance to snowball Earth. *Journal of Geophysical Research: Atmospheres*, 120(4):1404–1423.

Rose, B. E., Cronin, T. W., and Bitz, C. M. (2017). Ice caps and ice belts: The effects of obliquity on ice- albedo feedback. *The Astrophysical Journal*, 846(1):28.

Rose, B. E. and Marshall, J. (2009). Ocean heat transport, sea ice, and multiple climate states: Insights from energy balance models. *Journal of the Atmospheric Sciences*, 66(9):2828–2843.

Rushby, A. J., Claire, M. W., Osborn, H., and Watson, A. J. (2013). Habitable zone lifetimes of exoplanets around main sequence stars. *Astrobiology*, 13(9):833–849.

Rushby, A. J., Shields, A. L., and Joshi, M. (2019). The effect of land fraction and host star spectral energy distribution on the planetary albedo of terrestrial worlds. *The Astrophysical Journal*, 887(1):29.

Rushby, A. J., Shields, A. L., Wolf, E. T., Laguë, M., and Burgasser, A. (2020). The effect of land albedo on the climate of land-dominated planets in the trappist-1 system. *The Astrophysical Journal*, 904(2):124.

Sagan, C., Thompson, W. R., Carlson, R., Gurnett, D., and Hord, C. (1993). A search for life on Earth from the Galileo spacecraft. *Nature*, 365(6448):715–721.

Salameh, J., Popp, M., and Marotzke, J. (2017). The role of sea-ice albedo in the climate of slowly rotating aquaplanets. *Climate Dynamics*, pages 1–16.

Sandberg, A., Drexler, E., and Ord, T. (2018). Dissolving the fermi paradox. *arXiv preprint arXiv:1806.02404*.

Schidlowski, M. (1988). A 3,800-million-year isotopic record of life from carbon in sedimentary rocks. *Nature*, 333(6171):313–318.

Schwieterman, E. W., Kiang, N. Y., Parenteau, M. N., Harman, C. E., DasSarma, S., Fisher, T. M., Arney, G. N., Hartnett, H. E., Reinhard, C. T., Olson, S. L., et al. (2018). Exoplanet biosignatures: a review of remotely detectable signs of life. *Astrobiology*, 18(6):663–708.

Seager, S., Bains, W., and Petkowski, J. (2016). Toward a list of molecules as potential biosignature gases for the search for life on exoplanets and applications to terrestrial biochemistry. *Astrobiology*, 16(6):465–485.

Seager, S. and Deming, D. (2010). Exoplanet atmospheres. *Annual Review of Astronomy and Astrophysics*, 48:631–672.

Seager, S., Turner, E. L., Schafer, J., and Ford, E. B. (2005). Vegetation's red edge: a possible spectroscopic biosignature of extraterrestrial plants. *Astrobiology*, 5(3):372–390.

Segura, A., Kasting, J., Meadows, V., Cohen, M., Scalo, J., Crisp, D., Butler, R., and Tinetti, G. (2005). Biosignatures from Earth-like planets around M dwarfs. *Astrobiology*, 5(6):706–725.

Segura, A., Meadows, V., Kasting, J., Crisp, D., and Cohen, M. (2007). Abiotic formation of O_2 and O_3 in high-CO_2 terrestrial atmospheres. *Astronomy & Astrophysics*, 472(2):665–679.

Sellers, W. D. (1969). A global climate model based on the energy balance of the Earth-atmosphere system. *J of App Meteorology*, 8:392–400.

Shields, A. L., Bitz, C. M., Meadows, V. S., Joshi, M. M., and Robinson, T. D. (2014). Spectrum-driven planetary deglaciation due to increases in stellar luminosity. *The Astrophysical Journal Letters*, 785(1):L9.

Shields, A. L., Meadows, V. S., Bitz, C. M., Pierrehumbert, R. T., Joshi, M. M., and Robinson, T. D. (2013). The effect of host star spectral energy distribution and ice-albedo feedback on the climate of extrasolar planets. *Astrobiology*, 13(8):715–739.

Sousa-Silva, C., Petkowski, J. J., and Seager, S. (2019). Molecular simulations for the spectroscopic detection of atmospheric gases. *Physical Chemistry Chemical Physics*, 21(35):18970–18987.

Spiegel, D. S. and Turner, E. L. (2012). Bayesian analysis of the astrobiological implications of life's early emergence on Earth. *Proceedings of the National Academy of Sciences*, 109(2):395–400.

Stark, C. C., Belikov, R., Bolcar, M. R., Cady, E., Crill, B. P., Ertel, S., Groff, T., Hildebrandt, S., Krist, J., Lisman, P. D., et al. (2019). ExoEarth yield landscape for future direct imaging space telescopes. *Journal of Astronomical Telescopes, Instruments, and Systems*, 5(2):024009.

Stark, C. C., Roberge, A., Mandell, A., and Robinson, T. D. (2014). Maximizing the exoEarth candidate yield from a future direct imaging mission. *The Astrophysical Journal*, 795(2):122.

Stolper, D., Bender, M., Dreyfus, G., Yan, Y., and Higgins, J. (2016). A pleistocene ice core record of atmospheric O_2 concentrations. *Science*, 353(6306):1427–1430.

Strogatz, S. H. (1994). Nonlinear dynamics and chaos: with applications to physics. *Biology, Chemistry, and Engineering (Studies in Nonlinearity), Perseus, Cambridge, UK.*

The LUVOIR Team, . et al. (2019). The luvoir mission concept study final report. *arXiv preprint arXiv:1912.06219.*

Tian, F., France, K., Linsky, J. L., Mauas, P. J., and Vieytes, M. C. (2014). High stellar fuv/nuv ratio and oxygen contents in the atmospheres of potentially habitable planets. *Earth and Planetary Science Letters*, 385:22–27.

Tian, F., Toon, O. B., Pavlov, A. A., and De Sterck, H. (2005). Transonic hydrodynamic escape of hydrogen from extrasolar planetary atmospheres. *The Astrophysical Journal*, 621(2):1049.

Turbet, M. (2020). Two examples of how to use observations of terrestrial planets orbiting in temperate orbits around low mass stars to test key concepts of planetary habitability. *arXiv preprint arXiv:2005.06512*.

Turbet, M., Forget, F., Leconte, J., Charnay, B., and Tobie, G. (2017). Co_2 condensation is a serious limit to the deglaciation of Earth-like planets. *arXiv preprint arXiv:1703.04624*.

Turbet, M., Leconte, J., Selsis, F., Bolmont, E., Forget, F., Ribas, I., Raymond, S. N., and Anglada-Escudé, G. (2016). The habitability of Proxima Centauri b-II. Possible climates and observability. *Astronomy & Astrophysics*, 596:A112.

Vallis, G. K. and Farneti, R. (2009). Meridional energy transport in the coupled atmosphere–ocean system: Scaling and numerical experiments. *Quarterly Journal of the Royal Meteorological Society: A journal of the atmospheric sciences, applied meteorology and physical oceanography*, 135(644):1643–1660.

Villanueva, G. L., Smith, M. D., Protopapa, S., Faggi, S., and Mandell, A. M. (2018). Planetary spectrum generator: An accurate online radiative transfer suite for atmospheres, comets, small bodies and exoplanets. *Journal of Quantitative Spectroscopy and Radiative Transfer*, 217:86–104.

Voigt, A., Abbot, D. S., Pierrehumbert, R. T., and Marotzke, J. (2011). Initiation of a Marinoan Snowball Earth in a state-of-the-art atmosphere-ocean general circulation model. *Clim. Past*, 7:249–263.

Voigt, A. and Marotzke, J. (2010). The transition from the present-day climate to a modern Snowball Earth. *Climate Dynamics*, 35(5):887–905.

Walker, J. C., Hays, P., and Kasting, J. F. (1981a). A negative feedback mechanism for the long-term stabilization of Earth's surface temperature. *Journal of Geophysical Research: Oceans*, 86(C10):9776–9782.

Walker, J. C. G., Hays, P. B., and Kasting, J. F. (1981b). A negative feedback mechanism for the long term stabilization of Earth's surface temperature. *Journal of Geophysical Research*, 86(NC10):9776–9782.

Wang, J., Mawet, D., Hu, R., Ruane, G., Delorme, J.-R., and Klimovich, N. (2018). Baseline requirements for detecting biosignatures with the habex and luvoir mission concepts. *Journal of Astronomical Telescopes, Instruments, and Systems*, 4(3):035001.

Wang, Y., Tian, F., and Hu, Y. (2014). Climate patterns of habitable exoplanets in eccentric orbits around m dwarfs. *The Astrophysical Journal Letters*, 791(1):L12.

Way, M., Del Genio, A., Kelley, M., Aleinov, I., and Clune, T. (2015). Exploring the inner edge of the habitable zone with fully coupled oceans. *arXiv preprint arXiv:1511.07283*.

Way, M. J., Aleinov, I., Amundsen, D. S., Chandler, M., Clune, T., Del Genio, A. D., Fujii, Y., Kelley, M., Kiang, N. Y., Sohl, L., et al. (2017). Resolving orbital and climate keys of Earth and extraterrestrial environments with dynamics (ROCKE-3D) 1.0: a general circulation model for simulating the climates of rocky planets. *The Astrophysical Journal Supplement Series*, 231(1):12.

Way, M. J., Del Genio, A. D., Aleinov, I., Clune, T. L., Kelley, M., and Kiang, N. Y. (2018). Climates of warm Earth-like planets. I. 3D model simulations. *The Astrophysical Journal Supplement Series*, 239(2):24.

Williams, D. M. and Kasting, J. F. (1997). Habitable planets with high obliquities. *Icarus*, 129(1):254–267.

Winton, M. (2003). On the climatic impact of ocean circulation. *Journal of climate*, 16(17):2875–2889.

Wolf, E. T. (2017). Assessing the habitability of the TRAPPIST-1 system using a 3D climate model. *The Astrophysical Journal Letters*, 839(1):L1.

Wolf, E. T., Shields, A. L., Kopparapu, R. K., Haqq-Misra, J., and Toon, O. B. (2017). Constraints on climate and habitability for Earth-like exoplanets determined from a general circulation model. *The Astrophysical Journal*, 837(2):107.

Wordsworth, R. and Pierrehumbert, R. (2014). Abiotic oxygen-dominated atmospheres on terrestrial habitable zone planets. *The Astrophysical Journal Letters*, 785(2):L20.

Wordsworth, R. D., Forget, F., Selsis, F., Millour, E., Charnay, B., and Madeleine, J.-B. (2011). Gliese 581D is the first discovered terrestrial-mass exoplanet in the habitable zone. *Astrophys J Lett*, 733(2):L48.

Wunsch, C. and Ferrari, R. (2004). Vertical mixing, energy, and the general circulation of the oceans. *Annu. Rev. Fluid Mech.*, 36:281–314.

Yang, J., Abbot, D. S., Koll, D. D., Hu, Y., and Showman, A. P. (2019a). Ocean dynamics and the inner edge of the habitable zone for tidally locked terrestrial planets. *The Astrophysical Journal*, 871(1):29.

Yang, J., Cowan, N. B., and Abbot, D. S. (2013). Stabilizing cloud feedback dramatically expands the habitable zone of tidally locked planets. *Astrophysical Journal Letters*, 771.

Yang, J., Leconte, J., Wolf, E. T., Merlis, T., Koll, D. D., Forget, F., and Abbot, D. S. (2019b). Simulations of water vapor and clouds on rapidly rotating and tidally locked planets: A 3d model intercomparison. *The Astrophysical Journal*, 875(1):46.

Yang, J., Liu, Y., Hu, Y., and Abbot, D. S. (2014). Water trapping on tidally locked terrestrial planets requires special conditions. *Astrophysical Journal Letters*, 796.

Yang, J., Peltier, W., and Hu, Y. (2012a). The initiation of modern "soft Snowball" and "hard Snowball" climates in CCSM3. Part I: the influence of solar luminosity, CO_2 concentration and the sea-ice/snow albedo parameterization. *Journal of Climate*, 25:2711–2736.

Yang, J., Peltier, W., and Hu, Y. (2012b). The initiation of modern "soft Snowball" and "hard Snowball" climates in CCSM3. Part II: climate dynamic feedbacks. *Journal of Climate*, 25:2737–2754.

Zeebe, R. E. and Caldeira, K. (2008). Close mass balance of long-term carbon fluxes from ice-core co 2 and ocean chemistry records. *Nature Geoscience*, 1(5):312–315.

Zhan, Z., Seager, S., Petkowski, J. J., Sousa-Silva, C., Ranjan, S., Huang, J., and Bains, W. (2021). Assessment of isoprene as a possible biosignature gas in exoplanets with anoxic atmospheres. *Astrobiology*.

Zou, H. and Hastie, T. (2005). Regularization and variable selection via the elastic net. *Journal of the royal statistical society: series B (statistical methodology)*, 67(2):301–320.